

**ELECTRONIC STRUCTURE STUDIES OF SOME
LAYERED SUPERCONDUCTORS AND
SEMICONDUCTORS USING PHOTOEMISSION
SPECTROSCOPY**

By

Pramita Mishra

PHYS07200804007

Institute of Physics, Bhubaneswar

*A thesis submitted to the
Board of Studies in Physical Sciences*

*In partial fulfillment of requirements
For the Degree of*

**DOCTOR OF PHILOSOPHY
of**

HOMI BHABHA NATIONAL INSTITUTE



December 9, 2015

STATEMENT BY AUTHOR

This dissertation has been submitted in partial fulfillment of requirements for an advanced degree at Homi Bhabha National Institute (HBNI) and is deposited in the Library to be made available to borrowers under rules of the HBNI.

Brief quotations from this dissertation are allowable without special permission, provided that accurate acknowledgment of source is made. Requests for permission for extended quotation from or reproduction of this manuscript in whole or in part may be granted by the Competent Authority of HBNI when in his or her judgment the proposed use of the material is in the interests of scholarship. In all other instances, however, permission must be obtained from the author.

Pramita Mishra

CERTIFICATE

This is to certify that the thesis entitled "**Electronic structure studies of some layered superconductors and semiconductors using Photoemission Spectroscopy**", which is being submitted by **Ms. Pramita Mishra** in partial fulfillment of the degree of **Doctor of Philosophy in Physics** of **Homi Bhabha National Institute** is a record of her own research work carried by her. She has carried out her investigations for the last six years on the subject matter of the thesis under my supervision at **Institute of Physics, Bhubaneswar**. To the best of our knowledge, the matter embodied in this thesis has not been submitted for the award of any other degree.

Signature of the Candidate

Signature of the Supervisor

Pramita Mishra
Institute of Physics
Bhubaneswar

Prof. B. R. Sekhar
Professor
Institute of Physics
Bhubaneswar

DECLARATION

I, hereby declare that the investigation presented in the thesis has been carried out by me. The work is original and has not been submitted earlier as a whole or in part for a degree/diploma at this or any other Institution/University.

Pramita Mishra

To My Parents

Contents

Table of Contents	vii
Acknowledgement	viii
Synopsis	xi
List of Figures	xix
1 Introduction	1
1.1 Layered Materials :	1
1.2 Layered Superconductors:	2
1.2.1 Fe chalcogenides, $\text{FeSe}_{1-x}\text{Te}_x$	4
1.2.2 Nd based pnictides, $\text{NdFeAsO}_{1-x}\text{F}_x$	6
1.2.3 Electronic properties of Fe-superconductors	7
1.2.4 BiS_2 based superconductors	9
1.2.5 Electronic properties of BiS superconductors	10
1.3 Layered Semiconductors	10
1.3.1 Germanium Selenide (GeSe) :	11
2 Experimental Methodologies	21
2.1 Photoemission Spectroscopy:	21
2.1.1 Principle and Theory of photoemission	22
2.1.2 Instrumentation	29
2.2 Inverse Photoemission Spectroscopy	36
2.2.1 Principle and Theory of Inverse Photoemission	36
2.2.2 Instrumentation	38
2.3 Experimental Procedures	39
2.4 Band Structure Theory	41
2.4.1 The Many-Particle Problem	41

2.4.2	Density Functional Theory	42
2.4.3	Linear Muffin-tin Orbital method	43
3	Electronic structure study of Fe(Se,Te) superconductor	49
3.1	Introduction	49
3.2	Experimental	51
3.3	Results and Discussion	52
3.4	Conclusion	63
4	Electronic structure study of Nd[O_{1-x}F_x]FeAs superconductor	69
4.1	Introduction	69
4.2	Experimental	71
4.3	Results and Discussions	72
4.4	Conclusion	77
5	Electronic structure of rare-earth doped SrFBiS₂ superconductors	84
5.1	Introduction	84
5.2	Experimental	86
5.3	Results and Discussions	86
5.4	Conclusion	92
6	Electronic structure study of GeSe semiconductor	98
6.1	Introduction	98
6.2	Experimental	99
6.3	Results and Discussions	100
6.4	Conclusion	108
7	Summary	112
	Bibliography	115

Acknowledgement

The printed pages of this thesis is not a mere culmination of my research work rather a sum of experiences and interactions with many generous and inspiring people who have influenced me and led to the fruition of this thesis. The list is long but I cherish each contribution to my development as a scholar and an individual.

To start with, I would like to express my profound gratitude and deep regards to my Ph.D supervisor, Prof. B. R. Sekhar for his exemplary guidance, monitoring and constant encouragement through the course of my research work. Working with him gave me immense freedom in development of my research motivations and ideas. His exceptional expertise in dealing with instruments and unparalleled discussions was a constant source of motivation and inspiration. Many times, various non academic discussions dealing with different aspects of life, society and culture, in combination with a sip of tea were educative and interesting. I am extremely grateful to Mrs. Ranjana Sekhar and Kartyayini for making my stay homely during the course of my work. The fun filled evening gatherings along with the authentic Kerela cuisine, at their home, shall always be cherished.

I acknowledge the help, suggestions and discussions from Dr. S. R. Barman and Prof. Krishnakumar S. R. Menon during the course of inverse photoemission and ARPES experiments and Dr. V. P. S. Awana and Dr. G. K. Solanki for providing me samples. I am thankful to Prof. Pratap Kumar Sahoo for various discussions and help in my experimental work. I would like to thank all the experimental faculties of IOP for allowing me to avail the experimental facilities. I take this opportunity to thank my review committee members for their encouraging words and attention. A sincere thanks to Prof. Sudipta Mukherjee and Dr. Amitabh Virmani for the enjoyable moments spent during the gatherings and festivities at his home. It is my pleasure to thank Prof. Ajit Mohan Srivastava and Prof. Shikha Varma for various inspiring discussions and joyful moments during tea time. It was always a pleasure in attending the movie sessions and parties, at their home and I thank them for accepting me as an honorary member of their group and inviting me in all the gatherings.

I cannot thank enough Rupalidi for her constant support, guidance and cooperation in my

early days of research work. It gave me immense pleasure working and discussing with her both in academic and social aspects. Her enthusiastic approach in learning everything was a constant source of motivation for me. It was her presence and caring attitude which made my stay homely at IOP. A sincere gratitude to Himanshu for supporting me in the course and completion of my thesis work. His assistance and discussions, during the late night experiments, despite his dislike for late night work outs, is thanks worthy.

A special thanks to my invaluable network of supporting, forgiving and loving friends Vanaraj, Tanmoy and Raghav who made my period during the stay at IOP enjoyable as well as provided encouragement and motivation. The evening and late night hangouts at the IOP auditorium, tea time discussions and parties with all these buddies added flavour to my Ph.D life. The birthday celebrations in front of IOP auditorium shall always be cherished by me. Words are not enough to express my gratitude towards Vanaraj, for his support, encouragement, suggestion and most importantly for being a listening ear and bearing my idiosyncrasy during the sticky patch of my Ph.D days. The mouth watering dishes (specially kadhi and dal dhokri), tea-breaks and lighter moments at times of frustration made the path a bit easy. I owe to him for introducing me to a Gujurati delicacy “kadhi“. The remembrance of his recipe of cooking particular things in an extra particular way, illogical logics during discussions and late nights walk in the campus shall always bring a smile on my face. Thanks for being an awesome friend and it is this friendship which I shall treasure forever.

The early days of IOP were fun and lively with the story telling sessions of Trilochanda, the cooking sessions and sleepless night out masti with Binatadi, Rupalidi and Indrani. The company of Jayadi, Saumiadi, Anupamadi and Sudipta also made my stay pleasing. Although for shorter intervals, the company of Abhishek bhaiya, including his cooking, singing and movie sessions, was always enjoyable. A cup of tea at the canteen and hot discussions on various topics during walks around the campus with Shalik and Shreyansh, during the thesis writing phase, could not have been more pleasing. I thank all of them from the bottom of my heart. A special thanks to Ashutosh bhaiya for his constant help and encouragement along with the various discussions on academic as well as social fronts. I thank all the scholars who were involved in the khichdi parties and IOP express making these events an ever memorable one. Thanks to Ambika and Neeta for making my stay homely at IOP. Thanks to Mr Santosh Choudhury and

his family for their warm hospitality and the mouth watering Odia delicacies. Thanks to Abhishek Rai, Jayita and Maniraj for their constant help and discussions in IPES experiments and making my stay enjoyable at IUC-Indore. I would like to thank Ashish for his help and discussions in ARPES measurements. Thanks to Aurobindo, Biswajit, Geetanjali, Jasmin, Soumee and Abhishek - you were the guys outside my academic circle, whom I could rely on for any help and suggestions during the most crucial times. Thanks to Anshuman, Suman, Pushpsen and Souvanik for their help and motivation at different point of times. All my little companions Ananya, Agrata, Vikram and Ayansh deserve special thanks for making my stay stress relieving at IOP.

My sincere acknowledgements to Mr. Santosh Choudhury and Mr. Anup Kumar Behera for their timely technical support during the course of the experiments. I acknowledge the help of all the scientific and technical staffs of IOP for their help and cooperation. Acknowledgements to the excellent library and computer facilities provided by IOP and the timely help of all the academic as well as non academic staff. I express my deep gratitude to those who have offered pieces of advice, support and companionship, directly or indirectly, even if they remain unnamed. Its the time to thank all my teachers, but for their guidance I could never have been the person that I am today. I also express my gratitude towards all my critic, for their criticism boosted my self confidence and provided me strength to complete the thesis.

I would be amiss if I did not mention my elder brother and little sister whose support, love and affection was a driving force in the course and wrap up of the Phd thesis. Last but most importantly, words fall short to thank my parents, who have always been there for me, to share my joy on sunny days and to encourage me on rainy days. I cannot thank them enough for always believing in me when I did not have the strength to do so myself. This thesis is dedicated to them.

Pramita Mishra

Synopsis

Layered materials have become a topic of extensive research in the last few years owing to the rich fundamental physics and amazing technological applications [1]. The basic structure of these materials consist of stacks of 2 dimensional (2D) sheets with strong in-plane covalent bonding and interlayer van der Waals bonding. The 2D structure, give rise to many anomalous electronic and magnetic properties. These materials possess a vast spectrum of properties ranging from insulating through semiconducting to superconducting. In this thesis, we have investigated the electronic structure of the some layered superconductors and semiconductors using photoemission spectroscopy.

Photoemission spectroscopy is a very powerful experimental tool for probing the electronic structure, bonding and chemical nature of a material [2, 3]. Ultra violet photoemission (UPS) probes the occupied valence band density of states while X-Ray photoelectron spectroscopy (XPS) gives information regarding the core level electronic structure. Angle resolved photoelectron spectroscopy (ARPES) is of particular interest because it is the most direct technique to elucidate the momentum resolved occupied electronic structure of a material [4]. Moreover, availability of high resolution electron energy analyzers enables one to probe directly the most crucial low-energy excitations near the Fermi level (E_F). It can give valuable information regarding the finer spectral weight shifts, pseudogap behaviour [5], quasi particle excitations [6] and Orbital Selective Mottness [7, 8] near the Fermi level. On the other hand, inverse photoemission spectroscopy (IPES) probes the unoccupied density of states above the Fermi level [9]. For this thesis we have used Ultraviolet Photoemission Spectroscopy (UPS) and Inverse Photoemission Spectroscopy (IPES) to study the electronic structure of polycrystalline superconductors; Fe(Se,Te), NdFeASO(F) and $\text{Sr}_{0.5}\text{RE}_{0.5}\text{FBiS}_2$ (RE = Rare Earth). Angle Resolved Photoelectron Spectroscopy (ARPES) and X-Ray Photoelectron Spectroscopy (XPS) have been used to probe the valence band and core levels respectively, of GeSe. The experimental results are analyzed by our own LDA+U band structure calculations using TB-LMTO-ASA [10].

Amongst the various high T_c superconductors, the Fe-based systems are the first magnetic materials that are found to exhibit a T_c above 50 K [11]. There exist a strong interplay of electronic, spin and lattice degrees of freedom in these materials due to the multi orbital correlations existing in them. The presence of multiple bands crossing the Fermi level makes the electronic structure very sensitive to their crystal structure, especially the anion height (the distance of the

anion from the Fe plane) and the anion-Fe-anion bond angle [12]. Chapter IV and V of this thesis deals with our experimental studies of the electronic structure of the Fe superconductors using Photoemission spectroscopy and understanding them using the LDA based theoretical calculations. The doping and temperature dependent pseudogap seen in these systems have been explained in terms of the orbital selectivity of the Fe-3d orbitals. The moderate electron correlations coupled with Hund's coupling leads to Orbital Selective Mott transition [13] in Fe superconductors generating a mixed phase of localised electrons in some orbitals and itinerant in others.

The electronic structure of valence band and conduction band for $\text{FeSe}_{1-x}\text{Te}_x$ ($x = 1, 0.5, 0$) have been probed using UV Photoemission and Inverse Photoemission respectively. The experimental results and the theoretical LDA+U band structure calculations show a doping dependent pseudogap with Se substitution both in the occupied and unoccupied electronic states. The temperature dependent spectral weight transfer near the Fermi level, which results in the pseudogap, in the valence band region has been correlated to the changes in $\text{Fe}(\text{Se},\text{Te})_4$ tetrahedra which is sensitive to the change in chalcogen height i.e. the distance of chalcogen atom from the Fe plane. The calculations have shown that these structural changes lead to shifts in the electron occupancy from the xz/yz and $x^2 - y^2$ orbitals to the $3z^2 - r^2$ orbitals indicating a temperature induced crossover from a metallic state to an Orbital Selective Mott (OSM) Phase. Our study presents an observation of a temperature induced crossover to a low temperature OSM phase in the family of Fe chalcogenides. Complementary changes were observed on the unoccupied side in our inverse photoemission study. The depletion in spectral weight from the near E_F states at low temperature in IPES has been correlated with the enhancement of the $3z^2 - r^2$ orbitals in the PES. Changes in Fe-3d - chalcogen-p hybridisation originating from the changes in the chalcogen height due to doping and reduction in temperature controls the electronic structure of Fe superconductors. The coulomb correlation energy U , estimated from the combined PES and IPES spectra, signifies the enhancement in electron correlations in $\text{FeSe}_{1-x}\text{Te}_x$, with doping. The formation of pseudogap in PES and IPES confirms the importance of correlations in the 11 family of Fe superconductors.

In order to understand the generic behavior of the spectral weight shifts and the consequent normal state pseudogaps in the Fe based superconductors we made an extensive study of the valence band electronic structure of the $\text{Nd}[\text{O}_{1-x}\text{F}_x]\text{FeAs}$, which revealed the presence of a doping and temperature dependent pseudogap in this system also. Similar to the $\text{FeSe}(\text{Te})$

the pseudogap was found to be intimately correlated to the reduction in the pnictogen height induced by the changes in the Fe-As tetrahedra. The enhancement of Fe-3d (x^2-y^2 and yz/zx) - As- 4p hybridization at lower pnictogen height, results in a reduction of the occupancy of the x^2-y^2 and yz/zx orbitals at the Fermi level. This generates an Orbital Selective Mott insulating Phase (OSMP) at low temperature in the Fe (1111) systems, whereby the Fe-3d orbitals are rendered insulating. We found a similarity in the nature of the pseudogap observed in the (1111) and (11) family of superconductors signifying the role of multi orbital correlations in Fe superconductors.

Further, we have also made a comprehensive study of another family of superconductors, the Rare Earth (La, Ce) doped SrFBiS₂, using the valence band photoemission in conjunction with the LDA based band structure calculations, discussed in chapter VI of this thesis. The BiS₂ compounds exhibit a layered structure composed of stacks of spacer layers and BiS₂ layers [14] which play a significant role in determining the superconducting properties, similar to the case of the CuO layers in cuprates and Fe-P/Ch (P-pnictogen, Ch-chalcogen) layers in Fe superconductors. The changes in the near E_F electronic structure of SrFBiS₂ compound with rare earth (RE) doping has been focused in our study. The doped systems show a shifting of the Fermi level towards the conduction band which results in the shifting of photoemission spectral features towards higher binding energies compared to those of the parent compound. The combined effect of the doping of electrons and lowering of the Bi-S-Bi bond angle distortion, is more metallicity in the doped systems. Photoemission results revealed an enhanced spectral weight near E_F with a simultaneous depletion of states at higher binding energies. The pseudogap formation in BiS₂ superconductors shows a resemblance to the case of cuprates. The spectral weight depletion at low temperatures for both the undoped and doped compounds corroborates with the semiconducting nature of the BiS₂ in its normal state.

Recently, 2D chalcogenides with narrow band gaps have attracted much attention due to their richness in fundamental physics as well as diverse applications in thermoelectrics, optical filters, optical recording materials, infrared detectors, photovoltaics energy storage, photocatalysis, sensors etc. There has been an upsurge of research on the IV-VI semiconductors, particularly, the Germanium Selenide systems due to its use in random access memory applications and radiation sensors, solar cells and photovoltaics. Germanium Selenide belongs to the family of IV-VI layered chalcogenide semiconductors with orthorhombic structure (Pnma) [15]. The atomic layers are separated by van der Waals forces, making the material cleavable along the

b-c [100] planes. Chapter VII deals with the valence band electronic structure of Germanium Selenide (GeSe) single crystal investigated using Angle Resolved Photoemission spectroscopy (ARPES) and X-ray photoelectron spectroscopy. XPS study confirms the chemical constituent of the GeSe crystal. LDA based band structure calculations have been employed to support our experimental investigations. The experimentally observed bands from ARPES, match qualitatively with the calculated band structure along the high symmetry Γ -Z, Γ -Y and Γ -T directions. We have observed the valence band maximum at binding energy of -0.5 eV, which occurs nearly midway along Γ -Z direction, in accordance with the indirect band gap of GeSe. The difference in hybridisation of Se and Ge 4p orbitals along different directions is reflected as the variation of dispersion along these directions in the ARPES spectra. The predominance of Se 4p_z orbitals, evidenced from FAT band calculations, could be the cause of the highly dispersive bands along Γ -T direction. The detailed electronic structure analysis reveal the significance of the hybridized cation-anion 4p orbitals in the band dispersions in IV-VI semiconductors. This we find as the first comprehensive study on the electronic structure of a GeSe single crystal using ARPES in conjugation with theoretical band structure analysis.

Bibliography

- [1] D Johnson, S Clarke, J Wiley, K Koumoto, *Semicond. Sci. Technol.* **29**, 060301 (2014).
- [2] S. Hüfner, *Photoelectron Spectroscopy, Principles and Applications*, Springer
- [3] F. Reinert, S. Hüfner, *New J. Phys.* **7**, 97 (2005).
- [4] A. Damascelli, *Physica Scripta.* **T109**, 61 (2004).
- [5] T. Timusk, B. Statt, *Rep. Prog. Phys.* **62**, 61 (1999).
- [6] H. Ding, J. R. Engelbrecht, Z. Wang, J. C. Campuzano, S.-C. Wang, H.-B. Yang, R. Rogan, T. Takahashi, K. Kadowaki, D. G. Hinks, *Phys. Rev. Lett.* **87**, 227001 (2001).
- [7] M. Neupane, P. Richard, Z.-H. Pan, Y.-M. Xu, R. Jin, D. Mandrus, X. Dai, Z. Fang, Z. Wang, H. Ding, *Phys. Rev. Lett.* **103**, 097001 (2009).
- [8] M. Yi, D.H. Lu, R. Yu, S.C. Riggs, J.-H. Chu, B. Lv, Z.K. Liu, M. Lu, Y.-T. Cui, M. Hashimoto, S.-K. Mo, Z. Hussain, C.W. Chu, I.R. Fisher, Q. Si, Z.-X. Shen, *Phys. Rev. Lett.* **110**, 067003 (2013).
- [9] N.V. Smith, *Rep. Prog. Phys.* **51**, 1227 (1988).
- [10] O.K. Andersen, *Phys. Rev. B* **12**, 3060 (1975).
- [11] P.M. Aswathy, J.B. Anooja, P.M. Sarun, U. Syamaprasad, *Supercond. Sci. Technol.* **23**, 073001 (2010).
- [12] K. Kuroki, H. Usui, S. Onari, R. Arita, H. Aoki, *Phys. Rev. B* **79**, 224511 (2009).
- [13] M. Vojta, arXiv:1006.1559 (2010).
- [14] D. Yazici, I. Jeon, B.D. White, M.B. Maple, *Physica C* **514**, 218 (2015).

[15] L. Makinistian, E.A. Albanesi, *J. Phys.: Condens. Matter* **19**, 186211 (2007).

List of publications

1. Published

- (a) * Photoemission studies of the near E_F spectral weight shifts in $\text{FeSe}_{1-x}\text{Te}_x$ superconductor, **P. Mishra**, H. Lohani, R.A. Zargar, V.P.S. Awana, B.R. Sekhar, *J. Phys.: Condens. Matter* **26**, 425501 (2014)
- (b) * Electronic structure of germanium selenide investigated using ultra-violet photoelectron spectroscopy, **P. Mishra**, H. Lohani, A.K. Kundu, R. Patel, G.K. Solanki, Krishnakumar S.R. Menon and B.R. Sekhar, *Semicond. Sci. Technol.* **30**, 075001 (2015)
- (c) * Electronic structure of the unoccupied electron energy states in $\text{FeSe}_{1-x}\text{Te}_x$, **P. Mishra**, H. Lohani, M. Maniraj, J. Nayak, R.A. Zargar, V.P.S. Awana, B.R. Sekhar, *Solid State Communications* **219**, 48 (2015)
- (d) Investigation of correlation effects in FeSe and FeTe by LDA+U method, H. Lohani, **P. Mishra**, B.R. Sekhar, *Physica C* **512**, 54 (2015)
- (e) Structural and Optical study of Cobalt ion implanted Silicon, **Pramita Mishra**, Vanaraj Solanki, Ashutosh Rath, Soumee Chakraborty, Himanshu Lohani, Pratap K. Sahoo, Biju Raja Sekhar, *Advanced Materials Letters* **5**, 699 (2014)
- (f) Electronic structure of single crystal and highly oriented pyrolytic graphite from ARPES and KRIPES, R. Kundu, **P. Mishra**, B.R. Sekhar, M. Maniraj, S.R. Barman, *Physica B* **407**, 827 (2012)
- (g) Electronic structure of $\text{Bi}_{1-x}\text{Pb}_x\text{FeO}_3$ from photoelectron spectroscopic studies, R. Kundu, **P. Mishra**, B.R. Sekhar, J. Chaigneau, R. Haumont, R. Suryanarayanan, J.M. Kiat, *Solid State Communications* **151**, 256 (2011)
- (h) Defect controlled ferromagnetism in xenon ion irradiated zinc oxide, P. Satyarthi, S. Ghosh, **P. Mishra**, B.R. Sekhar, F. Singh, P. Kumar, D. Kanjilal, R.S. Dhaka, P. Srivastava, *Journal of Magnetism and Magnetic Materials* **385**, 318 (2015)
- (i) Correlation between structural, electrical and magnetic properties of GdMnO_3 bulk ceramics, S. Samantaray, D.K. Mishra, S.K. Pradhan, **P. Mishra**, B.R. Sekhar, Deb-dhyan Behera, P.P. Rout, S.K. Das, D.R. Sahu, B. K. Roul, *Journal of Magnetism and Magnetic Materials* **339**, 168 (2013)

- (j) Excitation dependent photoluminescence study of Si-rich a-SiNx:H thin films, Ravi Kumar Bommali, Sarab Preet Singh, Sanjay Rai, **P. Mishra**, B. R. Sekhar, G. Vijaya Prakash and P. Srivastava, Journal of Applied Physics **112**, 123518 (2012)

2. In Press

- (a) Room temperature superparamagnetism in rutile TiO₂ quantum dots: Produced via ECR sputtering, Vanaraj Solanki, I. Mishra, S.R. Joshi, **P. Mishra**, P. Dash. N.C. Mishra, D. Kanjilal, Shikha Varma, Nuclear Instruments and Methods in Physics Research B

3. To be submitted

- (a) * Electronic Structure of Nd[O_{1-x}F_x]FeAs investigated using Photoemission Spectroscopy, **P. Mishra**, H. Lohani, V.P.S. Awana, B.R. Sekhar
- (b) * Electronic structure study of RE doped SrFBiS₂ superconductors using Photoemission Spectroscopy, **P. Mishra**, H. Lohani, V.P.S. Awana, B.R. Sekhar

4. Conference Proceedings

- (a) Near E_F Electronic Structure of Graphite from Photoemission and Inverse Photoemission Studies, B.R. Sekhar, R. Kundu, **P. Mishra**, M. Maniraj, S.R. Barman, AIP Conference Proceedings, 1391, 50, 2011
- (b) * Pseudogap behaviour in FeTe and FeSe probed by photemission, **P. Mishra**, H. Lohani, R.A. Zargar, V.P.S. Awana, B.R. Sekhar, AIP Conference Proceedings, 1665, 130015 (2015)

* indicates papers on which this thesis is based

List of Figures

1.1	Prototypical crystal structure of iron based superconductors [16]. Red spheres correspond to Fe atoms while the pnictogens/chalcogens are shown as blue spheres. The filler layer is represented as grey slab.	4
1.2	Crystal Structure of Fe(Se,Te). The blue and red spheres correspond to Fe and Se/Te atoms respectively. α represents the Se/Te-Fe-Se/Te bond angle and Z_c is the chalcogen height defined as the height of Se/Te atoms from the Fe plane.	5
1.3	Crystal Structure of NdFeAsO(F). The cyan, red, black and blue spheres correspond to Nd, Fe As and O/F atoms respectively. Nd-O/F atoms form the spacer layer in between the two Fe-As layer. The parameters α and Z_c are also defined in the same manner as in Fe chalcogenides.	7
1.4	Crystal Structure of (a) ReOBiS ₂ , (b) SrFBiS ₂ and (c) Bi ₄ O ₄ (SO ₄)Bi ₂ S ₄ structures.	9
1.5	Crystal structure of GeSe with two unit cells. Red and blue spheres correspond to germanium and selenium atoms respectively. Ge1, Ge2, Ge3 and Ge4 correspond to first, second, third and fourth nearest neighbours respectively. The dashed line shows the cleavage plane along xy plane.	11
2.1	The schematic of a photoemission experiment. The photoemitted electron is specified by its kinetic energy (E_{kin}) and the emission angles θ and ϕ . The intensity of the outgoing electrons is measured by the analyzer as a function of (E_{kin}).	23
2.2	The schematic energy level diagram of photoemission process. E_F and E_{vac} are the Fermi energy and the vacuum level of the system. The intensity of the outcoming electrons is measured as a function of kinetic energy (E_{kin}).	24

2.3	Illustration of the three-step model of photoemission. It consists of (1) the photoexcitation of an electron in the bulk, (2) its travel through the solid to the surface and (3) its transmission through the surface into the vacuum.	27
2.4	Photoemission system used in lab.	29
2.5	A schematic diagram of hemispherical analyser [19].	32
2.6	A typical set-up of LEED.	35
2.7	The schematic of Inverse Photoemission Process.	36
2.8	The universal curve of the electron mean free path versus kinetic energy.	39
2.9	A schematic diagram of construction of Muffin-tin potential.	44
3.1	Structure of $\text{Fe}(\text{Se},\text{Te})_4$ tetrahedra showing the chalcogen height Z and angle α . Red and blue spheres correspond to Fe and Se/Te atoms respectively.	52
3.2	(a) High resolution (a) PES (b) IPES spectra taken at 300K for He I Valence band spectra measured at 300 K for $\text{FeSe}_{1-x}\text{Te}_x$ ($x = 1, 0.5, 0$). The features are marked as A, B, C and D. (b) IPES spectra for $\text{FeSe}_{1-x}\text{Te}_x$ ($x = 1, 0.5, 0$ shown in black, red and blue respectively) with marked features A and B. Dashed vertical lines correspond to the Fermi level.	53
3.3	Theoretically calculated (a) Total occupied DOS and (b) total unoccupied DOS, for $\text{FeSe}_{1-x}\text{Te}_x$ ($x = 1, 0.5, 0$). The theoretical features which matches with experiment has been marked as A, B, C and D in (a) and A1 and B1 in (b). The sub features of A (A' and A'') and A1 ($A1'$ and $A1''$) are also marked.	54
3.4	High Resolution (a) PES and (b) IPES spectra taken at 300 K for $\text{FeSe}_{1-x}\text{Te}_x$ ($x = 1, 0.5, 0$ shown in black, red and blue respectively). Features A' and A'' are denoted by black bars in (a). Inset of (a) shows the expanded view near the E_F	55
3.5	Fe 3d Partial DOS, using LDA+U, (a) Total occupied DOS and (b) total unoccupied DOS, for $\text{FeSe}_{1-x}\text{Te}_x$ ($x = 1, 0.5, 0$), with marked features. The PDOS contribution for xz (magenta) and yz (blue) orbitals are same for FeTe and FeSe. For $\text{FeSe}_{0.5}\text{Te}_{0.5}$, the xz and yz PDOS split owing to the different bond length of Fe-Te and Fe-Se.	56

3.6	The individual contributions of (a) xy , (b) yz/xz , (c) $3z^2-r^2$ and (d) x^2-y^2 orbitals to Fe 3d partial DOS for FeTe, FeSe _{0.5} Te _{0.5} and FeSe. Inset of (b) represents the expanded PDOS near E_F for yz (solid lines) and xz (dotted green line, for FeSe _{0.5} Te _{0.5}) orbitals. The reduced symmetry in case of FeSe _{0.5} Te _{0.5} lifts the degeneracy of xz and yz orbitals, thus the PDOS contribution splits which is otherwise same in case of FeTe and FeSe.	58
3.7	(a) Enlarged view of high resolution PES spectra measured at 300 K (black) and 77 K (red) for FeSe _{1-x} Te _x ($x = 1, 0.5, 0$) . (b) PES spectra in the energy range -0.8 -0.2 eV.	59
3.8	Temperature dependent IPES spectra taken at 300 K (black) and 77 K (red) for FeSe _{1-x} Te _{1-x} ($x = 1, 0.5, 0$)	60
3.9	PES spectrum (solid lines) measured using He I (21.2 eV) below the Fermi level (dashed vertical line) and IPES spectra (dots+lines) at 9.2 eV photon energy above Fermi level for FeSe _{1-x} Te _x ($x = 1, 0.5, 0$). The black and red spectra correspond to data taken at 300 K and 77 K respectively.	61
3.10	Comparison of HeI and HeII spectra for FeSe _{1-x} Te _x ($x = 1, 0.5, 0$) measured at 300 K (black) and 77 K (red).	62
3.11	The PES and IPES spectra below and above the Fermi level respectively, for FeTe (black), FeSe _{0.5} Te _{0.5} (blue) and FeSe (red). The black ticks correspond to the positions of A1 and B.	62
4.1	Crystal structure of REFePnO depicting two unit cells. Grey, blue, red and green spheres correspond to RE, O/F, Fe and Pn atoms, respectively.	72
4.2	(a) He II Valence band photoemission spectra for NdFeAsO (black) and NdFeAsO _{0.8} F _{0.2} (red) showing two major features A and B. (b) The density of states calculation for NdFeAsO with the marked positions A and B corresponding to the experimental features.	73
4.3	Calculated partial density of states of NdFeAsO.	74
4.4	The high resolution photoemission spectra for NdFeAsO (black) and NdFeAsO _{0.8} F _{0.2} (red) using He I (bottom panel) and He II (top panel) energy.	75

4.5	The high resolution photoemission spectra at 300 K (black) and 77 K (red) using He I (21.2 eV) source for (a) NdFeAsO (b) NdFeAsO _{0.8} F _{0.2} . The He II (40.8 eV) photoemission spectra at 300 K (black) and 77 K (red) for (c) NdFeAsO and (d) NdFeAsO _{0.8} F _{0.2}	76
5.1	Crystal structure of SrFBiS ₂ depicting two unit cells. Grey, green, purple and orange spheres correspond to Sr/RE, F, Bi and S atoms, respectively.	87
5.2	He II photoemission spectra for SrFBiS ₂ (black), Sr _{0.5} Ce _{0.5} BiS ₂ (blue) and Sr _{0.5} La _{0.5} BiS ₂ , with marked experimental features A, B and C. The sub features of A, a and a' are also marked.	88
5.3	The calculated DOS for Sr _{0.5} RE _{0.5} BiS ₂ with U = 5.0 eV, J = 0.7 eV (a), U = J = 0 (b) with the marked theoretical features.	89
5.4	Calculated partial DOS for (a) SrFBiS ₂ , (b) Sr _{0.5} Ce _{0.5} BiS ₂ , (c) Sr _{0.5} La _{0.5} BiS ₂ . Vertical dashed line corresponds to Fermi level.	90
5.5	Calculated band structure for (a) SrFBiS ₂ , (b) Sr _{0.5} Ce _{0.5} BiS ₂ , (c) Sr _{0.5} La _{0.5} BiS ₂	90
5.6	(a) High resolution He I photoemission spectra for SrFBiS ₂ (black), Sr _{0.5} Ce _{0.5} BiS ₂ (blue), (c) Sr _{0.5} La _{0.5} BiS ₂ (red) (b) High resolution He I photoemission spectra at 300 K (black) and 77 K (red) for SrFBiS ₂ (a), Sr _{0.5} Ce _{0.5} BiS ₂ (b), Sr _{0.5} La _{0.5} BiS ₂ (c). Dashed vertical line corresponds to E _F	92
6.1	(a) Crystal structure of GeSe with two unit cells. Red and blue dots correspond to Germanium and Selenium atoms respectively. Ge1, Ge2, Ge3 and Ge4 correspond to first, second, third and fourth nearest neighbours respectively. The dashed line shows the cleavage plane along x-y plane. (b) The surface Brillouin zone, showing the high symmetry directions (red lines) of the GeSe single crystal. (c) LEED pattern taken at 120 eV, with bright spots arranged in rectangular fashion indicating the rectangular symmetry of the Brillouin zone. The marked directions (black lines) in the LEED image correspond to the symmetry directions shown in fig b (marked by red lines).	100
6.2	GeSe local bonding picture representing the p orbitals of Se atom (blue) along with the p orbitals of the neighbouring Ge atom (red). These atoms correspond to the same ones shown in fig 1(a).	101

6.3	LDA density of states representing the s and p orbital contributions of Ge and Se atoms to the total density of states.	102
6.4	The core level spectra corresponding to Ge 3d, Se 3d, Ge 3p and Se 3p levels shown in fig (a), (b), (c) and (d) respectively.	102
6.5	Valence band region marked with prominent features probed using (a) Mg $K\alpha$ source (b) He I. The dashed lines correspond to the Fermi Level.	103
6.6	(a)EDC from ARPES on GeSe along Γ -Z direction of its Brillouin zone. The polar angle theta for Γ point and Z point (curves represented by thick black bold lines) is marked in the figure.Dotted line represents the Fermi level (b) Intensity plot of binding energy as a function of parallel component of momentum ($K_{ }$) representing the band dispersion. Vertical dotted lines correspond to Γ point and Z point while the horizontal dotted line represents the Fermi level.	104
6.7	ARPES spectra along Γ -Y direction represented in form of (a) EDC (b) intensity plot. Vertical lines in (b) represent the Γ point and Y point.	105
6.8	ARPES spectra along Γ -T direction represented in form of (a) EDC (b) intensity plot. Vertical lines in (b) represent the Γ point and T point.	105
6.9	The second derivative of intensity plot, $\partial^2 I / \partial E^2$ versus momentum component parallel to the sample surface, along (a) Γ -Z, (b) Γ -Y and (c) Γ -T directions of the Brillouin zone. Vertical dashed lines correspond to the high symmetry points.	106
6.10	Energy versus momentum component parallel to the sample surface ($E(k)$ vs $K_{ }$) representing the experimental data points (red circles) superposed on calculated band structure plot (black curves) along (a) Z- Γ -Z, (b) Y- Γ -Y and (c) T- Γ -T directions of the Brillouin zone. The fatness of band for GeSe calculated for (d) Se-4p orbitals and (e) Ge-4p orbitals. Black, red and blue denotes Se- p_x , p_y and p_z orbitals respectively while green, cyan and magenta denotes Ge- p_x , p_y and p_z orbitals respectively.	107

Chapter 1

Introduction

1.1 Layered Materials :

The advent of graphite based materials led to plethora of research in the field of layered materials in the quest for other alternative two dimensional (2D) layered materials. The anisotropy in structural, electrical and magnetic properties exhibited by these materials have been the topic of extensive research for solid state chemist, physicist and engineers [1]. The layered materials have paved the path way for the development of intercalation chemistry which has evolved into the field of topochemical reactions facilitating the synthesis of several kinetically stable products, which was difficult to grow using other growth techniques. This field has attracted physicists to unfold the origin and mechanism of various exotic phenomena which exist in these systems like spin and charge density, topological insulating state, quantum spin hall (QSH) effect, superconductivity, colossal magnetoresistance (CMR), metal insulator (MI) transition etc. . Engineers and scientists are also captivated towards these materials due to their amazing technological applications in electronics, sensing, photonics, catalysis, bioengineering, energy harvesting, and flexible electronics [2]. Modification of these materials achieved by chemical doping, pressure application and intercalation leads to unique and diverse properties enhancing their utilisation in technological applications. The layered materials can be used as building blocks for synthesis of various 3D structures with precisely tailored properties.

The basic structure of layered materials consists of stacks of 2-D sheets with strong in-plane covalent bonding and weak interlayer Vander Waal's interaction. Many of the physical and chemical properties of these materials owe its origin to the anisotropic layered structure with different interlayer and intralayer bonding. Due to the weak interlayer bonding, the layered materials possess a cleavage plane reducing it into a quasi-2D system. Examples of 2D

layered materials include graphite, hexagonal boron nitride (h-BN), chalcogenides, manganites, titanates, cobaltates, superconductors and topological insulators to name a few. All these materials are interesting on their own right, namely, they present correlated electronic states where charge, spin, orbital, lattice degrees of freedom play an important role. The broad range of compositions of layered materials and the endless possibilities of combining them in heterostructures give rise to a rich spectrum of properties ranging from insulators through semiconductors to superconductors and the recently discovered topological insulators. Despite the exploration of numerous layered compounds, there still exist a universe of 2D crystals with its own beauty and purpose, waiting to be discovered and studied.

The present thesis deals with some layered superconductors and semiconductors. The layered materials included in the thesis are Fe chalcogenide ($\text{FeSe}_{1-x}\text{Te}_x$), Fe pnictide ($\text{NdFeAsO}_{1-x}\text{F}_x$), rare earth (La,Ce) doped SrFBiS_2 superconductors and chalcogenide semiconductor (GeSe). The subsequent sections shall cover the materials used in the thesis.

1.2 Layered Superconductors:

Since the discovery of the phenomenon of superconductivity in 1911 by Heike Kamerlingh Onnes [3], it still remains an unsolved puzzle with missing pieces. The whole range of intriguing and often surprising properties discovered in this field drives physicists to unwind the mystery behind the origin and mechanism of superconductivity. The phenomenon of superconductivity remained confined to very low-temperatures until the discovery of high- T_c superconductivity ($T_c \sim 30$ K) in layered La-Ba-Cu-O ceramics by Bednorz and Muller in 1986 [4]. This paved the path way for synthesis of numerous high T_c superconducting cuprates. In 1993 the highest T_c of ~ 135 K was achieved in Hg based cuprates [5]. The synthesis of cuprates also laid a platform for the exploration of several other layered superconducting materials. In 2008, the discovery of $\text{LaFeAsO}_{1-x}\text{F}_x$ [6] with T_c of ~ 26 K, ushered into a new arena of superconductors, namely the Fe based superconductors. The existence of superconductivity in Fe based compounds was quite puzzling on account of the antagonistic relationship between superconductivity and magnetism. These systems generated a great interest among researchers opening a new route for the high- T_c research in additon to that of the cuprates [7]. However, it also posed new challenges on both experimental and theoretical sides and added a new problem for physicists in addition to the longstanding problem of cuprates. This new class of iron-based

systems share some common properties with cuprates such as the layered crystal structures, 3d electrons participation and antiferromagnetic (AFM) ordering in the parent compounds. However, many differences exist between the two classes especially in their electronic structures. The parent compound of iron based superconductors are bad metals on contrary to the Mott insulating nature of the parent compound of cuprates. Moreover, the properties of iron based superconductors exhibit a lower anisotropy in comparison to the cuprates. The Fe superconductors are classified into two broad categories namely pnictides, containing pnictogen atom (As,P) and chalcogenides, containing chalcogen atom (Se,Te). However, on the basis of crystal structure these are categorised into four families. The different families of Fe superconductors are discussed below:

(1) 1111 family:

The reports on LaFePO with $T_c \sim 5-7$ K by Kamihara et al. [8] laid the first step to the exploration of the (1111) family of superconductors with general formula LnFeAsO (Ln= rare earth atom). The highest T_c achieved in this family is ~ 56 K for $\text{Gd}_{1-x}\text{Th}_x\text{FeAsO}$ [9]. Other members of this family include $\text{SmFeAsO}_{1-x}\text{F}_x$ ($T_c = 43$ K), $\text{CeFeAsO}_{1-x}\text{F}_x$ ($T_c \sim 41$ K), $\text{NdFeAsO}_{1-x}\text{F}_x$ ($T_c \sim 51$ K) and $\text{PrFeAsO}_{1-x}\text{F}_x$ ($T_c \sim 52$ K) [10].

(2) 122 family :

The proposition of BaFe_2As_2 , as a new superconductor, by M. Rotter [11] led to the search of new compounds with the formula AEFe_2As_2 (AE = Alkaline Earth element). His proposition was based on the structural similarity of this compound with the LaFeAsO compounds. The partial replacement of Barium with Potassium (hole doping) induced superconductivity at 38 K in the first member of the family, $\text{Ba}_{0.6}\text{K}_{0.4}\text{Fe}_2\text{As}_2$ [12]. Subsequently, several other compounds with doping of Strontium, Calcium, Europium, Sodium, Cesium, Cobalt etc. were reported [10]. Till date, the T_c of ~ 38 K, exhibited by $\text{Ba}_{0.6}\text{K}_{0.4}\text{Fe}_2\text{As}_2$, remains the highest in this family.

(3) 111 family :

The reports of C. Wang et al. [13] opened up the family of 111 family of Fe superconductors, with the discovery of LiFeAs. The highest T_c , reached is ~ 18 K. The other member of this family is NaFeAs.

(4) 11 family :

FeSe with $T_c \sim 8$ K [14] is the first member of the 11 family. The members of this family are represented by general formula $\text{Fe}(\text{Se}_{1-x}\text{A}_x)$, where $\text{A} = \text{Te}, \text{S}$; $(\text{Fe}_{1-x}\text{A}_x)\text{Se}$, where $\text{A} = \text{Co}$,

Ni; $\text{Fe}(\text{Te}_{1-x}\text{A}_x)$, where $\text{A} = \text{S}$ $\text{FeSe}_{0.5}\text{Te}_{0.5}$ exhibits the maximum T_c of ~ 15 K [15] in this family.

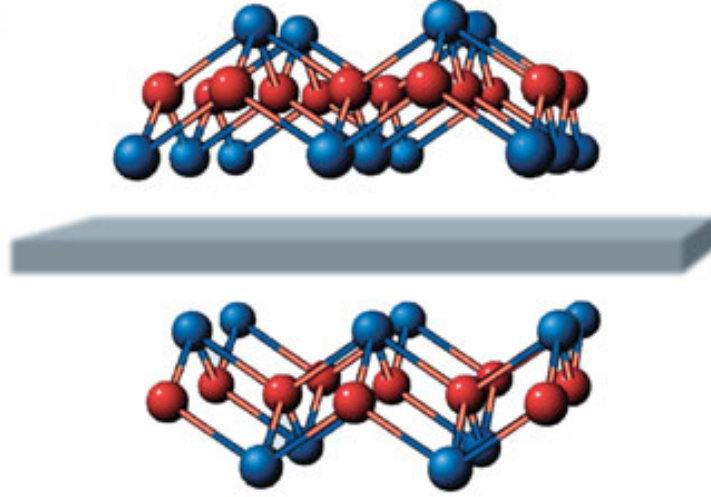


Figure 1.1: Prototypical crystal structure of iron based superconductors [16]. Red spheres correspond to Fe atoms while the pnictogens/chalcogens are shown as blue spheres. The filler layer is represented as grey slab.

Despite the differences in electronic properties and behaviour of each distinct class, all of them share a common structural motif comprising of stacks of edge sharing FeQ_4 tetrahedra. Q is a pnictide or chalcogenide atom. All the compounds exist in tetragonal crystal structure at room temperature. The schematic of general crystal structure, displayed in Fig 1.1 shows a filler layer sandwiched between two $(\text{Fe-Q})_4$ tetrahedral layer. For 1111 family the spacer layer consist of RE-O (RE is rare earth atom) atoms. For the 122 and 111 layer, the alkaline atoms (Ba, Sr etc) and alkali atoms (Li) act as spacer layer respectively. The 11 family contains no spacer layer. This thesis deals with a member of 1111 family, $\text{NdFeAsO}_{1-x}\text{F}_x$ and a member of 11 family, $\text{FeSe}_{1-x}\text{Te}_x$. Hence, these two compounds shall be discussed in detail in the subsequent paragraphs.

1.2.1 Fe chalcogenides, $\text{FeSe}_{1-x}\text{Te}_x$

Among the various layered superconductors, the Fe chalcogenides $\text{FeSe}_{1-x}\text{Te}_x$, are one of the most well studied system owing to their simple structure and puzzling electronic and physical properties. These materials, at ambient temperature, adopt the anti-PbO tetragonal structure made up of layers of FeCh_4 (Ch = chalcogen) tetrahedra (shown in Fig 1.2). The chalcogen-Fe-chalcogen angle (α) and chalcogen height Z_c is sensitive to doping. An enhancement of

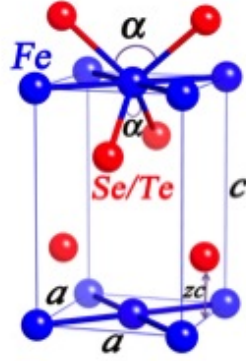


Figure 1.2: Crystal Structure of Fe(Se,Te). The blue and red spheres correspond to Fe and Se/Te atoms respectively. α represents the Se/Te-Fe-Se/Te bond angle and Z_c is the chalcogen height defined as the height of Se/Te atoms from the Fe plane.

α and reduction in Z_c occurs due to Se doping in FeTe. Despite their simple structure, Fe chalcogenides display complex phase diagrams and their electronic and magnetic behaviour is very sensitive to small variations in composition, defects distribution, external and/or chemical pressure. All these features make these systems the ideal playground for theoretical and experimental investigations. A recent advancement in this field is the observation of superconductivity with T_c above 100 K in single layer FeSe films on doped SrTiO₃ which turns insulating with the addition of one more layer [17]. This unusual behavioral difference between single and double layer films of FeSe is a signature of strong electron correlation which has been experimentally observed [18].

The parent, nonsuperconducting, antiferromagnetic compound α -FeTe exists in tetragonal ($P4/nmm$) phase at room temperature and shows a structural phase transition at $T_S \sim 60-75$ K [19]. The electronic properties of the low temperature phase is composition dependent. As a function of Fe deficiency, there exists two distinct type of transport behaviours in the low temperature phase. Fe_{1.076}Te, exhibits a transition from semiconducting to metallic phase, accompanied by tetragonal to monoclinic ($P2_1/m$) transition at 75 K. While Fe_{1.141}Te, remains semiconducting but shows a tetragonal to orthorhombic (Pmmn) phase transition at 63 K. The magnetic transition occur simultaneously at the structural transition for both the compositions. The samples used in this thesis are polycrystalline FeTe sample, with no excess Fe, exhibiting a semiconducting to metallic transition accompanied by a structural transition at 80 K [20]. As reported by Okada et al. [21] FeTe shows no sign of superconductivity even at higher pressure of 19 GPa. However, a shift of structural transition to lower temperature was observed due to application of pressure. The FeTe compound shows an ordering of spin density wave (SDW),

below the antiferromagnetic transition, which involves the development of a superstructure in the form of a periodic modulation in the electronic spin density. If the new periodicity is a rational fraction or multiple of the lattice constant, the density wave is said to be commensurate; otherwise the density wave is termed incommensurate. The $\text{Fe}_{1.141}\text{Te}$ compound shows an incommensurate spin density wave with commensurate value $\delta = 0.38$, while the $\text{Fe}_{1.076}\text{Te}$ compound shows a commensurate spin density wave, with commensurate value $\delta = 0.5$.

The first observation of superconductivity in FeSe with $T_c \sim 8$ K, was reported by Hsu et al. [14]. Pressure application leads to enhancement of T_c up to 37 K [22]. Despite the existence of several forms of FeSe, superconductivity occurs only for β -FeSe, which has a narrow stability range from $\text{Fe}_{1.01}\text{Se}$ to $\text{Fe}_{1.02}\text{Se}$. The highest transition temperature $T_c \sim 9$ K has been observed for the composition with stoichiometry $\text{Fe}_{1+\delta}\text{Se}$, with $\delta = 0.1$. Increasing the Fe content leads to decrease in T_c to nearly 5 K for $\delta = 0.2$, whereas superconductivity is completely suppressed for compositions $\delta \geq 0.3$. FeSe exhibits a structural transition from tetragonal to orthorhombic (Cmma) phase at 70-90 K [23]. The structural transition is not accompanied by any magnetic transition.

For the optimal doping of 0.5, the T_c reported is nearly 15.2 K for $\text{FeSe}_{0.5}\text{Te}_{0.5}$ [24]. This enhancement is reported to be linked to the local structural symmetry breaking [25] and the degree of disorder caused by the smaller ionic radius of Se [15]. This compound shows no signature of magnetic or structural transition.

1.2.2 Nd based pnictides, $\text{NdFeAsO}_{1-x}\text{F}_x$

The high T_c exhibited by the Fe pnictides of (1111) family, has generated enormous research in this family, with an aim to synthesize Fe superconductors with higher T_c , and has led to the discovery of various layered oxy-pnictides [10]. Amongst various layered oxypnictides, the Nd based superconductors, with an unpaired 4f electron and T_c of ~ 50 K has gained special interest among researchers. The oxygen deficiency in NdFeAsO raises the T_c to nearly 54 K [26]. The interaction of Nd magnetic moment generated due to the unpaired 4f electrons with the FeAs layer gives rise to exotic phenomena observed in this system [27]. The crystal structure of $\text{NdFeAsO}_{1-x}\text{F}_x$ superconductor consists of alternate stacks of Fe-As layer and Nd-O/F layers with eight atoms in a tetragonal (space group P4/nmm) unit cell (shown in Fig 1.3).

The Fe-As-Fe layer is responsible for superconductivity while the Nd-O/F layer is the

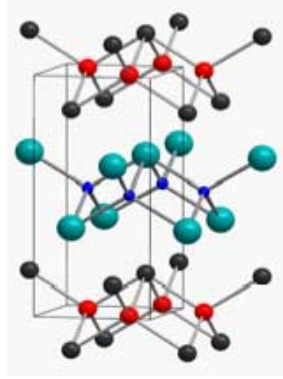


Figure 1.3: Crystal Structure of NdFeAsO(F). The cyan, red, black and blue spheres correspond to Nd, Fe As and O/F atoms respectively. Nd-O/F atoms form the spacer layer in between the two Fe-As layer. The parameters α and Z_c are also defined in the same manner as in Fe chalcogenides.

charge carrier supplying layer. The Fe-pnictogen-Fe angle (α) and the height of pnictogen atom from the Fe plane (Z_c) is sensitive to F doping. The parent compound, NdFeAsO is an antiferromagnetic, nonsuperconductor and exhibits structural transition from tetragonal to orthorhombic structure at 150 K. F doping at O site, causes emergence of superconductivity by suppressing the spin density wave order, with a T_c of ~ 50 K [28].

1.2.3 Electronic properties of Fe-superconductors

The electronic structure of Fe superconductors, derived from the Fe 3d-states hybridized with Pn/Ch p-orbital derived bands are characterized by bad metallicity, low carrier concentration and high electronic density of states near Fermi level. The electronic properties are controlled by the electron correlations arising from the competing inter- and intra-orbital interactions near the E_F region [29]. In addition, the geometry of edge sharing Fe-(Ch/Pn)₄ tetrahedral unit, particularly, the Pn/Ch-Fe-Pn/Ch angles and anion height are important parameters in tuning the electronic properties of these systems and determining T_c [29, 30]. The degree of correlations in Fe superconductors have been highly debatable. Fermi surface instabilities, itinerant electrons and renormalized Fermi liquid support the weak correlations [31–34] while localised electrons, magnetic superexchange, bad metallicity, non-Fermi liquid and Hund's metals suggest the strong correlations [35–38]. The multiorbital correlation in combination with Hund's coupling caused by the participation of all the five Fe 3d electrons result in some exotic electronic properties like orbital selectivity [39, 40], Mottness [41], quantum phase transition [42], nematicity [43], pseudogap [44] etc. It is well known that the multiband systems are char-

acterized by a strong interplay between lattice, electronic and magnetic degrees of freedom which govern the electronic density of states near the Fermi level. Hence, the exploration of the density of states near Fermi level is necessary to unwind the origin and mechanism of superconductivity and other exotic properties observed in FeSCs.

In multiorbital systems, the physics of metal to insulator transition (MIT) may be orbital sensitive and the first experimental observation of the orbital selectivity occurred in $\text{Ca}_{2-x}\text{Sr}_x\text{RuO}_4$ [45] and was later discovered in iron based superconductors [46, 47]. The moderate electron correlations controlled by the competing inter- and intra-orbital interactions near the E_F region generates Orbital Selective Mott Phase (OSMP) in which electrons in some orbitals are Mott localized, while others remain itinerant [39, 41, 48, 49]. A doping dependent OSMP was proposed theoretically in Fe superconductors by Craco et al. and Aichhorn et al. [50, 51] and later on discovered in $\text{A}_x\text{Fe}_{2-y}\text{Se}_2$ [46, 47, 52].

Pseudogap, the term first coined by Neville Mott in 1986, indicates a minimum in the density of states at the Fermi level, $N(E_F)$, resulting from Coulomb repulsion between electrons in the same atom, a band gap in a disordered material or a combination of these. The phenomenon of pseudogap was first detected in the temperature dependence of the spin-lattice relaxation and Knight shift in nuclear magnetic resonance and magnetic susceptibility studies [53]. The pseudogap in high temperature superconductors (HTSC) [54] fascinated the scientific community and presently the pseudogap phenomenon has been extended to other systems like Fe superconductors [55], manganites [56], Kondo insulators [57], thin films of conventional superconductors [58], Co-Fe based half metals [59], ultracold Fermi gases [60]. The signature of pseudogap can be observed in experiments like specific heat, resistivity, ARPES, optics, Raman scattering, inelastic neutron scattering, resonant inelastic X-ray scattering, tunneling spectroscopy, nuclear magnetic resonance to name a few [55]. Photoemission studies on Fe superconductors confirm the existence of pseudogap [61–64].

The pairing mechanism in Fe superconductors has been much debatable and topic of extensive research. The nature of pairing mechanisms have been proposed by various researchers. Theoretically, phonon mechanism [65] was ruled out and spin fluctuation mediated pairing [66, 67] was proposed as a mechanism for the emergence of superconductivity in the family of Fe superconductors. It has been proposed [68] that the nesting between disconnected Fermi surface pockets can induce spin fluctuations associated with the nesting vector. This can lead to a s wave superconducting gap which changes sign between various pockets, hence termed as

s_{\pm} wave or sign-reversing s-wave first proposed by Mazin et al. [66]. Further d-wave pairing is also considered a candidate in the Fe superconductors [67,69]. Many researchers [70,72] have reported a sign-reversing s wave that has nodes intersecting the Fermi surface which competes with the d-wave pairing. It has been predicted theoretically [73] that the nodal s-wave pairing is intrinsic to the iron pnictide semiconductors, while a full gap can occur due to the presence of impurities. Experimentally, the fully gapped, sign reversing s-wave scenario is consistent with ARPES measurements [74,75].

1.2.4 BiS₂ based superconductors

The observation of unconventional pairing mechanism in layered superconductors due to the reduced dimensionality, has generated tremendous amount of exploration in this field in the past few decades. In 2012, a new layered superconductor with a BiS₂ based superconducting layer which is structurally similar to the cuprates and Fe superconductors, was discovered [76]. LaO_{0.5}F_{0.5}BiS₂ exhibits the highest T_c of ~ 11 K in this family. [77]. These superconductors, composed of alternate stacking of superconducting BiS₂ layers and blocking layers, exist in tetragonal structure. There exists three types of BiS₂ superconductors depending on the type of blocking layers as shown in Fig 1.4.

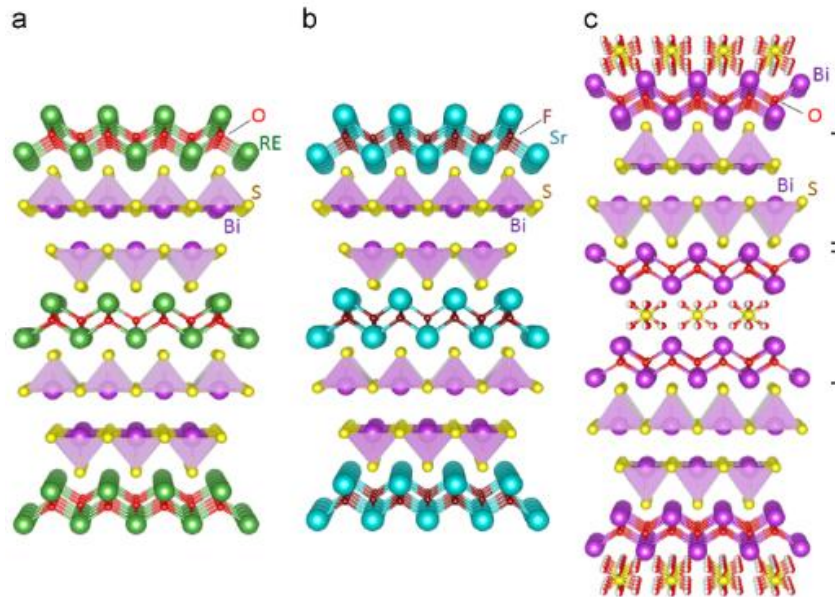


Figure 1.4: Crystal Structure of (a) ReOBiS₂, (b) SrFBiS₂ and (c) Bi₄O₄(SO₄)Bi₂S₄ structures.

In REOBiS₂ type structure (fig 4(a)), the blocking layer consists of REO (RE : La, Ce, Pr, Nd, Yb) atoms. The conducting carriers can be controlled by partial substitution of Fluorine

at Oxygen site or the RE substitution by the M^{4+} ions (M : Th, Hf, Zr, Ti) [78]. Replacement of the REO blocking layers by the SrF layers lead to SrFBiS₂ structure [79]. In this structure, the carrier concentration at the BiS₂ layers can be tuned by the partial substitution of Sr by RE elements like La, Ce, Nd, Pr and Sm [78]. The REO and SrF blocking layers are quite similar to the Fe based superconductors LaFeAsO [6] and SrFeAsF [80]. The last structure, the Bi₄O₄(SO₄)Bi₂S₄, with some defects in the SO₄ site, causes generation of electron carriers within the BiS₂ layers [81]. The superconducting phase in this family is Bi₄O₄(SO₄)_{1-x}Bi₂S₄. The undoped parent compounds are semiconducting in nature while resistivity decreases with the emergence of superconductivity in the doped compounds.

1.2.5 Electronic properties of BiS superconductors

The two dimensional Fermi surface composed of Bi $p_{x/y}$ orbitals, controls the major electronic properties [82] of BiS superconductors. As a function of doping, the Fermi surface evolves from X-Y pockets encircling the mid points on the edge of the Brillouin zone (BZ) to the Γ -M pockets encircling the centre and corner of the BZ via a Lifshitz transition [83] which occurs at doping $x = 0.5$. Below the Lifshitz filling level, a nodeless gap and weak topological superconducting state exists while above the Lifshitz points, the gap becomes nodal [83]. The pairing symmetry in this family remains controversial. Due to the weak correlation of the extended p orbitals and low T_c , electron phonon coupling was suggested to play a significant role in the Cooper pairing [84, 85]. Magnetic penetration depth measurement is consistent with the s wave pairing symmetry [86] In contrast to the conventional superconductivity scenario, weak Fermi surface nesting and smaller Fermi pockets in ARPES measurement [87, 88] suggest strong correlation effects. Further, the neutron scattering experiment and larger ratio of $2\Delta/T_c$ indicates a weaker electron phonon coupling [89, 90]. Thus, electron correlations were assumed to be the driving force for superconductivity [91–94]. A dominant triplet pairing with a sub dominant singlet component, arising from the spin orbit coupling of Bi atoms, exist in these systems [95].

1.3 Layered Semiconductors

Over the past decade, semiconducting materials have regained impetus in research owing to their scientific aspect and technological development. Semiconductors are the most attractive

class of materials for functional nanodevices, including gas and biological sensors, field effect transistor, light emitting diodes, solar cells, nanogenerators and optoelectronic devices [96]. Among the variety of layered semiconductors, the chalcogenide semiconductors have gained tremendous attraction in the scientific community. Chalcogenide is a chemical compound consisting of at least one element from the group 16 specially sulphides, selenides and tellurides. 2D layered chalcogenides exhibit a broad range of electronic properties ranging from insulators to semiconductors, from metals to superconductors and the recently discovered topological insulators.

1.3.1 Germanium Selenide (GeSe) :

GeSe, a p-type narrow band gap ($E_g = 1.1$ eV) layered semiconductor, exists in orthorhombic ($Pnma$) rock-salt structure as shown in Fig 1.5. A single unit cell contains eight atoms situated in two adjacent double layers along the z axis. The atoms in each double layer are bonded to their three nearest neighbours in a zig-zag fashion. The layer structure of GeSe single crystal provides a cleavage plane facilitating Angle resolved Photoemission (ARPES) measurements. GeSe shows strong anisotropic properties due to the layered structure.

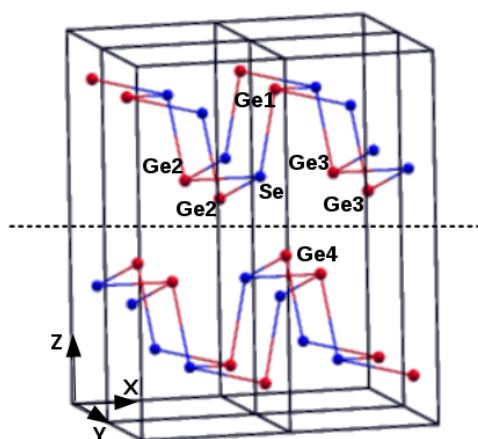


Figure 1.5: Crystal structure of GeSe with two unit cells. Red and blue spheres correspond to germanium and selenium atoms respectively. Ge1, Ge2, Ge3 and Ge4 correspond to first, second, third and fourth nearest neighbours respectively. The dashed line shows the cleavage plane along xy plane.

GeSe occurs in two polymorphic phases, a stable orthorhombic phase (α phase) at low temperature and a cubic phase (β phase) at high temperature beyond 656° C. The small band gap of GeSe enables its use in the solar cell industry and photovoltaics. In addition, Ge based

semiconductors are potential alternatives to their counterparts, such as narrow band-gap systems containing Pb, Cd and Hg due to the advantages of their relatively higher stability and environmental stability [97].

The presence cation s states, hybridized with the cation p and anion p contributions, defines the physical properties of the IV-VI semiconductors [98,99]. The physical properties of orthorhombic IVVI materials possess a striking resemblance among themselves [100, 101]. Thus, the study of the valence band behaviour near valence band maximum shall accurately describe the electronic and physical properties of IV-VI semiconductors. GeSe, as a prototypical example of this family has been chosen to study the detailed electronic structure of the IV-VI semiconductors. The previously reported experimental work on GeSe covers angle integrated photoemission, high resolution electron energy loss, transmittance, reflectance, thermoreflectance, refraction index, photoconductivity, photoelectron partial-yield and constant-initial-state (CIS) spectra and x-ray powder diffraction plus Raman spectroscopy (for structural, vibrational and electronic properties related to compression mechanisms) [102]

The thesis is organised in the following manner. Chapter 2 discusses the various experimental techniques utilized in this thesis. The electronic structure study of $\text{FeSe}_{1-x}\text{Te}_x$ using UV Photoemission and Inverse Photoemission, in conjugation with band structure calculations have been presented in chapter 3. The photoemission study of $\text{NdFeAsO}_{1-x}\text{F}_x$ and Rare Earth (La, Ce) doped SrFBiS_2 superconductors have been discussed in chapter 4 and 5 respectively. Chapter 6 deals with the electronic structure study of GeSe single crystal using Angle resolved Photoemission Spectroscopy and X-Ray Photoemission Spectroscopy. The summary is presented in chapter 7.

Bibliography

- [1] D. Johnson, S. Clarke, J. Wiley, and K. Koumoto, *Semicond. Sci. Technol.* **29**, 060301 (2014).
- [2] A. B. Kaul, *J. Mater. Res.* **29**, 348 (2014).
- [3] H. K. Onnes: *Leiden Comm.* 120b, 122c, 124c (1911).
- [4] J. G. Bednorz, and K.A. Müller: *Z. Phys. B* **64**, 189 (1986).
- [5] A. Schilling, M. Cantoni, J.D. Guo, and H.R. Ott, *Nature* **363**, 56 (1993).
- [6] Y. Kamihara, T. Watanabe, M. Hirano, and H. Hosono, *J. Am. Chem. Soc.* **130**, 3296 (2008).
- [7] D. C. Johnston, *Advances in Physics* **59**, 803 (2010).
- [8] Y. Kamihara, H. Hiramatsu, M. Hirano, R. Kawamura, H. Yanagi, T. Kamiya, and H. Hosono, *J. Am. Chem. Soc.* **128**, 10012 (2006).
- [9] C. Wang, L. Li, S. Chi, Z. Zhu, Z. Ren, Y. Li, Y. Wang, X. Lin, Y. Luo, S. Jiang, Z. Xu, G. Cao, and Z. Xu, *Euro Phys. Lett.* **83**, 67006 (2008).
- [10] P. M. aswathy, J. B. Anooja, P. M. Sarun, and U. Syamaprasad, *Supercond. Sci. Technol.* **23**, 073001 (2010)
- [11] M. Rotter, M. Tegel, I. Shellenberg, W. Hermes, R. Pottgen, and D. Johrendt, *Phys. Rev. B* **78**, 020503 (2008).
- [12] M. Rotter, M. Pangerl, M. Tegel, and D. Johrendt, *Angewandte Chemie International Edition* **47**, 7949 (2008).

- [13] X. C. Wang, Q. Q. Liu, Y. X. Lv, W. B. Gao, L. X. Yang, R. C. Yu, F. Y. Li, and C. Q. Jin, *Solid State Communications* **148**, 538 (2008).
- [14] F. -C. Hsu, J. -Y. Luo, K. -W. Yeh, T. -K. Chen, T. -W. Huang, P. M. Wu, Y. -C. Lee, Y. -L. Huang, Y. -Y. Chu, D. -C. Yan, and M. -K. Wu, *Proc. Natl. Acad. Sci. USA* **105**, 14262 (2008).
- [15] K. -W. Yeh, T. -W. Huang, Y. L. Huang, T. -K. Chen, F. -C. Hsu, P. M. Wu, Y. -Y. Lee, Y. -Y. Chu, C. -L. Chen, J. -Y. Luo, D. -C. Yan, and M. -K. Wu, *Europhys. Lett.* **84**, 37002 (2008).
- [16] I. I. Mazin, *Nature* **464**, 183 (2010).
- [17] J. -F. Ge, Z. -L. Liu, C. Liu, C. -L. Gao, D. Qian, Q. -K. Xue, Y. Liu, and J. -F. Jia, *Nature Materials* **14**, 285 (2015).
- [18] J. J. Lee, F. T. Schmitt, R. G. Moore, S. Johnston, Y.-T. Chi, W Li, M. Yi, Z. K. Liu, M. Hashimoto, Y. Zhang, D. H. Lu, T. P. Devereaux, D. -H. Lee, and Z.-X Shen, *Nature* **515**, 245 (2014).
- [19] W. Bao, Y. Qiu, Q. Huang, M. A. Green, P. Zajdel, M. R. Fitzsimmons, M. Zhernenkov, S. Chang, M. Fang, B. Qian, E. K. Vehstedt, J. Yang, H. M. Pham, L. Spinu, and Z. Q. Mao, *Phys. Rev. Lett.* **102**, 247001 (2009).
- [20] V. P. S. Awana, A. Pal, A. Vajpayee, B. Gahtori, and H. Kishan, *Physica C* **471**, 77 (2011).
- [21] H. Okada, H. Takahashi, Y. Mizuguchi, Y. Takano, and H. Takashi, *J. Phys. Soc. Jpn.* **78**, 083709 (2009).
- [22] Y. Mizuguchi, F. Tomioka, S. Tsuda, T. Yamaguchi, and Y. Takano, *Appl. Phys. Lett.* **93**, 152505 (2008).
- [23] S. Margadonna, Y. Takabayashi, M. T. McDonald, K. Kasperkiewicz, Y. Mizuguchi, Y. Takano, A. N. Fitch, E. Suard, and K. Prassides, *Chem. Commun.* 5607 (2008).
- [24] K. -W. Yeh, T. -W. Huang, Y. -L. Huang, T. -K. Chen, F. -C. Hsu, P. M. Wu, Y. -C. Lee, Y. -Y. Chu, C. -L. Chen, J. -Y. Luo, D. -C. Yan, and M. -K. Wu, *Europhys. Lett.* **84** 37002 (2008).

- [25] B. Joseph, A. Iadecola, A. Puri, L. Simonelli, Y. Mizuguchi, Y. Takano, and N.L. Saini Phys. Rev. B **82**, 020502 (2010).
- [26] H. Kito, H. Eisaki, A. Iyo, J. Phys. Soc. Jpn. **77**, 063707 (2008).
- [27] P. Jeglič, J. -W. G Bos, A. Zorko, M. Brunelli, K. Koch, H. Rosner, S. Margadonna, and D. Arčon, Phys. Rev. B **79**, 094515 (2009).
- [28] Y. Qiu, W. Bao, Q. Huang, T. Yildirim, J. M. Simmons, M. A. Green, J.W. Lynn, Y. C. Gasparovic, J. Li, T. Wu, and X. H. Chen, Phys. Rev. Lett. **101**, 257002 (2008).
- [29] T. Miyake, K. Nakamura, R. Arita, and M. Imada, J. Phys. Soc. Japan **79**, 044705 (2010).
- [30] V. Vildosola, L. Pourovskii, R. Arita, S. Biermann, and A. Georges, Phys. Rev. B **78**, 064518 (2008).
- [31] S. Raghu, X. -L. Qi, C. -X Liu, D. J. Scalapino, and S.-C. Zhang, Phys. Rev. B **77**, 220503 (2008).
- [32] I. I. Mazin, M. D. Johannes, L. Boeri, K. Koepernik, and D. J. Singh, Phys. Rev. B **78**, 085104 (2008).
- [33] A. V. Chubukov, D. V. Efremov, and I. Eremin, Phys. Rev. B **78**, 134512 (2008).
- [34] V. Cvetkovic, and Z. Tesanovic, Euro. Phys. Lett. **85**, 37002 (2009).
- [35] T. Yildirim, Phys. Rev. Lett. **101**, 057010 (2008).
- [36] Q. Si, and E. Abrahams, Phys. Rev. Lett. **101**, 076401 (2008).
- [37] K. Haule, and G. Kotliar, New J. Phys. **11**, 025021 (2009).
- [38] K. Kuroki, S. Onari, R. Arita, H. Usui, Y. Tanaka, H. Kontani, and H. Aoki, Phys. Rev. Lett. **101**, 087004 (2009).
- [39] N. Lanatá, H. U. R. Strand, G. Giovannetti, B. Hellsing, L De' Medici, and M. Capone, Phys. Rev. B **87** 045122 (2013).
- [40] T. Hanaguri, S. Niitaka, K. Kuroki, and H. Takagi, Science **328**, 474 (2010).
- [41] L De' Medici, G. Giovannetti, and M. Capone, Phys. Rev. Lett **112**, 177001 (2014).

- [42] J. Rinçon, A. Moreo, G. Alvarez, and E. Dagotto, *Phys. Rev. B* **90**, 241105 (2014).
- [43] J. K. Glasbrenner, I. I. Mazin, H. O. Jeschke, P. J. Hirschfeld, and R. Valenti, arXiv:1501.04946 (2015).
- [44] L. Craco, and M. S. Laad, arXiv:1001.3273 (2010).
- [45] M. Neupane, P. Richard, Z. -H. Pan, Y. -M. Xu, R. Jin, D. Mandrus, X. Dai, Z. Fang, Z. Wang, and H. Ding, *Phys. Rev. Lett.* **103**, 097001 (2009).
- [46] M. Yi, D. H. Lu, R. Yu, S. C. Riggs, J. -H. Chu, B. Lv, Z. K. Liu, M. Lu, Y. -T. Cui, M. Hashimoto, S. -K. Mo, Z. Hussain, C. W. Chu, I. R. Fisher, Q. Si, and Z.-X. Shen, *Phys. Rev. Lett.* **110** 067003 (2013).
- [47] W. Li, C. Zhang, S. Liu, X. Ding, X. Wu, X. Wang, H. H. Wen, and M. Xiao, *Phys. Rev. B* **89** 134515 (2014).
- [48] L De' Medici, S. R. Hassan, M. Capone, and X. Dai, *Phys. Rev. Lett.* **102**, 126401 (2009).
- [49] R. Yu, and Q. Si, *Phys. Rev. Lett.* **110**, 146402 (2013).
- [50] L. Craco, M. S. Laad, and S. Leoni, *Europhys. Lett.* **91** 27001 (2009).
- [51] M. Aichhorn, S. Biermann, T. Miyake, A. Georges, and M. Imada, *Phys. Rev. B* **82**, 064504 (2010).
- [52] Z. Wang, M. Schmidt, J. Fischer, V. Tsurkan, M. Greger, D. Vollhardt, A. Loidl, and J. Deisenhofer, *Nature Comm.* **5**, 3202 (2014).
- [53] B. Batlogg, H. Y. Hwang, H. Takagi, R. J. Cava, H. L. Kao, and J. Kwo, *Physica C* **130**, 235 (1994).
- [54] N. Plakida, *High-Temperature Cuprate Superconductors: Experiment, Theory, and Applications Springer Series in Solid-State Sciences*, Springer, 2010.
- [55] A. A. Kordyuk, arXiv:1501.0415 (2015).
- [56] Elbio Dagotto, *Nanoscale Phase Separation and Colossal Magnetoresistance*, Springer Science (2013)

- [57] M. Okawa, Y. Ishida, M. Takahashi, T. Shimada, F. Iga, T. Takabatake, T. Saitoh, and S. Shin, arXiv: 1407.0578 (2014).
- [58] B. Sac  p  , C. Chapelier, T. I. Baturina, V. M. Vinokur, M. R. Baklanov, and M. Sanquer, *Nat. Commun.* **1**, 140 (2010).
- [59] A. Mann, J. Walowski, M. M  nzenberg, S. Maat, M.J. Carey, J.R. Childress, C. Mewes, D. Ebke, V. Drewello, G. Reiss, and A. Thomas, *Phys. Rev. X* **2**, 041008 (2012).
- [60] P. Magierski, G. Wlaz  owski, and A. Bulgac, *Phys. Rev. Lett.* **107**, 145304 (2011).
- [61] T. Shimojima, T. Sonobe, W. Malaeb, K. Shinada, A. Chainani, S. Shin, T. Yoshida, S. Ideta, A. Fujimori, H. Kumigashira, K. Ono, Y. Nakashima, H. Anzai, M. Arita, A. Ino, H. Namatame, M. Taniguchi, M. Nakajima, S. Uchida, Y. Tomioka, T. Ito, K. Kihou, C. H. Lee, A. Iyo, H. Eisaki, K. Ohgushi, S. Kasahara, T. Terashima, H. Ikeda, T. Shibauchi, Y. Matsuda, and K. Ishizaka, *Phys. Rev. B* **89**, 045101 (2014).
- [62] T. Sato, S. Souma, K. Nakayama, K. Terashima, K. Sugawara, T. Takahashi, Y. Kamihara, M. Hirano, and H. Hosono, *J. Phys. Soc. Jpn.* **77**, 063708 (2008).
- [63] L. H. -Yun, J. X. -Wen, Z. W. -Tao, Z. Lin, M. J. -Qiao, L. G. -Dong, D. X. -Li, W. Gang, L. R. -Hua, C. X. -Hui, R. Z. -An, Y. Wei, C. G. -Can, C. G. -Fu, W. N. -Lin, W. G. -Ling, Z. Yong, Z. Yong, W. X. -Yang, Z. Z. -Xian, X. Z. -Yan, C. C. -Tian, and Z. X. -Jiang, *Chinese Phys. Lett.* **25**, 3761 (2008).
- [64] Y. Ishida, T. Shimojima, K. Ishizaka, T. Kiss, M. Okawa, T. Togashi, S. Watanabe, X. Wang, C. Chen, Y. Kamihara, M. Hirano, H. Hosono, and S. Shin, *J. Phys. Soc. Jpn.* **77**, 61 (2008).
- [65] L. Boeri, O. V. Dolgov, and A. A. Golubov, *Phys. Rev. Lett.* **101**, 026403 (2008).
- [66] I. I. Mazin, D. J. Singh, M. D. Johannes, and M. H. Du, *Phys. Rev. Lett.* **101**, 057003 (2008).
- [67] K. Kuroki, S. Onari, R. Arita, H. Usui, Y. Tanaka, H. Kontani, and H. Aoki, *Phys. Rev. Lett.* **101**, 087004 (2008).
- [68] K. Kuroki, H. Usui, S. Onari, R. Arita, and H. Aoki, *Phys. Rev. B* **79**, 224511 (2009).

- [69] K. Kuroki, S. Onari, R. Arita, H. Usui, Y. Tanaka, H. Kontani, and H. Aoki, *New J. Phys.* **11**, 025017 (2009).
- [70] C. Cao, P. J. Hirschfeld, and H. -P. Cheng, *Phys. Rev. B* **77**, 220506 (2008).
- [71] Y. Yanagi, Y. Yamakawa, and Y. Ono, *J. Phys. Soc. Jpn.* **77**, 123701 (2008).
- [72] K. Seo, B. A. Bernevig, and J. Hu, *Phys. Rev. Lett.* **101**, 206404 (2008).
- [73] V. Mishra, G. Boyd, S. Graser, T. Maier, P. J. Hirschfeld, and D. J. Scalapino, *Phys. Rev. B* **79** 094512 (2009).
- [74] H. Ding, P. Richard, K. Nakayama, T. Sugawara, T. Arakane, Y. Sekiba, A. Takayama, S. Souma, T. Sato, T. Takahashi, Z. Wang, X. Dai, Z. Fang, G. F. Chen, J. L. Luo, and N. L. Wang, *Euro Phys. Lett.* **83**, 47001 (2008).
- [75] K. Nakayama, T. Sato, P. Richard, Y. Xu, Y. Sekiba, S. Souma, G. Chen, J. Luo, N. Wang, H. ding, and T. Takahashi, *Euro Phys. Lett.* **85**, 67002 (2009).
- [76] J. Xing, S. Li, X. Ding, H. Yang, and H. H. Wen, *Phys. Rev. B* **86**, 214518 (2012).
- [77] Y. Mizuguchi, T. Hiroi, J. Kajitani, H. Takatsu, H. Kadowaki, and O. Miura, *J. Phys. Soc. Jpn.* **83**, 053704 (2014).
- [78] Y. Mizuguchi, *J. Phys. Chem. Solids* **84**, 34 (2015).
- [79] H. Lei, K. Wang, M. Abeykoon, E.S. Bozin, and C. Petrovic, *Inorg. Chem.* **32**, 10685 (2013).
- [80] F. Han, X. Zhu, G. Mu, P. Cheng, and H. H. Wen, *Phys. Rev. B* **78**, 180503 (2008).
- [81] Y. Mizuguchi, H. Fujihisa, Y. Gotoh, K. Suzuki, H. Usui, K. Kuroki, S. Demura, Y. Takano, H. Izawa, and O. Miura, *Phys. Rev. B* **86**, 220510 (2012).
- [82] H. Usui, K. Suzuki, and K. Kuroki, *Phys. Rev. B* **86**, 220501 (2012).
- [83] Y. Yang, W. -S. Wang, Y. -Y. Xiang, Z. -Z. Li, and Q. -H. Wang, *Phys. Rev. B* **88**, 094519 (2013).
- [84] X. G. Wan, H. C. Ding, S. Y. Savrasov, and C. G. Duan, *Phys. Rev. B* **87**, 115124 (2013).

- [85] T. Yildirim, Phys. Rev. B **87**, 020506 (2013).
- [86] G. Lamura, T. shiroka, P. Bonfa, S. Sanna, R. De Renzi, C. Baines, H. Luetkens, J. Kajitani, Y. Mizuguchi, O. Miura, K. Deguchi, S. Demura, Y. Takano, and M. Putti, Phys. Rev. B **88**, 180509 (2013).
- [87] Z. -R. Ye, H. -F. Yang, D. -W. Shen, J. Jiang, X. -H. Niu, D. -L. Feng, Y. -P. Du, X. -G. Wan, J. -Z. Liu, X. -Y. Zhu, H. -H. Wen, and M. -H. Jiang, Phys. Rev. B **90**, 045116 (2014).
- [88] L. -K. Zeng, X. -B. Wang, J. Ma, P. Richard, S. -M. Nie, H. -M. Weng, N. -L. Wang, Z. Wang, T. Qian, and H. Ding, Phys. Rev. B **90**, 054512 (2014).
- [89] S. Li, H. Yang, D. Fang, Z. Wang, J. Tao, X. Ding, and H. H. Wen, Sci. China Phys. Mech. Astron., **56**, 2019 (2013).
- [90] J. Z. Liu, D. L. Fang, Z. Y. Wang, J. Xing, Z. Y. Du, S. Li, X. Y. Zhu, H. Yang, and H.H. Wen, Europhys. Lett. **106**, 67002 (2014).
- [91] T. Zhou, and Z.D. Wang, J. Supercond. Nov. Magn. **26**, 2735 (2013).
- [92] Y. Liang, X. X. Wu, W. F. Tsai, and J. P. Hu, Front. Phys. **9**, 194 (2014).
- [93] G. B. Martins, A. Moreo, and E. Dagotto, Phys. Rev. B **87**, 081102 (2013).
- [94] Y. Yang, W. S. Wang, Y. Y. Xiang, Z. Z. Li, and Q. H. Wang, Phys. Rev. B **88**, 094519 (2013).
- [95] C. -L. Dai, Y. Yang, W. -S. Wang, and Q. -H. Wang, Phys. Rev. B **91**, 024512 (2015).
- [96] A. Qurashi, Metal Chalcogenide Nanostructures for Renewable Energy Applications, Wiley ISBN: 978-1-118-23791-5, (2015).
- [97] P. D. Antunez, J. J. Buckley, and R. L. Brutchey, Nanoscale **3**, 2399 (2011).
- [98] S. H. Wei, and A. Zunger, Phys. Rev. B **55**, 13605 (1997).
- [99] E. A. Albanesi, E. C. Okoye, C. O. Rodriguez, E. L. Peltzer y Blanca, and A. G. Petukhov Phys. Rev. B **61**, 16589 (2000).

[100] R. B. Shalvoy, G. B. Fisher, and P. J. Stiles, *Phys. Rev. B* **15**, 2021 (1977).

[101] M. Taniguchi, R. L. Johnson, J. Ghijsen, and M. Cardona, *Phys. Rev.* **42**, 3634 (1990).

[102] L. Makinistian, and E. A. Albanesi, *J. Phys.: Condens. Matter* **19**, 186211 (2007).

Chapter 2

Experimental Methodologies

In the present chapter we have discussed the various experimental techniques employed in the thesis. Photoemission spectroscopy is an efficient technique to investigate the electronic structure of solids. The electronic structures of layered materials, studied here, have been investigated utilising Ultraviolet Photoemission Spectroscopy (UPS), X-ray Photoemission Spectroscopy (XPS), Angle Resolved Photoemission Spectroscopy (ARPES) and Inverse Photoemission Spectroscopy (IPES). Low energy Electron Diffraction (LEED) has been used to confirm the crystallinity of single crystal surface. The experimental results have been well supported by the theoretical band structure calculations using Tight Binding Linear Muffin Tin Orbital (TB LMTO) method with ASA approximation. Section 2.1 and 2.2 focusses on Photoemission Spectroscopy (UPS and XPS) and Inverse Photoemission Spectroscopy (IPES) respectively. Section 2.3 describes the experimental procedures adopted in our photoemission experiments. Section 2.4 highlights the evolution and theoretical background of TB LMTO method.

2.1 Photoemission Spectroscopy:

Photoemission spectroscopy has been established as one of the most important tool for studying the electronic structure of molecules, solids and surfaces. The photoelectric effect was first experimentally observed by Heinrich Hertz and Wilhelm Hallwachs in 1887. They demonstrated that UV exposure of solid surfaces lead to ejection of negatively charged particles [1,2]. Subsequently, there were observation of photoelectric effect via emission of electrons from the cathode, by Thomson [3] in 1899 and by Lenard [4] in 1900. They also established the dependency of the electron current and its velocity on the intensity and frequency of the incident

light. But the phenomenon remained unresolved within the framework of classical theory of electromagnetic radiation until 1905 when Albert Einstein gave an explanation invoking the concept of quantum nature of light [5]. Since the discovery of photoelectric effect, continuous efforts were undertaken to establish photoemission as a technique to extract the information regarding the states of an electron inside a solid. The field of photoemission was pioneered in the early 1960s by several groups. The group of Spicer, measured the first UPS valence band spectrum on copper [6] and developed the three-step model [7]. The group of Turner, performed UPS on gases [8] using a novel type of VUV excitation source, namely the differentially pumped gas discharge lamp [9] that is still common in UPS setups today. The group of Siegbahn in Uppsala, developed a high-resolution XPS analyser that allowed the detailed study of core-level binding energies of solids [10]. In 1974 Smith, Traum and DiSalvo [11–14] first performed the angular dependent band mapping of the layered compounds TaS₂ and TaSe₂.

The early experimental set up suffered from poor energy and momentum resolutions, of around 100 meV and 2°, respectively. The achieved resolutions were inadequate for the study of various exotic physical phenomena like superconductivity, ferromagnetism etc. in a solid as the electrons occupying ~ 25 meV below Fermi energy (E_F) governs the entire physics which underlies these phenomena. Significant progress towards the advancement of photoelectron spectroscopy has led to the state of the art energy and momentum resolutions to reach the regime of sub-meV [15] and fraction of a degree respectively. The enormous evolution of PES is intertwined with the development of many other experimental techniques, such as the improvement of ultrahigh vacuum (UHV), the design of electron energy analyzers with high energy resolution, the development of synchrotron radiation, laser based light sources and very low temperature facilities.

2.1.1 Principle and Theory of photoemission

Photoemission is a photon in electron out process based on the principle of photoelectric effect. Photons with energy $h\nu$ impinging on a sample result in excitation of electrons to a higher state inside the solid. If the photoexcited electron has sufficient energy to overcome the surface barrier (work function) of the material, it emanates out and is detected by an energy analyzer. The schematic of a photoemission geometry is shown in figure 2.1. The kinetic energy of the emitted photoelectron is given by

$$E_{kin} = h\nu - |E_B| - \phi \quad (2.1)$$

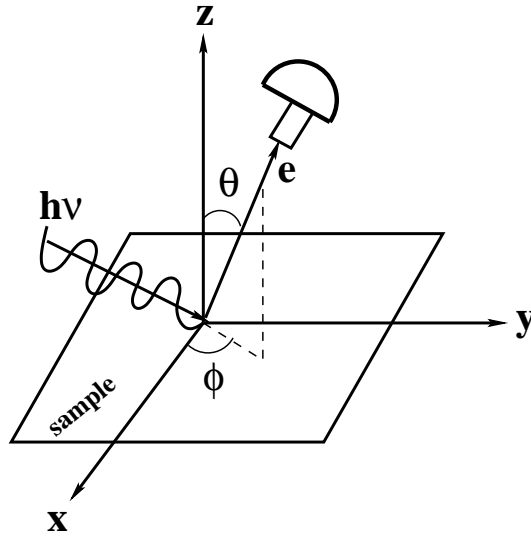


Figure 2.1: The schematic of a photoemission experiment. The photoemitted electron is specified by its kinetic energy (E_{kin}) and the emission angles θ and ϕ . The intensity of the outgoing electrons is measured by the analyzer as a function of (E_{kin}).

where, $h\nu$ is the photon energy, E_{kin} is the kinetic energy of the photoelectron, E_B is the binding energy of the electron inside the solid and ϕ is the work function (the energy required for an electron at E_F to just escape from the solid). The schematic energy level diagram of photoemission process is depicted in figure 2.2.

The energy of the incident photons classifies photoemission spectroscopy into X-ray Photoelectron Spectroscopy (XPS) and Ultraviolet Photoelectron Spectroscopy (UPS). The photon source used in case of XPS lies in the X-ray regime (100 - 1500 eV) and hence probes the core levels in solids determining the chemical compositions, elemental concentrations and oxidation states of the elements. The energy of the incident photon is in the UV regime (10 - 100 eV) in case of UPS and hence probes valence energy levels and chemical bonding. The lower photon energy in the case of UPS results in a higher probability of interaction with the valence electrons and hence is more sensitive to valence bands. The photocurrent is measured as a function of electron kinetic energy and the resulting spectrum is displayed in the form of energy distribution curve (EDC).

Depending on the geometries of photoemission, UPS is divided into two broad categories namely, angle integrated photoemission and angle resolved photoemission. In the case of angle integrated measurements, the solid angle of detection is large (under favourable conditions close to 2π) as a result, the momentum information is blurred by the integration over all the

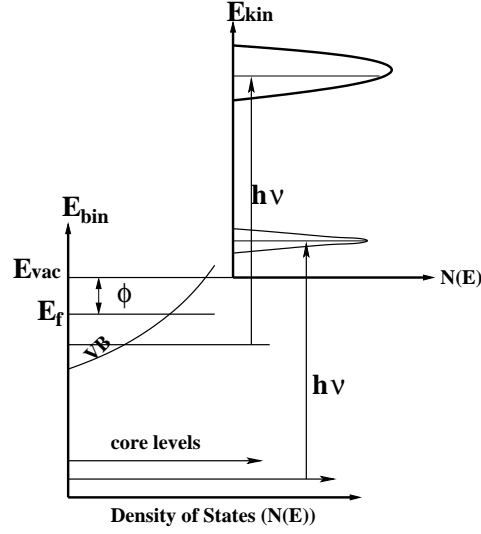


Figure 2.2: The schematic energy level diagram of photoemission process. E_F and E_{vac} are the Fermi energy and the vacuum level of the system. The intensity of the outgoing electrons is measured as a function of kinetic energy (E_{kin}).

outgoing wave vectors. Such measurements are usually performed on polycrystalline samples and yield joint density of states. In the case of angle resolved photoemission, performed on single crystals, the solid angle of detection is small ($< 2^\circ$) which allows exploitation of k-conservation by detection in a narrow k-interval. The take off angles of the photoelectrons are also taken care of either by an analyzer with pin hole entrance aperture and EDCs being recorded point by point by moving the analyzer or by a more advanced analyzer with channel plate.

Both energy (eqn. 2.1) and momentum (eqn. 2.2) are conserved in the photoemission process.

$$\mathbf{k}_i + \mathbf{k}_{h\nu} = \mathbf{k}_f \quad (2.2)$$

where, \mathbf{k}_i and \mathbf{k}_f are the reduced wave vectors of the electron in its initial and final states respectively inside the solid and $\mathbf{k}_{h\nu}$ is the wave vector of the incident photon. For low energy photon, used to study the valence band, the momentum of the incident photon can be neglected when compared with the crystal momentum of the electron in the first Brillouin zone. Hence, $\mathbf{k}_i = \mathbf{k}_f$. The final state Bloch function can be written as

$$\mathbf{k}_f = \mathbf{k} + \mathbf{G} \quad (2.3)$$

where, \mathbf{G} is the reciprocal lattice vector coming from the periodicity of lattice and \mathbf{k} is the final state crystal momentum in the reduced Brillouin zone. As the photoexcited electron is

free outside the solid, each $(\mathbf{k}+\mathbf{G})$ component can be matched to a travelling wave outside the crystal. Thus, the conservation of the wave vector is given by

$$\mathbf{k}_f = \mathbf{k} + \mathbf{G} = \mathbf{K}, \quad (2.4)$$

\mathbf{K} being the wavevector of the travelling free electron. Combining equations (2.2) and (2.4) we get

$$\mathbf{k}_i = \mathbf{K} \quad (2.5)$$

But due to the presence of the surface discontinuity in solid, the total momentum is no longer conserved, rather only the component parallel to the surface is conserved. Hence, the correct momentum conservation relation is given by,

$$\mathbf{k}_{i\parallel} = \mathbf{k}_{\parallel} + \mathbf{G}_{\parallel} = \mathbf{K}_{\parallel} \quad (2.6)$$

where, $\mathbf{k}_{i\parallel}$, \mathbf{k}_{\parallel} , \mathbf{G}_{\parallel} and \mathbf{K}_{\parallel} are the surface parallel components of the reduced initial state wave vector \mathbf{k}_i , the reduced final state wave vector \mathbf{k} , the reciprocal lattice vector \mathbf{G} and the external photoelectron wave vector \mathbf{K} respectively. Since the kinetic energy of the photoelectron is measured experimentally, its total momentum can be calculated from the following equation

$$\hbar^2 K^2 / 2m_e = E_{kin} \quad (2.7)$$

where, m_e is the mass of an electron. According to the geometry in fig. 2.1 and using equation (2.7) the parallel and perpendicular components of the momentum are obtained as

$$K_{\parallel} = \frac{\sqrt{2m_e E_{kin}}}{\hbar} \sin \theta \quad (2.8)$$

$$K_{\perp} = \frac{\sqrt{2m_e E_{kin}}}{\hbar} \cos \theta \quad (2.9)$$

The x and y components of \mathbf{K}_{\parallel} are related to the azimuthal angle ϕ in the following way

$$K_{\parallel x} = \frac{\sqrt{2m_e E_{kin}}}{\hbar} \sin \theta \cos \phi \quad (2.10)$$

$$K_{\parallel y} = \frac{\sqrt{2m_e E_{kin}}}{\hbar} \sin \theta \sin \phi \quad (2.11)$$

Once $K_{\parallel x}$ and $K_{\parallel y}$ become known, the parallel component of the crystal momentum ($\mathbf{k}_{i\parallel}$) of the electron in its initial state is also known through the relation in equation (2.6). The ARPES work presented in this thesis has dealt only with the parallel component of momentum.

In photoemission experiment the measured quantity is the photoelectron intensity as a function of the kinetic energy of the emitted electrons. The total intensity of the photoemitted electrons $I(E, k)$ (k dependence being taken care of only in ARPES) is the sum of the distribution of primary electrons $I_p(E, k)$ which have not suffered any inelastic collisions and a background of secondary electrons $I_s(E, k)$ which have suffered an energy loss in one or more collisions. Therefore,

$$I(E, k) = I_p(E, k) + I_s(E, k) \quad (2.12)$$

The background of secondary electrons can be subtracted from the energy distribution curve (EDC) of the photoemitted electrons. To have an idea of the factors contributing to the primary photoelectron intensity, the photoemission process is usually described in the framework of two theoretical models namely, the one-step model and the three-step model. In the one-step model, the photon absorption, electron emission and its detection is considered as a single coherent process. But, the model suffers from computational difficulties due to the inherent complexities arising from the involvement of surface vacuum interface and choices of wave functions. Hence, the photoemission process is most often interpreted in terms of the much simpler three-step model [7, 16–18]. In this approach, the photoemission process is subdivided into three sequential independent steps (Fig. 2.3) such as:

- (1) the optical excitation of an electron in the bulk,
- (2) the transport of the excited electron through the solid to the surface and
- (3) the escape of the electron from the solid surface into the vacuum.

The photoemission intensity ($I_p(E, k)$) is then given by the product of three independent quantities: the total probability for the optical transition ($P(E, k)$), the scattering probability of the electrons while travelling through the solid ($d(E, k)$) and the transmission probability ($T(E, k)$) through the surface potential barrier.

The transition probability w_{fi} due to an optical excitation from the N -electron initial state Ψ_i^N to one of the possible final states Ψ_f^N is approximated by the Fermi's Golden rule:

$$w_{fi} = \frac{2\pi}{\hbar} |\langle \Psi_f^N | H_{int} | \Psi_i^N \rangle|^2 \delta(E_f^N - E_i^N - h\nu), \quad (2.13)$$

where, $E_i^N = E_i^{N-1} - E_B^k$ and $E_f^N = E_f^{N-1} + E_{kin}$ are the energies of the initial and final N -electron states, respectively, E_B^k is the binding energy of the photoelectron with momentum k and kinetic energy E_{kin} . The initial state can be written as a product of ϕ_i^k , the state from which the electron with momentum k is photoexcited, and the wave function of the remaining

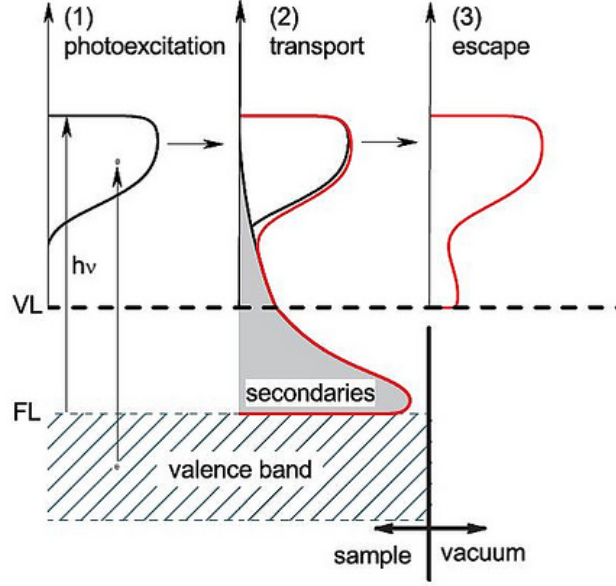


Figure 2.3: Illustration of the three-step model of photoemission. It consists of (1) the photoexcitation of an electron in the bulk, (2) its travel through the solid to the surface and (3) its transmission through the surface into the vacuum.

electrons Ψ_i^{N-1} , i.e.,

$$\Psi_i^N = C\phi_i^k\Psi_i^{N-1}, \quad (2.14)$$

where, C is the operator that antisymmetrizes the wave function properly. In a similar way the final state can also be expressed as

$$\Psi_f^N = C\phi_f^{E_{kin}}\Psi_f^{N-1}, \quad (2.15)$$

where, $\phi_f^{E_{kin}}$ is the wave function of the photoemitted electron and Ψ_f^{N-1} is the same for the remaining $(N - 1)$ electrons. The transition matrix element then reduces to

$$w_{fi} = \frac{2\pi}{\hbar} |\langle \phi_f^{E_{kin}} | H_{int} | \phi_i^k \rangle|^2 |\langle \Psi_f^{N-1} | \Psi_i^{N-1} \rangle|^2 \delta(E_f^N - E_i^N - h\nu) \quad (2.16)$$

or

$$w_{fi} = |M_{fi}^k|^2 |c_{fi}|^2 \delta(E_f^N - E_i^N - h\nu) \quad (2.17)$$

where, $|M_{fi}^k|^2$ is the one-electron matrix element and $|c_{fi}|^2$ is $(N - 1)$ electron overlap integral. Basically, this is the probability that the removal of an electron from the i^{th} state of a N -electron system leaves the system in any of its excited state f of the $(N - 1)$ electron system. In a real solid, many of the c_{fi} which contributes to the photoemission intensity as additional peaks

(called satellites) along with the main peak, are non zero. The intensity is then proportional to the transition matrix element, i.e.,

$$I_p(E, k) \propto \sum_{f,i} |M_{fi}^k|^2 |c_{fi}|^2 \delta(E_f^N - E_i^N - h\nu) \quad (2.18)$$

The above formalism is valid for atoms and molecules but is not applicable to solids where correlation exists. In the case of strongly correlated systems, the interacting electrons are conveniently described using Green's function formalism where the Green's function is related to another quantity called spectral function $A(k, E)$ in the following manner:

$$A(k, E) = \pi^{-1} \text{Im}\{G(k, E)\} \quad (2.19)$$

It is also found that $A(k, E)$ has a form which is very similar to the photoemission intensity described above and in fact $I_p(E, k)$ can be expressed as

$$I_p(E, k) \propto \sum_{f,i} |M_{fi}^k|^2 A(k, E) \quad (2.20)$$

$A(k, E)$ describes the probability of removing (for E below E_F) or adding (to E above E_F) an electron with energy E and wave vector \mathbf{k} from (to) the interacting system. For a non-interacting system with one-electron energy E_k^0 , the Green's function is given by

$$G_0(\mathbf{k}, E) = \frac{1}{E - E_k^0 - i\epsilon} \quad (2.21)$$

where, ϵ is a very small quantity and

$$A_0(\mathbf{k}, E) = \delta(E - E_k^0) \quad (2.22)$$

which means that the spectral function for a non-interacting system is a δ -function centered at $E = E_k^0$. In an interacting electron system the electron energy gets renormalized by the self-energy, given by,

$$\Sigma(\mathbf{k}, E) = \text{Re}\{\Sigma(\mathbf{k}, E)\} + i\text{Im}\{\Sigma(\mathbf{k}, E)\} \quad (2.23)$$

The Green's function changes to

$$G(\mathbf{k}, E) = \frac{1}{E - E_k^0 - \Sigma(\mathbf{k}, E)} \quad (2.24)$$

and correspondingly the spectral function gets modified as

$$A(\mathbf{k}, E) = \pi^{-1} \frac{\text{Im}\{\Sigma(\mathbf{k}, E)\}}{[E - E_k^0 - \text{Re}\{\Sigma(\mathbf{k}, E)\}]^2 + [\text{Im}\{\Sigma(\mathbf{k}, E)\}]^2} \quad (2.25)$$

The real part of the self-energy corresponds to the shift in the energy of the particle (called quasiparticle for interacting system) from its one-electron value, while the imaginary part is related to the life-time of the quasiparticle.

2.1.2 Instrumentation

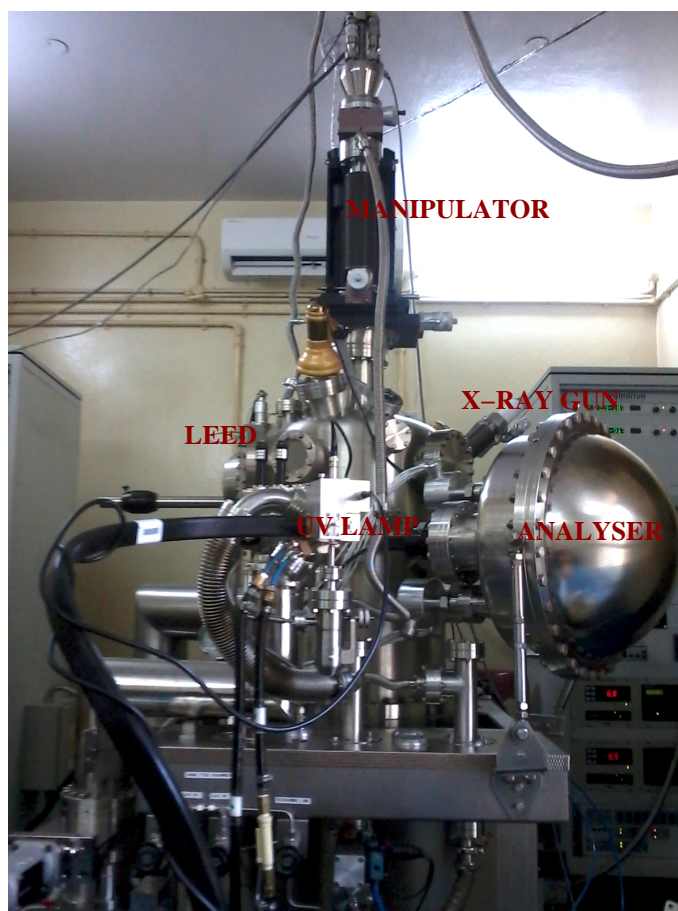


Figure 2.4: Photoemission system used in lab.

The photoemission spectrometric system in our laboratory shown in fig. 2.4 consists of two OMICRON ultra-high vacuum (UHV) chambers, the main chamber / analysis chamber and a sample preparation chamber. The analysis chamber is made up of mu metal which protects the photoemitted electrons from earth's magnetic field and any stray magnetic field. For quick sample loading without breaking the UHV conditions in preparation and analysis chambers, a small load lock chamber is attached with the preparation chamber. Further, the sample preparation chamber is equipped with a four-axes manipulator, a diamond file, a sample heater and an Ar ion sputter gun. Samples from the preparation chamber are transferred by using a magnetically coupled transfer rod. The analysis chamber is equipped with the sources of energetic photons (X-ray and VUV-light), the hemispherical electron energy analysers (SCIENTA R3000 and OMICRON AR 65), four-axes cryo-manipulator and low energy electron diffraction (LEED). The working principle of a few of the important components are discussed below.

1. Photon Source

UV photons are generated via SCIENTA VUV 5k lamp and X-ray dual anode source serves the purpose of generating X rays.

UV Lamp

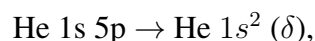
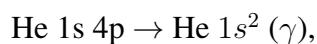
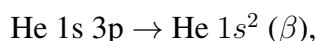
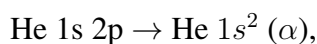
The SCIENTA VUV 5k is a high intensity monochromatised VUV (vacuum ultra violet) radiation source. The VUV radiation originates from radiative transitions in the Helium plasma excited by electron impact using the Electron Cyclotron Resonance (ECR) technique. Discharge occurs in the discharge cavity inside the lamp head VUV 5050, in a magnetic field tuned to the microwave frequency, generated from a microwave generator VUV 5011, to meet the ECR condition.

The microwave (RF) generator consists of a 10 mW dielectric resonator oscillator (DRO) and a four cavity klystron amplifier (Varian VKX 7913) together with necessary power supplies and control electronics. Klystron amplifies the radio frequency signal by converting the kinetic energy in a DC electron beam into radio frequency power. The RF power is then transported via a ferrite circulator to the output waveguide. About 25% of the input DC power is converted to RF radiation, the rest is dissipated as heat. When the high voltage is switched on, the RF energy goes to the cavity and is reflected back to the circulator, which redistributes it into a high power dummy load. A small part of this reflected power is detected and subsequently compared to a reference voltage. If the level is above 20%, 12 V DC is fed out to the spark generator at the lamp head. This generates 25 kV pulses that discharge inside one of the hollow magnet pole pieces to ignite the plasma. As soon as the discharge starts, the reflection disappears and the high voltage pulses cease.

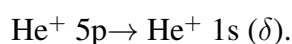
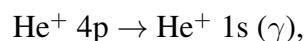
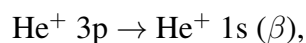
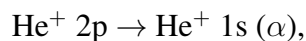
The oscillating RF electric field then reaches the transformer located inside the lamp head via waveguide. The transformer is an impedance matching structure between the rectangular waveguide and a pair transmission line composed of Tantalum, which allows compression of the incident field in the direction perpendicular to the electric field vector to 5 mm. This results in a considerably increased power density. The electric field then reaches the plasma cavity where it causes Helium discharge by ECR phenomena in the presence of an inhomogenous magnetic field created by the magnets coupled externally to the plasma tube. An oscillating electric field with its electric field vector perpendicular to the magnetic field vector results in acceleration of the particles, like in a cyclotron. In comparison to the standard method of creating a discharge by application of Dc voltage between two electrodes, ECR has added

advantages. Firstly, the plasma is achieved in a small volume due to efficient acceleration. Secondly, ECR plasma requires much lower gas pressure.

The VUV source can be operated with various discharge gases like helium, neon, argon, krypton, xenon or hydrogen. We have used Helium gas to study the valence band and the near Fermi level (E_F) features. Helium discharge causes the atoms to go into an excited state and subsequently the excited states decay very fast by emitting photons with an energy equal to the energy difference between the excited states and the ground states. In the case of helium, two groups of radiation are present: the first one originates from the decay of excited neutral helium atoms i.e.,



The second one originates from the decay of singly ionized helium atoms, i.e.,



The α lines are the strongest ones and occur at 21.22 eV and 40.81 eV for He I and He II respectively.

The He I and He II lines are separated by means of VUV5040 monochromator. It consists of a toroidal grating that selects and refocuses the chosen wavelength generated from the UV source via the adjustment of outer and central knobs. The VUV flux density is $\sim 1.5 \times 10^{16}$ photons/sr second with a beam diameter of 2 mm. Two stages of differential pumping are employed to maintain the chamber in UHV while providing a stable pressure in the lamp. At the first stage, the discharge region is pumped down to a pressure of $\sim 10^{-2}$ mbar using a rotary pump, whereas for the second stage, a turbomolecular pump is employed to further reduce the He gas pressure before the main vacuum chamber.

X-ray source

The DAR 400 X-ray source from OMICRON is employed for XPS measurements. It is a twin

anode (Mg $K\alpha$ (1253.6 eV) and Al $K\alpha$ (1486.6 eV)) X-ray source. Electrons are extracted from a hot filament and focused to bombard the selected surface of an anode at high positive potential. The excited core level electrons emit characteristic X-rays when they de-excite to a lower energy level. The anode is water cooled to prevent the aluminium or magnesium surfaces from evaporating. X-rays generated at the surface of the anode pass through a thin aluminium window to the sample under study. The aluminium window acts as a partial vacuum barrier between the source and the sample region.

2. Hemispherical Analyser

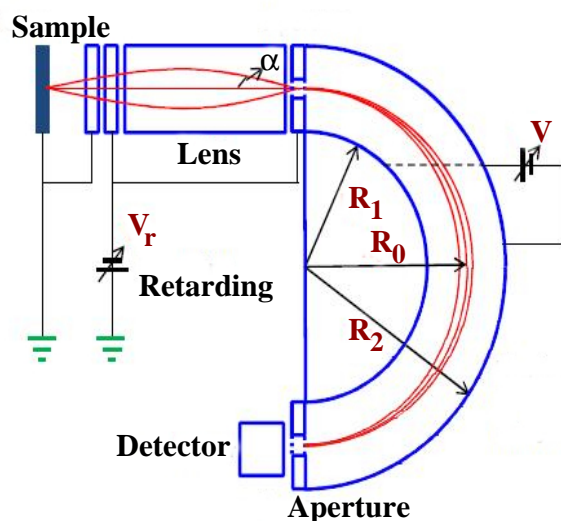


Figure 2.5: A schematic diagram of hemispherical analyser [19].

Measuring the kinetic energy of photoelectron is the most important requirement of photoemission process. The photoelectrons drifting in vacuum are pulled towards and focused into the energy analyser by the electric field generated by the electron lens. There exists several types of analyser, but the concentric hemispherical analyser (CHA) is the most widely used. A hemispherical deflection analyser consists of two concentric hemispheres, schematically shown in Fig. 2.5. The entrance and exit slits are centered on the mean radius of the inner and outer spheres. A potential difference is applied between the two hemispheres, with the outer one being negative with respect to the inner one. The electrostatic lens directs the photoelectrons into the space between the two hemispheres. Subsequently, all the photoelectrons experience a centripetal force and hence undergo uniform circular motion. Thus, the radius of curvature of this motion for a given potential difference between the two hemispheres is determined by

the electron's kinetic energy. The kinetic energy of the electron travelling on the central path ($R_0=(R_1+R_2)/2$), also known as the pass energy, is given by

$$E_P = \frac{eV}{R_2/R_1 - R_1/R_2} \quad (2.26)$$

The pass energy depends on the radii of the hemispheres and the voltage applied between them. Photoelectrons with kinetic energy greater than the pass energy will follow a path of larger radius of curvature and will therefore collide with the outer hemisphere. The photoelectrons with kinetic energy less than the pass energy will follow a path of smaller radius of curvature and will coincidentally collide with the inner hemisphere. The energy resolution of the CHA is calculated as [20]

$$\Delta E = E_P \left(\frac{x_1 + x_2}{2R_0} + \alpha^2 \right) \quad (2.27)$$

with x_1 and x_2 being the width of entrance and exit apertures respectively and α the angular acceptance of electron beam at the entrance slit. From the above expression, it is evident that the radii of the hemisphere and the slit width are relevant in determining the resolution of an energy analyzer. Hence, a large hemisphere is inherently favored because of a better resolution. In reality, the pass energy and the aperture sizes are set to achieve a good compromise between signal intensity and energy resolution.

For this thesis, the UPS data were collected by a hemispherical analyser SCIENTA R3000 with a mean radius of 135 mm. The ARPES and XPS measurements were done using R4000-WAL (with wide angle lens for high resolution) with a mean radius of 200 mm. The ejected photoelectrons are sorted according to their ejection angles via the electron lens and reach the hemispherical analyser which sorts the electrons according to their kinetic energy. Finally, the photoelectrons reach the Multi-channel Plate (MCP)-CCD detector assembly for particle detection which sorts the particles as a 2D image. The coverage of angular range is $\pm 10^\circ$ and $\pm 15^\circ$ for R3000 and R 4000-WAL respectively. The entrance slit width of the hemispherical analyser can be fixed at any of the six slit apertures, 0.2 (straight), 0.2 (curved), 0.4 (curved), 0.8 (curved), 1.3 (straight), 3.0 (straight).

Electron Lens

The SCIENTA R3000/EW4000 uses an multi-element electrostatic lens to collect and transfer the ejected photoelectrons from sample to the entrance slit of the hemispherical analyser. Inside the electrostatic lens, metal plates are held at constant potential. The electron lens serve various functions. Firstly, it acts as focussing lens, ensuing selection of different analysis areas and to

operate the lens in different modes (transmission and angular multiplexing modes). Secondly, it matches the initial kinetic energy of the electrons to the fixed pass energy of the analyser. The lens is equipped with a set of intensity deflector plates UP and LEFT. These plates ensure the electrostatic lens to look a few mm in the x or y direction on the sample without any geometrical change of the analyser, excitation source or manipulator. These can also be used for correction of misalignment of the excitation spot and the electron optic axis. The lens can be operated in transmission and angular multiplexing imaging modes. Switching between the two modes is done through the SCIENTA software. Transmission mode is the standard mode of lens operation. It produces an image of the sample on the detector and is intended for large spot analysis of polycrystalline samples. Transmission mode maximizes the total transmission through the lens at a constant magnification of about $5\times$. The spatial resolution in this mode is of the order of $300\ \mu\text{m}$. Angular multiplexing mode is a special way of lens operation, in which the emission angle distribution is imaged. Angular mode is used for Angle Resolved Photoemission Spectroscopy (ARPES).

Multi Channel Detector

The modern scienta analyser is equipped with a 2D multichannel detector attached to the end of hemispherical analyser. It offers the advantage of improved data acquisition efficiency, energy resolution and momentum resolution. The detector is a MCP/CCD camera unit which serves a 2-D detection system with energy in one direction and spatial/angular information in the other direction. The detector unit comprises of three sub units: the field termination mesh, the detector assembly (multichannel plates and phosphorus screen) and the CCD camera. The field termination mesh, placed immediately in front of the detector ensures a homogenous termination of the analyser field. It renders the possibility of a negative bias voltage on the detector to reduce the low energy secondary electrons. The detector assembly consists of two Multi-Channel Plates (MCP) and a phosphorous screen. The MCPs multiply each incoming electron about a million times. This electron pulse is accelerated to the phosphorous screen producing a light flash detectable by the Firewire CCD camera. The detector area registered by the CCD is a square of over 600 simultaneous energy channels and over 400 spatial/angular channels. The energy range is governed by the pass energy while the spatial/angular dispersion is controlled by the lens mode.

3. Low Energy Electron diffraction (LEED)

The orientation of single crystal surface is determined using LEED. A beam of low energy (20-

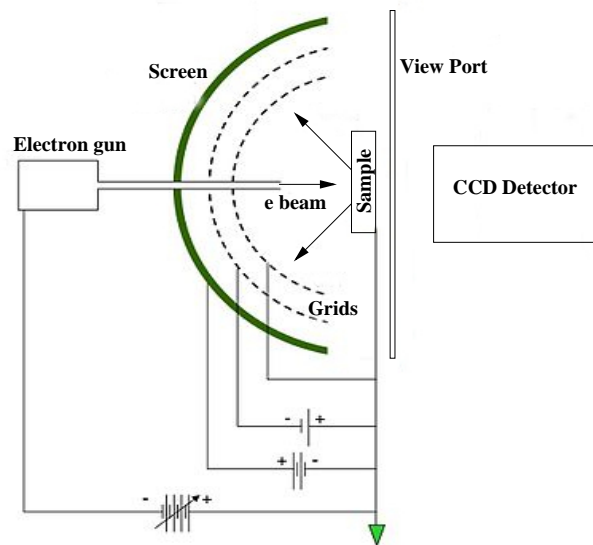


Figure 2.6: A typical set-up of LEED.

200 eV) electrons incident normally on the sample is diffracted by the periodically arranged atoms in crystals by Braggs law of diffraction, and gives rise to diffraction spots on the screen of the LEED system. Since the de Broglie wavelength associated with low energy electron is comparable to the lattice constant of a crystal, its diffraction can give information regarding the geometrical structure of the crystal. Single crystals with a well-ordered surface structure generates a back-scattered electron diffraction pattern while polycrystals give rise to a diffused circular pattern. The elastically-scattered electrons contribute to the diffraction pattern while the lower energy (secondary) electrons are removed by energy-filtering grids placed in front of the fluorescent screen (employed to display the pattern).

A typical experimental set-up is shown in figure 2.6. The basic elements in a LEED unit are an electron gun and a display system. Electron gun contains a cathode filament (thoriated tungsten) which is negatively biased with respect to the sample. Electrons emitted from the cathode via thermionic emission are accelerated and focussed into a beam by series of electron lenses. The electrons incident normally on the surface are backscattered elastically and diffraction pattern is seen on the screen. LEED detection system usually consists of three or four hemispherical concentric grids and a phosphor screen. The grids serve the purpose of screening out the inelastically scattered electrons. The first grid is grounded to shield the sample from the high electric fields from the luminescent screen. The second grid, the suppressor, is set to a voltage just below the acceleration voltage of the incident electrons to remove inelastically

scattered electrons from the diffracted beam. The last grid is grounded to shield the suppressor from the high voltage on the luminescent screen. After passage through the last grid the elastically scattered electrons are accelerated towards the screen by the screen voltage.

2.2 Inverse Photoemission Spectroscopy

Inverse photoemission is basically an electron in photon out process which relies on the concept of detecting the Bremsstrahlung radiation emitted due to the radiative transitions of electrons. Inverse photoemission spectroscopy (IPES) has emerged as a powerful technique to study the unoccupied electronic states of solid [21–23]. It can access the otherwise hardly accessible region between the Fermi and the vacuum level of the sample. Photoelectron spectroscopy and inverse photoemission spectroscopy are complementary to each other.

2.2.1 Principle and Theory of Inverse Photoemission

A monoenergetic beam of incoming electron initially couples to an unoccupied quantum state of energy (E_i , initial state energy) that is located above the vacuum level. Then, the electron undergoes a radiative transition to another unoccupied state (E_f , the final state energy). The transition is possible only to states that are located above the Fermi level.

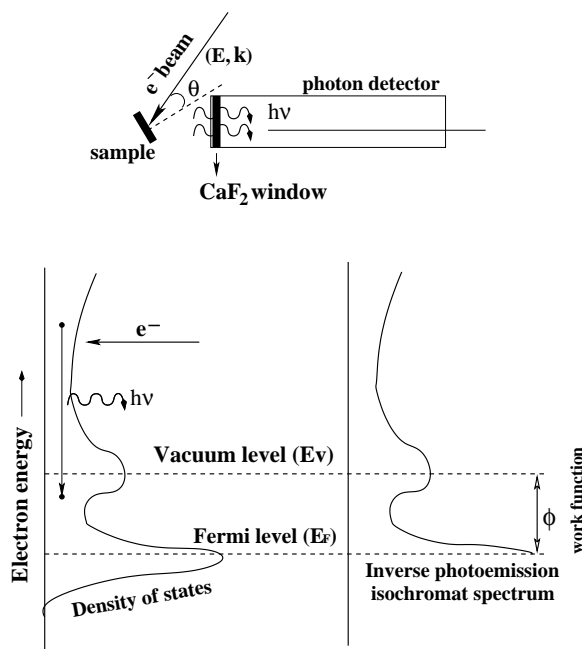


Figure 2.7: The schematic of Inverse Photoemission Process.

The schematic of inverse photoemission process is represented in fig 2.7. The energy conservation relation is given by

$$h\nu = E_f - E_i \quad (2.28)$$

The number of photons emitted with an energy $h\nu$ depends on the number of unoccupied states available at that energy. Thus, measurement of intensity distribution of the emitted photons is a measurement of the density of unoccupied states above Fermi level. The yield in IPES is very low compared to that of PES as can be seen from the ratio (R) of their differential cross-section:

$$R = \frac{(d\sigma/d\omega)_{IPES}}{(d\sigma/d\omega)_{PES}} = \left(\frac{\lambda_e}{\lambda_{h\nu}}\right)^2 \quad (2.29)$$

where, λ_e and $\lambda_{h\nu}$ are the wavelengths of emitted electron and photon in PES and IPES respectively. This ratio is a reflection of the different densities of final states available for the two transitions. The value of R is of the order of 10^{-5} and 10^{-3} in the UV and X-ray energy regime respectively. The low cross section for emission of photons in IPES is the major reason for a relatively slow development of the technique as compared with PES. In comparison to other techniques such as appearance potential spectroscopy (APS), X-ray absorption spectroscopy (XAS) which can probe unoccupied electronic states, IPES has the special advantage of resolving the momentum dependence of the empty bands. So, apart from the density of states in its angle-integrated mode it is possible to obtain the k -dependent band structure from k -resolved inverse photoemission spectroscopy (KRIPES).

There are two modes of operation of IPES experiment namely isochromat mode and tunable mode. In case of isochromat mode the intensity at constant photon energy $h\nu$ is detected by scanning the incident electron energy. In the tunable mode, the incident electron energy is fixed and one detects the intensity of the emitted photons as a function of photon energies. The information extracted is independent of the measurement mode used. In this thesis, we have used the isochromat mode and thus this method will be discussed henceforth. The random distribution of grains in case of polycrystalline sample results in an momentum integrated IPES spectra reflecting the joint density of unoccupied states. For single crystals, it is possible to measure the momentum resolved unoccupied band dispersion ($E(k)$).

As inverse photoemission can be regarded as a time inversion of the photoemission process, the time inversion of this model appropriate to bremsstrahlung emission leads to the three step [24] model analogous to photoemission process.

(1) Penetration of electrons into the solid: the incoming electron couples into one of the ini-

tially unoccupied electron states.

(2) Competition between non-radiative and radiative decay: there is a strong probability, $\beta(E)$, that the electron will decay non-radiatively through inelastic electron-electron scattering. This is the physical origin of the very short values ($\lambda \leq 0-20\text{\AA}$) for penetration depths of low energy electrons. The remaining fraction, $1-\beta(E)$, decay radiatively giving rise to the measured photons.

(3) Optical deexcitation: The radiative decay takes place by means of a direct (i.e. k conserving) transition, since the photon momentum is negligibly small.

The relative magnitudes of the photoemission photocurrent and the inverse photoemission photon yield mainly depends on the corresponding cross-sections (the transition probability per unit time). The interaction Hamiltonian in this case also is same as in direct photoemission because both the processes involve interaction of electron with photon.

2.2.2 Instrumentation

The basic experimental requirement of IPES is an electron source providing a well-defined beam and a photon detector with limited bandwidth. The photon detectors used in IPES have fallen into two categories, those which operate in an isochromat or fixed photon energy mode and those that are tunable, allowing detection at different photon energies. The IPES results, presented in this thesis, were obtained using a band-pass Geiger-Müller type photon detector with acetone gas filling and CaF_2 window (acetone/ CaF_2) in isochromat mode with a mean photon energy of 9.9 eV [25]. A Geiger-Müller counter, as schematically shown in the upper panel of figure 2.7, consists of a tube closed at one end by a calcium fluoride (CaF_2) window and filled with a gas to a certain pressure. The combination of the transmission properties of the window and the photoionization cross section of the gas determines the photon energy detected and the bandwidth. A photon with an energy lower than the cut-off of the window but higher than the ionization potential of the gas will initiate an electron cascade which is collected by a central electrode. For example, the high energy cut-off of the acetone/ CaF_2 detector is due to the CaF_2 window that does not transmit photons with energy > 10.2 eV, while the threshold for the photoionization of acetone at 9.7 eV sets the low energy cut-off. This determines the band-pass function and results in a mean photon detection energy of 9.9 eV with a FWHM of 0.4 eV. Thus, 9.9 ± 0.2 eV photons can enter the detector to photoionize acetone.

The typical requirements of electron sources for IPES are large current at low energies

with a narrow angular spread in the beam. However, the ability to achieve the requirements of high currents and low energies is restricted by fundamental limits imposed by space-charge effects: the space-charge-limited current density at a cathode varies as the three-halves power of the extraction voltage and inversely as the square of the cathode-anode distance. A Stoffel-Johnson type [26] electron source was used in our experiment. This is chosen because it has less space-charge effect and high beam current. The contact potential difference applied between the cathode and the lens electrodes ensues an uniform well focused electron beam with the set kinetic energy. The compensation of the contact potential difference also enhances the beam current substantially at low energies (<10 eV) and uniform beam current is achieved for the whole energy range [27].

2.3 Experimental Procedures

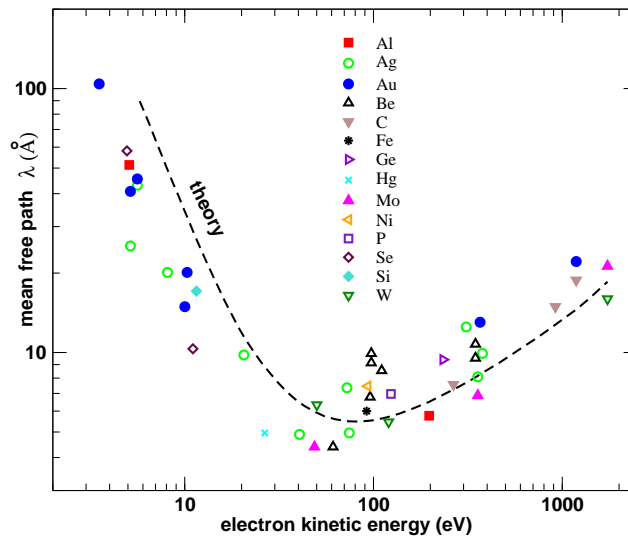


Figure 2.8: The universal curve of the electron mean free path versus kinetic energy.

It has already been discussed that the PES is a highly surface sensitive technique [28]. The 'universal curve' shown in fig. 2.8 gives an idea of the inelastic mean free path of the photoexcited electrons versus its kinetic energy. As seen from fig 2.8, the mean free path lies around or below 10 \AA in the kinetic energy range of 20-200 eV. Hence, vacuum better than 10^{-10} mbar is mandatory for maintaining a clean surface devoid of any contaminants. The photoemission spectra obtained from a contaminated surface shall not represent the bulk electronic structure. This makes the preparation and preservation of a clean sample surface

essential to PES measurement. The UHV is generated using a series of pumps namely rotary, turbo molecular, ion and sputter ion pumps. Among the various surface preparation techniques in situ scraping and in situ cleaving are the most widely used.

The sample was mounted on a stainless steel sample holder using commercial UHV compatible glue. Grounding of the sample was ensured using silver paste around the sample. The sample was first loaded under atmosphere into the load lock, which was pumped down to 1×10^{-7} mbar within one hour, then transferred into the preparation chamber with base vacuum $\sim 7 \times 10^{-10}$ mbar. Inside the preparation chamber, a clean surface is achieved. In case of polycrystalline samples, we have repeatedly scraped the surface using a diamond file until the feature at ~ 9.5 eV binding energy disappears. This feature has earlier been shown to originate from surface contamination, particularly adsorbed oxygen [29]. In case of single crystals, insitu cleaving using post technique has been used. In this technique, a small post (a small sized pin) is fixed on the sample surface with the help of UHV compatible glue, which is then struck off the sample insitu, to obtain a clean surface. The samples were then transferred immediately to the analysis chamber which is at a base vacuum of 3×10^{-10} . The crystallinity of the single crystals were ensured by taking the LEED patterns inside the analysis chamber. The exposure of UV light on the sample surface was accessible by moving the sample manipulator along x,y,z direction. The sample positioning was ensured according to the maximum electron counts obtained in the CCD detector. The energy of photon source can be tuned from He I (21.2 eV) to He II (40.8 eV) using the monochromator. To check the reproducibility of the results, all measurements reported here have been repeated many times. The spectra were collected at constant pass energy (CAE) mode using pass energy of 5 eV in transmission mode. The energy step size for full scan and high resolution scan were taken as 10 and 5 meV respectively. The slit size of the analyser was fixed at 1.3 mm and 3.0 mm for He I and He II lines respectively. For the ARPES experiments, the spectra were recorded at a pass energy of 10 meV, with energy step size of 40 meV in the angular mode. The slit size was fixed at 0.2 (curved). The XPS spectra were recorded at 200 eV pass energy in the transmission mode. The Carbon 1s line at 284.6 eV has been utilised for charge correction. A shirley type background has been removed from all the XPS spectra presented in the thesis. For the temperature dependent measurements, the samples were cooled by pumping liquid nitrogen through the sample manipulator fitted with a cryostat. Sample temperatures were measured using a silicon diode sensor touching the bottom of the stainless steel sample plate. The low temperature photoemission measurements

at 77 K were performed immediately after cleaning the sample surfaces followed by the room temperature measurements. The system was calibrated using the Fermi edge of a sputtered polycrystalline silver sample. The sputtering was done in the preparation chamber with 2 keV Ar ions at an Argon pressure of 4.5×10^{-5} mbar.

2.4 Band Structure Theory

Though the advent of quantum mechanics in early 1990s created the backbone for calculations of electronic structure and properties of atoms and solids, the calculations for complicated systems remained impossible until the progress of advanced mathematical and computational methods. As aptly stated by Paul Dirac in 1929 "The fundamental laws necessary for the mathematical treatment of large parts of physics and the whole of chemistry are thus fully known, and the difficulty lies only in the fact that application of these laws lead to equations that are too complex to be solved." The development of efficient computational facility as well as the methods of solving the rigorous quantum mechanical equations created a significant landmark in the field of quantum chemistry and condensed matter physics. Density Functional Theory (DFT) has emerged as one of the widely used methods today. Its importance was highlighted by the 1998 Nobel prize in chemistry which was awarded to Walter Kohn for his development of the density functional theory and to John Pople for his development of computational methods in quantum chemistry.

2.4.1 The Many-Particle Problem

The basic problem in condensed matter physics is dealing with the interactions of large number of particles. DFT attempts to solve this mathematically using computational tools. If the system is an atom or a small molecule, the number of particles is rather small, but when dealing with larger systems, describing the wave function of the system explicitly becomes infeasible. The full Hamiltonian for a many body problem in the non relativistic case consists of two species, electrons and nuclei, with Coulomb interaction both between themselves and with each other. To make situation simple, the Born-Oppenheimer approximation [30] is considered which assumes that the nuclei of the atoms, molecules or solids remain fixed and generate a static external potential in which the electrons move. For a system containing N electrons, Schrodinger's equation can be written as

$$\left[-\frac{\hbar^2}{2m} \sum_{i=1}^N \nabla_i^2 + \sum_{i=1}^N V_{ext}(\mathbf{r}_i) + \frac{1}{2} \sum_{j \neq i=1}^N \frac{e^2}{|\mathbf{r}_i - \mathbf{r}_j|} \right] \psi(x_1, x_2, \dots, x_N) = E\psi(x_1, x_2, \dots, x_N), \quad (2.30)$$

where, $x_i = \mathbf{r}_i, \sigma_i$

\mathbf{r} and σ are the electron space and spin coordinates respectively.

The first term represents the kinetic energy T , the second term denotes the external potential V_{ext} and the third term describes the electron-electron interaction U .

V_{ext} is the electrostatic potential generated by the nuclei and can be written as:

$$\sum_{i=1}^N V_{ext}(\mathbf{r}_i) = \sum_{i,k} \frac{Z_k e^2}{|\mathbf{r}_i - \mathbf{R}_k|} \quad (2.31)$$

where, Z_k is the atomic number of nucleus k at \mathbf{R}_k .

The quantum mechanical approach to solve equation 2.30 involves specification of external potential, calculation of wave function and observables by taking the expectation value of operators with this wave function. The early attempts to solve the many body problem started with the free electron model (FEM) which works well for the case of metals. Then came the Hartree and Hartree-Fock approaches and finally the Thomas-Fermi model, which might be thought of as a very early form of DFT since it uses the electron charge density as the basic variable instead of the wave function.

2.4.2 Density Functional Theory

The density functional theory is based on the two theorems proposed by Hohenberg and Kohn [31] in 1964. The first theorem demonstrates that the ground state properties of a many electron system are uniquely determined by an electron density that depends on three spatial coordinates, through the use of the functionals of electron density. The second theorem defines an energy functional and proves that the correct ground state electron density minimizes this energy functional. The HK-DFT lacked in accuracy due to the absence of exchange and correlation terms. In 1965, Kohn and Sham [32] formulated the DFT theory including the exchange and correlation terms. In the KS-DFT approximation, the many-body problem of interacting electrons in a static external potential is reduced to a system of non-interacting electrons moving in an effective potential. The effective potential includes the external potential and the effects of

the Coulomb interactions between the electrons, like the exchange and correlation interactions. Modeling the latter two interactions were difficult within the framework of KS DFT.

The most widely accepted approximation is the Local Density Approximation (LDA) to incorporate the exchange and correlation interactions. Local-density approximations (LDA) are a class of approximations to the exchange-correlation (XC) energy functional in density functional theory (DFT) that depend solely on the value of the electronic density at each point in space (and not, for example, derivatives of the density or the Kohn-Sham orbitals). Many approaches can yield local approximations to the XC energy. However, the approximations derived from the homogeneous electron gas (HEG) model is the most successful one. The HEG is a system of electrons moving on a positive background charge distribution such that the entire system is electrically neutral. The number of electrons N and the volume V are considered to approach infinity, while the electron density, $n = N/V$, remains finite and constant everywhere. Physically, this is an assumption of ideal metal i.e a perfect infinite crystal of valence electrons and uniformly distributed positive atoms.

The potentials used in LDA include augmented plane waves (APW), atomic orbitals (AO), Gaussian orbitals (GO), muffin-tin orbitals (MTO), and linear combinations of them (LAPW, LCAO, LCGO, LMTO). In the present thesis, TBLMTO-ASA [33, 34] based calculations, employing scalar relativistic corrections including combined correction term and Langreth-Meh-Hu gradient corrected von Barth Hedin parametrized energy and potential, have been used. The calculated theoretical results have been correlated with the experimental observation. Hence we shall discuss the LMTO method in detail.

2.4.3 Linear Muffin-tin Orbital method

The LDA reduces the many body Hamiltonian of the valence electron cloud in the presence of 'frozen' array of ion cores. The effective Hamiltonian as seen by an electron within LDA is given by,

$$V(\mathbf{r}) = \sum_{\mathbf{R}} v(\mathbf{r} - \mathbf{R}) \quad (2.32)$$

where, \mathbf{R} are the positions of ion-cores and \mathbf{r} is the position of the electron. In the neighbourhood of an ion-core, the potential seen by the electron in a solid is not very different from that in the atom whose ion-core we are focussing on. The crystal potential used in LMTO changes rapidly near the atomic sites which are considered as muffin-tin spheres and varies slowly near

the interstitial region. The muffin-tin (MT) potential V_{MT} approximates the potential by assuming it is spherically symmetrical near the atomic site and flat in the interstitial region given by,

$$V_{ext}(\mathbf{r}) = V_{MT}(\mathbf{r}) = \begin{cases} V_{ext}(r), & r \leq s \\ V_0, & r > s, \end{cases} \quad (2.33)$$

s is radius of MT spheres. The fig 2.9 shows the schematic of construction of muffin-tin potential.

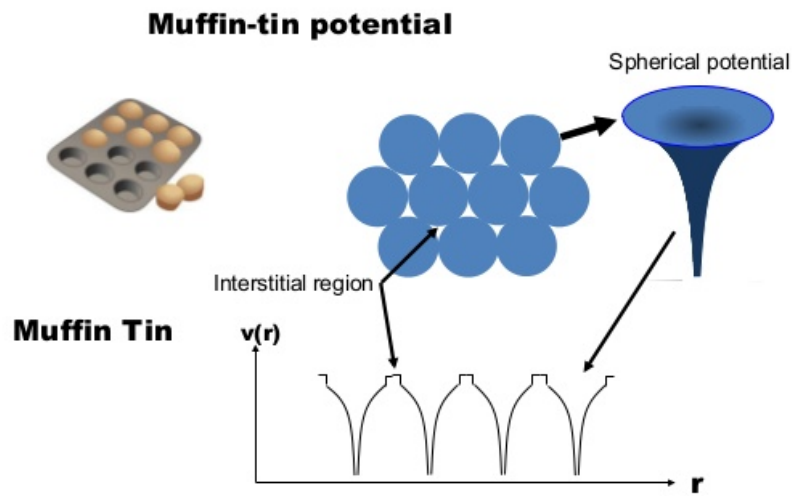


Figure 2.9: A schematic diagram of construction of Muffin-tin potential.

The wavefunction can now be expressed as a product of spherical harmonics and radial wavefunctions inside the sphere and plane waves in the interstitial region. The Atomic Sphere Approximation (ASA) chooses the MT radius in such a way that the total volume of the MT spheres are equal to the total volume of the system, which means that the spheres have a slight overlap [35]. Also, it takes the kinetic energy outside the MT sphere as zero. The MTO's are energy dependent inside the spheres. The muffin tin orbitals are linearised to create an energy independent basis set which can then be used to make the matrix element of the Hamiltonian which gives an Eigen value problem which are the solutions to the Kohn Sham equations. To calculate the matrix elements of the Hamiltonian and the wave function overlap, Anderson showed that one needs only the so called potential parameters obtained at the muffin-tin radii and the structure constants which carry information of the geometry of the lattice. The matrix elements are readily computed once the potential parameters are known and it is these parameters which are recalculated each time in the self-consistent cycle of the LMTO-ASA method.

The structure constants are computed only once and may be stored to be used repeatedly, in the self-consistent calculation. The electron-electron correlation, U and Hund's exchange term, J can be taken care by use of LDA+ $U+J$.

LMTO-ASA has its own merit and limitations which is discussed below [36]. The LMTO-ASA offers several advantages over other methods in terms of (a) easy interpretation (b) speed (c) simplicity. The muffin-tin potential defines the basis set to construct Bloch wave function of the material. The atomic wave function is constructed using only s , p , d basis function for transition metals. For rare-earths and actinides one has to include the f orbitals in the expansion of the crystal wave function. This use of a minimal basis set makes computation very fast as it requires diagonalisation of a small sized Hamiltonian. The disadvantages include (a) the limited accuracy in particular that Hellman-Feynman forces have been difficult to evaluate accurately with this method (b) the method is limited to close-packed systems. (c) for open structures, one has to use the empty spheres to make the system close packed, and it becomes inconvenient when dealing with structure optimisations The theoretical bands calculated using LMTO does not match accurately with the experimental spectra and Dynamic mean field theory (DMFT) approximation [37, 38] is required for the exact interpretation of experimental data.

Bibliography

- [1] H. Hertz; *Ann. Phys.* **31**, 983 (1887).
- [2] W. Hallwachs; *Ann. Phys.* **33**, 301 (1888).
- [3] J. J. Thomson; *Phil. Mag.* **48**, 547 (1899).
- [4] P. Lenard; *Ann. Physik* **2**, 359 (1900).
- [5] A. Einstein; *Ann. Phys.* **31**, 132 (1905).
- [6] W. E. Spicer, and C. N. Berglund; *Phys. Rev. Lett.* **12**, 9 (1964).
- [7] C. N. Berglund and W. E Spicer, *Phys. Rev.* **136**, A1044 (1964).
- [8] D. W. Turner, C. Baker, A. D. Baker, and C. R. Brundle, *Molecular Photoelectron Spectroscopy* (London: Wiley-Interscience) (1970).
- [9] D. W. Turner, and M. I. Al-Joboury, *J. Chem. Phys.* **37**, 3007 (1962).
- [10] C. Nordling, E. Sokolowski, and K. Seigbahn, *Phys. Rev.* **105**, 1676 (1957).
- [11] N. V. Smith, and L. F. Mattheiss. *Phys. Rev. B*, **9**, 1341 (1974).
- [12] N. V. Smith. *Phys. Rev. B*, **9**, 1365 (1974).
- [13] N. V. Smith, M. M. Traum, and F. J. DiSalvo. *Solid State Comm.* **15**. 211 (1974).
- [14] M. M. Traum, N. V. Smith, and F. J. DiSalvo. *Phys. Rev. Lett.* **32**, 1241 (1974).
- [15] T. Kiss, F. Kanetaka, T. Yokoya, T. Shimojima, K. Kanai, S. Shin, Y. Onuki, T. Togashi, C. Zhang, C. T. Chen, and S. Watanabe. *Phys. Rev. Lett.* **94**, 057001 (2005).
- [16] H. Y. Fan; *Phys. Rev.* **68**, 43 (1945).

- [17] H. Mayer, and H. Thomas; *Z. Phys.* **147**, 419 (1957).
- [18] H. Puff; *Phys. Stat. Sol.* **1**, 636 (1961).
- [19] Y. Liu, Angle Resolved Photoemission Studies Of Two Dimensional Electron Systems, Ph.D thesis (2010).
- [20] H. Luth, *Solid Surfaces, Interfaces, and Thin Films*, Springer, 4th edition (2001).
- [21] V. Dose, *Progress In Surface Science*, **13**, 225 (1983).
- [22] N. V. Smith, *Rep. Prog. Phys.* **51**, 1227 (1988).
- [23] P. D. Johnson, and S. L. Hulbert, *Rev. Sci. Instrum.* **61**, 2277 (1990).
- [24] D. P. Woodruff, N. V. Smith, P. D. Johnson, and W. A Royer, *Phys. Res. B* **26**, 2943 (1982).
- [25] S. Banik, A. K. Shukla, and S. R. Barman, *Rev. Sci. Instrum* **76**, 066102 (2005).
- [26] N. G. Stoffel, and P. D. Johnson, *Nucl. Inst. & Meth. A* **234**, 230 (1985).
- [27] M. Maniraj, and S. R. Barman, *Rev. Sci. Instrum.* **85**, 033301 (2014).
- [28] D. A. Shirley; in *Photoemission in Solids I*, edited by M. Cardona, and L. Ley, (Springer Verlag, Berlin, 1978) Vol **26**, p. 193
- [29] D. D. Sarma, N. Shanthi, S. R. Krishnakumar, T. Saitoh, T. Mizokawa, A. Sekiyama, K. Kobayashi, A. Fujimori, E. Weschke, R. Meier, G. Kaindl, Y. Takeda, and M. Takano, *Phys. Rev. B* **53**, 6873 (1996).
- [30] M. Born, and R. Oppenheimer, *Annalen der Physik* **389**, 457 (1927).
- [31] P. Hohenberg, and W. Kohn, *Phys. Rev. B* **136**, 864 (1964).
- [32] W. Kohn, and L. J. Sham, *Phys. Rev. A* **140**, 1133 (1965).
- [33] O. K. Anderson, *Phys. Rev. B* **12**, 3060 (1975).
- [34] O. K. Anderson, and O. Jepsen, *Phys. Rev. Lett.* **53**, 2571 (1984)
- [35] S. Barbara, and S. H. Vedene, *Phys. Rev. B* **37**, 7525 (1988)

- [36] M. Cardona, P. Fulde, K. V. Klitzing, R. Merlin, H. -J. Queisser, and H. Störmer, *Solid State Sciences*, Springer series **167** ISBN 978-3-642-15143-9
- [37] G. Kotliar, S. Y. Savrasov, K. Haule, V. S. Oudovenko, O. Parcollet, and C. A. Marianetti, *Rev. Mod. Phys.* **78**, 865 (2006).
- [38] D. Vollhardt, *Annalen der Physik* **524**, 1 (2012)

Chapter 3

Electronic structure study of Fe(Se,Te) superconductor

In this chapter, we have discussed the electronic structure of $\text{FeSe}_{1-x}\text{Te}_x$ superconductor, belonging to (11) family, using Photoemission Spectroscopy and Inverse Photoemission Spectroscopy. The experimental results have been well supported by our theoretical band structure calculations.

3.1 Introduction

The unconventional superconductivity [1] in iron based compounds [2, 3] has attracted much attention due to its importance in elucidating a consolidated understanding of superconductivity in general. Unlike the cuprate High T_c materials, superconductivity in these compounds involves some exotic interplay of structural and magnetic degrees of freedom. Although among them, Fe(Se,Te) is rather simple from a structural point of view, it shows a strong bearing of the spin fluctuations and structural and magnetic disorder on its superconducting properties. The emergence of superconductivity without doping and the absence of spacer layer in these systems, in contrast to the other Fe superconductors make Fe(Se,Te) an interesting candidate for research and extensive theoretical and experimental studies focussing on the electronic structure of this system have been undertaken.

Theoretical calculations indicate that the Fermi surface of Fe(Se,Te) consists of two hole cylinders near the zone center and two lighter compensating electron cylinders around the zone corner [4]. The relatively stronger correlation in Fe(Se,Te) systems in comparison to other Fe superconductors [5, 6], leads to a complex pairing symmetry and unconventional superconductivity. ARPES studies demonstrate an isotropic superconducting gap derived from the strong

coupling [7, 8]. Further, a sign reversing gap between the hole and the electron Fermi-surface pockets ($s\pm$ wave), favoring the unconventional pairing mechanism associated with spin fluctuations has been confirmed [1, 9]. Recent reports have indicated that the electronic structure of Fe(Se,Te) are in the BCS-BEC cross over regime [10, 11]. The superconducting gap indicates composite superconductivity consisting of strong coupling BEC in the electron band and weak coupling BCS like superconductivity in the hole band [11].

Despite, a number of reports addressing many of the issues, the roles of electron-phonon coupling, spin density wave states, quasiparticles etc. are still under intense debate. Many exotic properties of these superconductors originate from some of the key elements like magnetic fluctuations, unconventional electron-phonon coupling and electron correlations. Further, the multiorbital correlation in combination with Hund's coupling caused by the participation of all five Fe 3d electrons result in some distinctive electronic properties like orbital selectivity [1, 12, 13], Mottness [14], quantum phase transition [15], nematicity [16], pseudogap [17] etc.

Presence of pseudogaps is a characteristic feature of the family of unconventional superconductors such as high T_c cuprates [18, 19], heavy fermion superconductors [20] and the recently discovered iron pnictides and chalcogenides [21–23]. In last few years, correlation of the pseudogap with the superconducting state has been under intense study. Although, the origin of pseudogap in these materials is still under debate, a general consensus is prevailing among researchers about the existence of two types of pseudogaps, located at low and high binding energies in high T_c superconductors. The low energy pseudogap which originates from superconducting fluctuations [24, 25] persists just above T_c where as the origin of high energy pseudogap existing far above T_c is still a puzzle [26, 27]. Nevertheless, electron correlation is considered to play a vital role in the existence of the high temperature pseudogap in unconventional superconductors [28] like the case of manganites [29]. The electronic properties of these superconductors with their moderate electron correlations, are controlled mostly by the competing inter- and intra- orbital interactions near the E_F region. It has been pointed out [30] that these interactions generate an Orbital Selective Mott Phase (OSMP) in which electrons in some orbitals are Mott localized while others remain itinerant. Earlier, such an OSMP was identified in $\text{Ca}_{2-x}\text{Sr}_x\text{RuO}_4$ [31, 32]. Recently, a doping dependent OSMP was proposed to be present in Fe(Se,Te) by *Craco et al.* and *Aichhorn et al.* [33, 34] from a theoretical point of view.

Electron spectroscopic methods are considered to be quite suited to probe the near E_F electronic structure and thereby the nature of pseudogaps. Although a number of photoemission studies [10, 35, 36] focussed on the electronic structure of valence band (occupied states) and the pseudogap formation in the Fe(Se,Te) system, their origins and nature are still not clear. Moreover, a detailed investigation of the unoccupied states are also not reported. In this study, photoemission spectroscopy (PES) and inverse photoemission spectroscopy (IPES) in conjunction with LDA based band structure calculations have been used to understand the detailed near E_F electronic structure of Fe(Se,Te). Changes in the Fe 3d - Se 4p/Te 5p correlation strength with doping or temperature lead to noticeable spectral weight shifts in the near E_F states in PES and IPES which could be intimately related to the structural changes of the Fe(Se,Te)₄ tetrahedra. The temperature dependent normal state pseudogap observed in PES has been correlated to the insulating behavior originating from the multi-orbital correlation and the Hund's coupling. Based on our theoretical calculations it is shown that the formation of such a pseudogap could be a signature of the temperature induced Orbital Selective Mott Transition (OSMT). The Coulomb correlation energies in Fe(Se,Te) systems have been estimated from the combined PES and IPES spectra.

3.2 Experimental

Polycrystalline samples of FeSe_{1-x}Te_x ($x = 1, 0.5, 0$) used in this study were synthesized via solid state reaction route [37] and characterized for their electrical, magnetic and structural properties [38]. In order to avoid a common source of error in the spectroscopic analysis of these compounds, it was ensured that the samples contain no excess Fe and are of single phase in nature. Angle integrated ultraviolet photoemission measurements were performed by using an ultra high vacuum system equipped with a high intensity vacuum-ultraviolet source and a hemispherical electron energy analyzer (SCIENTA R3000). At the He *I* ($h\nu = 21.2$ eV) line, the photon flux was of the order of 10^{16} photons/sec/steradian with a beam spot of 2 mm diameter. Fermi energies for all measurements were calibrated by using a freshly evaporated Ag film on a sample holder. The total energy resolution, estimated from the width of the Fermi edge, was about 27 meV for He *I* excitation. Inverse photoemission spectroscopic (IPES) measurements were performed in the isochromat mode with a mean photon energy of 9.9 eV using a combination of electrostatically focussed Stoffel Johnson type electron gun with

a contact potential [39] and an acetone gas filled photon band pass detector with a CaF_2 window [40,41]. The total energy resolution of IPES measurements were ~ 600 meV. IPES spectra were obtained by normalizing the measured photon counts by the sample current at each energy step. The binding energy has been determined with reference to the Fermi level of a sputter cleaned silver surface. All the measurements were performed inside the analysis chamber under a base vacuum of $\sim 5.0 \times 10^{-11}$ mbar. The polycrystalline samples were repeatedly scraped using a diamond file inside the preparation chamber with a base vacuum of $\sim 5.0 \times 10^{-11}$ mbar and the spectra were taken within 1 hour, so as to avoid any surface degradation. All measurements were repeated many times to ensure the reproducibility of the spectra. For the temperature dependent measurements, the samples were cooled down by pumping liquid nitrogen through the sample manipulator fitted with a cryostat. Sample temperatures were measured using a silicon diode sensor touching the bottom of the stainless steel sample plate. The low temperature photoemission measurements at 77 K were performed immediately after cleaning the sample surfaces followed by the room temperature measurements.

In order to understand the observed changes in the near E_F spectral features we used TBLMTO-ASA [42] calculations employing scalar relativistic corrections including combined correction term and Langreth-Meh-Hu gradient corrected von Barth Hedin parametrized energy and potential. The experimental lattice parameters at 300K were used in the calculations [38]. The correlation effects of the Fe-d orbitals were taken into account by using LDA+U formulism with J as 0.9 eV [34], and U as 3.5 eV for FeTe and 4.0 eV for FeSe [6]. For the $\text{FeSe}_{0.5}\text{Te}_{0.5}$ U was taken as 3.8 eV, a value intermediate between those of FeTe and FeSe.

3.3 Results and Discussion

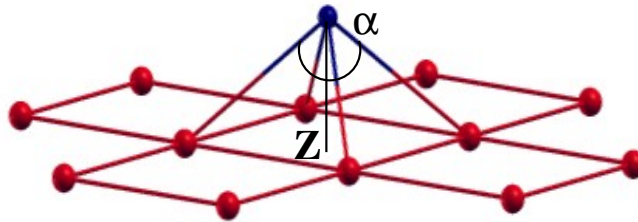


Figure 3.1: Structure of $\text{Fe}(\text{Se},\text{Te})_4$ tetrahedra showing the chalcogen height Z and angle α . Red and blue spheres correspond to Fe and Se/Te atoms respectively.

The structure of $\text{FeSe}_{1-x}\text{Te}_x$ compounds consists of a stacking of edge sharing $\text{Fe}(\text{Se},\text{Te})_4$ tetrahedra without any spacer layer in between [3] as shown in figure 3.1. The chalcogen height (height of Se/Te atom from the Fe plane) and the Fe-Se/Te-Fe bond angle (α) is also marked. The parent compound FeTe is a non superconductor and exhibits a monoclinic structure at low temperature. It also shows an antiferromagnetic spin density wave (SDW) transition at 70 K [43]. The other parent, FeSe is a superconductor with a T_c of 8 K [44], which increases to 37 K under a pressure of $\sim 4\text{GPa}$ [45]. Recently, T_c of $\sim 100\text{K}$ has been observed in single layer FeSe films on doped SrTiO_3 [46]. Substitution of Se at the Te site enhances the T_c to a maximum of 15 K for $x = 0.5$ [3], on the contrary, it is expected that disorder should reduce the superconducting transition temperature, T_c [47]. This enhancement is reported to be linked to the local structural symmetry breaking [48] and the degree of disorder caused by the smaller ionic radius of Se [3]. Recent report by Wang et al. [49] have demonstrated the topological nature of $\text{FeSe}_{0.5}\text{Te}_{0.5}$ characterised by Dirac cone type surface states.

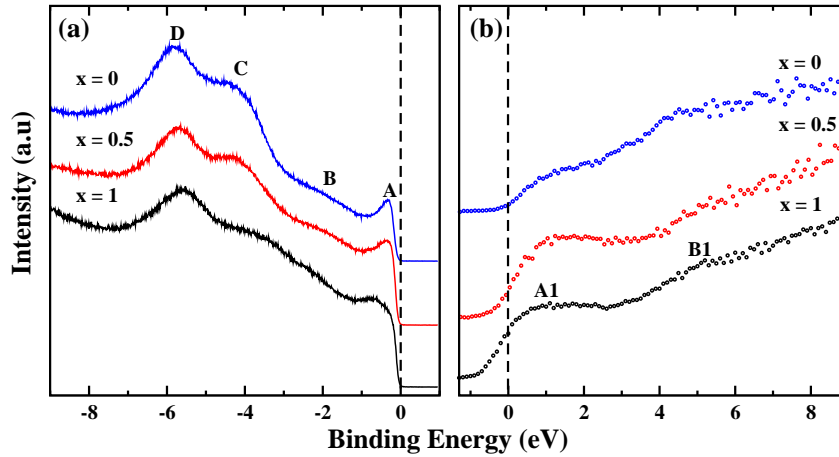


Figure 3.2: (a) High resolution (a) PES (b) IPES spectra taken at 300K for He I Valence band spectra measured at 300 K for $\text{FeSe}_{1-x}\text{Te}_x$ ($x = 1, 0.5, 0$). The features are marked as A, B, C and D. (b) IPES spectra for $\text{FeSe}_{1-x}\text{Te}_x$ ($x = 1, 0.5, 0$ shown in black, red and blue respectively) with marked features A and B. Dashed vertical lines correspond to the Fermi level.

Figure 3.2(a) shows the valence band spectra of $\text{FeSe}_{1-x}\text{Te}_x$ ($x = 1, 0.5, 0$) samples taken at He I photon energy. The spectra for all the compositions show four major features marked as A, B, C and D positioned at 0.5, 2, 4 and 6 eV respectively. The broadened feature A seen in the case of FeTe transforms into a sharp peak for FeSe. Feature C becomes prominent and shifts to higher binding energy with increasing Se content. Further, feature D also shifts to higher binding energy with Se doping. Panel (b) of figure 3.2 shows the inverse photoemission spectra

of the $\text{FeSe}_{1-x}\text{Te}_x$ samples, taken at room temperature, depicting the unoccupied density of states. The experimental spectra show two prominent features A1 and B1 located at binding energy positions 1 and 5.5 eV respectively. B1 is less prominent due to the electron scattering inverse photoemission process [50].

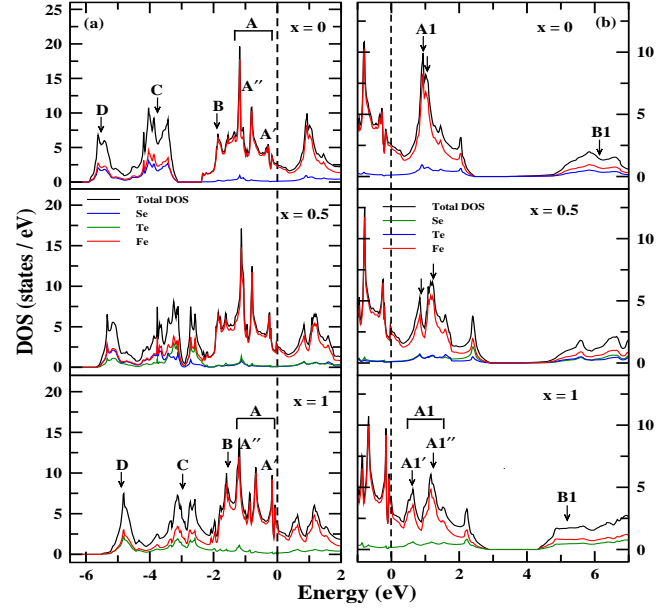


Figure 3.3: Theoretically calculated (a) Total occupied DOS and (b) total unoccupied DOS, for $\text{FeSe}_{1-x}\text{Te}_x$ ($x = 1, 0.5, 0$). The theoretical features which matches with experiment has been marked as A, B, C and D in (a) and A1 and B1 in (b). The sub features of A (A' and A'') and A1 ($A1'$ and $A1''$) are also marked.

To explore the orbital contribution of the observed experimental features the TBLMTO-ASA based band structure calculations for occupied and unoccupied density of states are plotted in fig 3.3(a,b). Features A and B exhibit predominant Fe 3d character, C represents hybridized Fe 3d - Se 4p/Te 5p states while D corresponds to Se 4p/Te 5p states. For FeTe, the features B and C merge while in case of FeSe, a clear gap is seen in the calculated DOS, which is in accordance with the experimental results. Se doping shifts the features C and D towards higher binding energy owing to the greater electronegativity of Se (2.4) in comparison to Te (2.1). Further the feature A is composed of two sub features A' (-0.15 eV) and A'' (-1.0 eV). The unoccupied density of states plotted in fig 3.3(b) indicates that A1 arises primarily from the Fe-3d states with a small contribution from the chalcogen (Se/Te) p states and B1 consists predominantly of the hybridised Fe3d-Se4p/Te5p unoccupied states. Further, feature A1 comprises of $A1'$ (0.6 eV) and $A1''$ (1.2 eV). These assignments of features in occupied and unoccupied

states are in agreement with other's calculations also [6, 51].

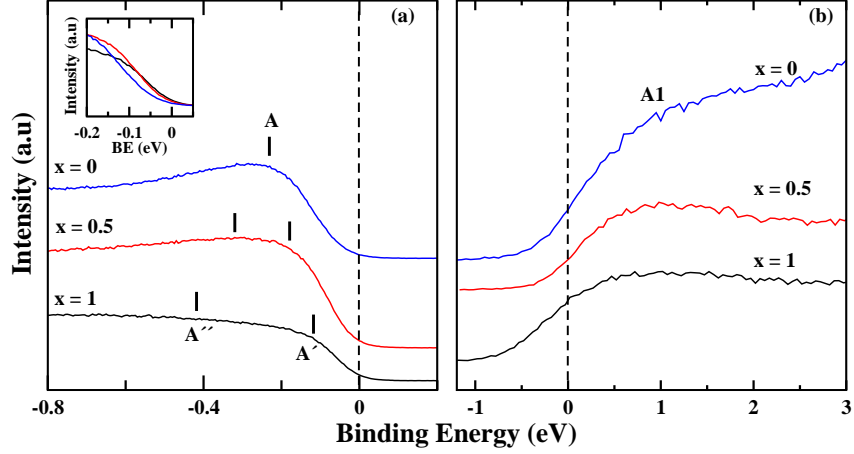


Figure 3.4: High Resolution (a) PES and (b) IPES spectra taken at 300 K for $\text{FeSe}_{1-x}\text{Te}_x$ ($x = 1, 0.5, 0$ shown in black, red and blue respectively). Features A' and A'' are denoted by black bars in (a). Inset of (a) shows the expanded view near the E_F .

In order to see the finer changes in the near E_F electronic structure we have taken a set of high resolution spectra of this region around E_F . In Figure 3.4(a,b) we have plotted the PES and IPES spectra from the three compositions taken at room temperature. As we see, from fig 3.4(a), the feature A consists of two features A' and A'' positioned at 0.1 and 0.5 eV respectively. These features correspond to the features in DOS calculations A' (0.15 eV) and A'' (1.0 eV). The discrepancy in the energy positions could be due to the self-energy correction which is neglected in the calculations [52]. As we go from FeTe to FeSe, the energy separation between these two features keep decreasing and intensity of A'' increases. Thus, the doublet structure in case of FeTe transforms into a prominent peak with a weak shoulder in case of FeSe. Thus, with increase in the Se content from 0 to 1 the intensity of peak A increases. It can also be seen, that some of the electronic states at the E_F get depleted (from the inset of fig 3.4(a)) with Se doping and the spectral weight at E_F shift to higher binding energy positions at A. Similar spectral change in PES with doping was earlier reported by Yokoya et al. [51] also. Such a shift in the spectral weight is a signature of the presence of a pseudogap in the case of FeSe. In complementary to PES, a reduced spectral weight near the Fermi level (E_F) with Se doping is seen in IPES spectra plotted in fig 3.4(b). The sub features of A1 are not resolved experimentally in IPES. The depletion of spectral weight near E_F with Se substitution is in conformity with the reports by Saini et al. [53] based on their studies using X-ray absorption spectroscopy (XAS) in which the electronic structure of unoccupied states of $\text{FeSe}_{1-x}\text{Te}_x$ are

probed.

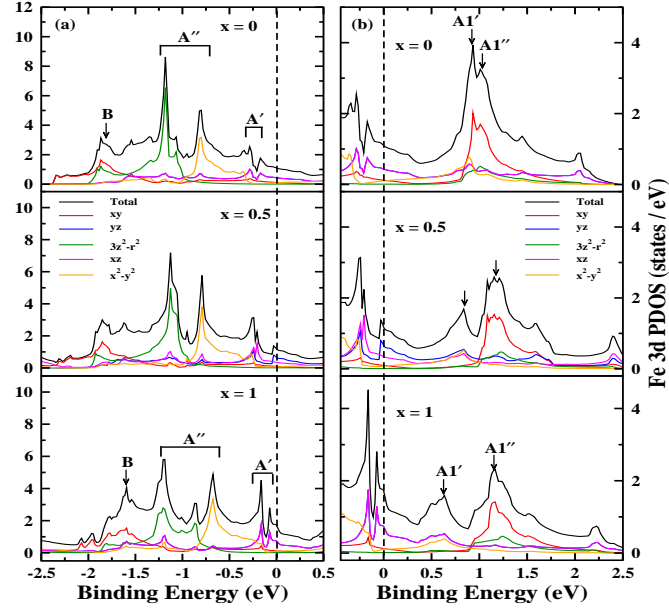


Figure 3.5: Fe 3d Partial DOS, using LDA+U, (a) Total occupied DOS and (b) total unoccupied DOS, for $\text{FeSe}_{1-x}\text{Te}_x$ ($x = 1, 0.5, 0$), with marked features. The PDOS contribution for xz (magenta) and yz (blue) orbitals are same for FeTe and FeSe. For $\text{FeSe}_{0.5}\text{Te}_{0.5}$, the xz and yz PDOS split owing to the different bond length of Fe-Te and Fe-Se.

The depleted occupied as well as unoccupied DOS near E_F is associated with the changes in the tetragonal crystal structure of Fe(Se,Te). Substitution of Se for Te in FeTe leads to an increase in the Se/Te - Fe - Se/Te bond angle (α shown in fig 3.1). The angle α which is 95° in case of FeTe, approaches the ideal tetrahedron value of 109.5° with Se doping [54]. Similarly, the chalcogen height (z) decreases from 1.78 \AA to 1.46 \AA with Se doping [6]. The bond angle and chalcogen height is determinant to the overlap between the iron and chalcogen orbitals, resulting in a stronger hybridization between the Fe 3d and the chalcogen p orbitals. In addition an enhancement of Fe-3d interorbital hoppings via chalcogen p orbitals occur at reduced chalcogen height. This leads to an enhanced splitting of lower and upper Fe-3d bands (situated in valence and conduction bands respectively) and thereby a reduction in density of states near E_F [6]. The role of Fe 3d - chalcogen p hybridisation in the unoccupied region is supported by the experimental results of Saini et al. [53]. This study demonstrates that the Fe-3d unoccupied states display a gradual decrease in spectral intensity with Se substitution. The experimental observation, supported by cluster model calculations, correlate the spectral weight depletion to the enhanced hybridisation of chalcogen p orbitals with the Fe 3d orbitals. The increased chalcogen p - Fe-3d hybridisation for FeSe in comparison to FeTe is also evidenced from the

Fe K edge X ray absorption near edge spectra (XANES) [55] which probes the unoccupied Fe-chalcogen hybridised states. Thus, the change in hybridisation strength of the Fe-3d - Se-4p/Te-5p states govern the electronic structure of the $\text{FeSe}_{1-x}\text{Te}_x$ system and result in a reduced density of states near Fermi level with Se doping, both in the occupied and unoccupied region.

The nature of bands involved in the formation of the pseudogap and in the spectral weight shifts could well be identified from our Fe 3d partial density of states (PDOS) calculations using the TB-LMTO ASA method. Figure 3.5 shows the Fe 3d occupied (a) and unoccupied (b) PDOS of the $\text{FeSe}_{1-x}\text{Te}_x$ system. Although, FeSe, FeTe and $\text{FeSe}_{0.5}\text{Te}_{0.5}$ have tetragonal symmetry, different Fe-Se and Fe-Te bond lengths in case of $\text{FeSe}_{0.5}\text{Te}_{0.5}$ reduce the space group symmetry to 99 (P4mm) [56]. The lower symmetry in case of $\text{FeSe}_{0.5}\text{Te}_{0.5}$ results in the lifting of the degeneracy of xz/yz orbitals (as seen from fig 3.5). The occupied PDOS (fig 3.5(a)) reveals that xz/yz and x^2-y^2 orbitals are the most populated ones at 0.15 eV (A') while the feature at 1 eV (A'') corresponds to states mostly populated with $3z^2-r^2$. The feature at ~ 0.15 eV shifts back to higher binding energy and becomes less prominent with doping of Se in place of Te. On the contrary, the feature at ~ 1.0 eV shifts towards E_F and the plateau at ~ 0.8 eV reduces with Se incorporation. The above effect results in an enhanced DOS for FeSe in comparison to FeTe at 0.5 eV in the PES spectra. Similarly, the unoccupied Fe-3d DOS reveal that the xz/yz and x^2-y^2 orbitals are the highest populated ones corresponding to the feature $A1'$ while the xy orbital is the highest for $A1''$. The feature $A1'$ moves away from the E_F while the feature $A1''$ moves towards the E_F in addition to an intensity enhancement of both $A1'$ and $A1''$ (fig 3.3(b)). The intensity of xy and x^2-y^2 orbitals could be seen to be increasing with the reduction in the doping value x, leading to the increase in the intensity of $A1$.

To explore the change in Fe-3d orbital contribution with Se doping, we have plotted the occupied Fe-3d orbital contribution in fig 3.6. Replacement of Te by Se leads to decrease in chalcogen height, which affects the occupancy of the out of plane Fe-3d orbitals, $3z^2-r^2$ - xz/yz. The reduced chalcogen height (z) and increased bond angle with Se doping results in a stronger hybridization of Fe 3d - chalcogen p orbitals and an enhanced Fe-3d interorbital hoppings. As can be seen from the fig 3.6, the DOS contribution for $3z^2-r^2$ and xy orbitals is very less near E_F while x^2-y^2 and yz/zx orbitals contribute significantly to the density of states near E_F . This large DOS at the Fermi level leads to remarkable electron correlation effects for the latter orbitals. Substitution of Se, causes a reduction in z which affects the hybridisation of the Fe-3d - chalcogen p orbitals and the Fe-3d interorbitals. The hybridisation between x^2-y^2 - $3z^2-r^2$ and

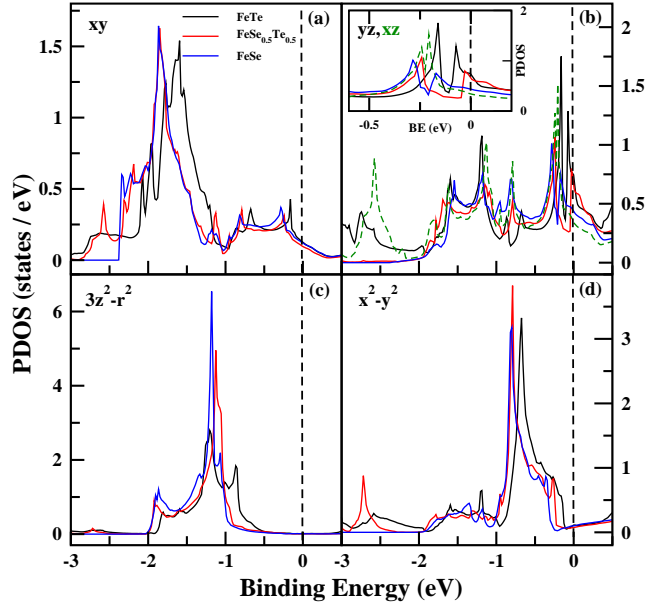


Figure 3.6: The individual contributions of (a) xy , (b) yz/xz , (c) $3z^2-r^2$ and (d) x^2-y^2 orbitals to Fe 3d partial DOS for FeTe, FeSe_{0.5}Te_{0.5} and FeSe. Inset of (b) represents the expanded PDOS near E_F for yz (solid lines) and xz (dotted green line, for FeSe_{0.5}Te_{0.5}) orbitals. The reduced symmetry in case of FeSe_{0.5}Te_{0.5} lifts the degeneracy of xz and yz orbitals, thus the PDOS contribution splits which is otherwise same in case of FeTe and FeSe.

$yz/zx - xy$ orbitals is enhanced with Se doping due to the lowering of chalcogen height. This is reflected as an orbital selective weight transfer in fig 3.6, whereby, the occupancy of x^2-y^2 and yz/zx orbitals reduces near E_F with a simultaneous increase in occupancy of $3z^2-r^2$ orbitals at higher binding energy. This change in orbital occupancy is reflected as the spectral weight shifts which in turn results in the formation of a pseudogap with Se doping in the valence band.

Figure 3.7(a,b) depicts the near E_F PES spectra of FeSe_{1-x}Te_x taken at 300 K (black) and 77 K (red). The feature A, originating from Fe 3d states shows an enhancement in its intensity as the temperature is lowered. Although, in case of FeTe this increase is very small, substitution of half of Te with Se results in a marked change. It should be noted that with further increase in Se content, this enhancement of intensity of peak A becomes weaker, though still distinct. Associated with this increase in intensity there is a depletion of states at the Fermi level. Further, it can be seen that the area by which the A peak has increased does not match with the number of states depleted from the near E_F position. This indicates that electrons from other orbitals also shift resulting in the increase in its intensity. It should be noted that, depletion of these states from the near E_F clearly indicates an opening up of a

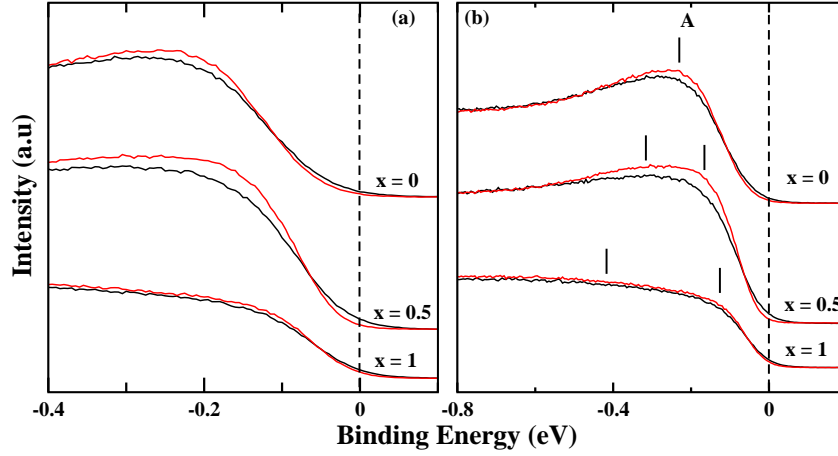


Figure 3.7: (a) Enlarged view of high resolution PES spectra measured at 300 K (black) and 77 K (red) for $\text{FeSe}_{1-x}\text{Te}_x$ ($x = 1, 0.5, 0$). (b) PES spectra in the energy range -0.8 -0.2 eV.

pseudogap as the temperature is lowered from 300 K to 77 K. Moreover, the spectral weight transfer is weak in case of FeTe while $\text{FeSe}_{0.5}\text{Te}_{0.5}$ exhibits a significant shift. A comparison of the figures 3.4(a) and 3.7(a) will reveal that the doping dependent spectral weight transfer is similar to the temperature dependent transfer in the respect of their energy positions. It has been reported earlier that lowering the temperature results in the reduction in the Fe-chalcogen height (Z shown in fig 3.1) in case of FeTe and $\text{FeSe}_{0.5}\text{Te}_{0.5}$ while a slight increase in case of FeSe [57]. The magnitude of this decrease is greater in case of $\text{FeSe}_{0.5}\text{Te}_{0.5}$ compared to FeTe. Thus, at 77 K, $\text{FeSe}_{0.5}\text{Te}_{0.5}$ has the shortest chalcogen height while FeTe the longest. The reduced chalcogen height at low temperature in case of $\text{FeSe}_{0.5}\text{Te}_{0.5}$ ensures the strongest hybridization between the Fe-3d orbitals. This reflects in the maximum spectral weight transfer to higher binding energy in comparison to both the parent compounds. As mentioned before, in an analogy with the doping dependent case discussed earlier, the reduction in the chalcogen height shifts the electron occupancy from the xz/yz and x^2-y^2 to the $3z^2-r^2$ orbitals resulting in the temperature dependent spectral weight transfer and thereby the pseudogap. This is a temperature induced crossover from a metallic state in which all the t_{2g} orbitals ($xy, xz/yz$) near the E_F are occupied to a state in which occupancy of the xz/yz orbitals are depleted, signifying a Mott transition. This kind of spectral weight transfer which is a characteristic of Mottness [58], has earlier been identified as Orbital Selective Mott Transition (OSMT) [30]. Our study presents the first observation of a temperature induced crossover to a low temperature OSM phase in the family of Fe chalcogenides although such phenomena was earlier observed

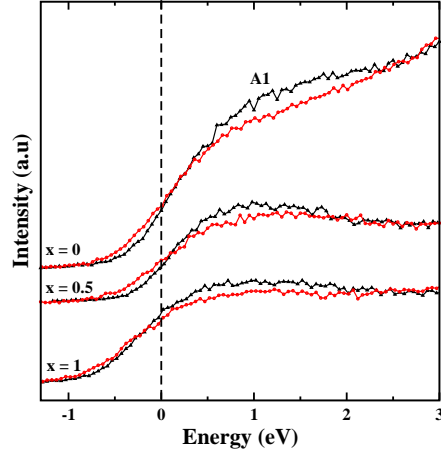


Figure 3.8: Temperature dependent IPES spectra taken at 300 K (black) and 77 K (red) for $\text{FeSe}_{1-x}\text{Te}_{1-x}$ ($x = 1, 0.5, 0$)

in $\text{A}_x\text{Fe}_{2-y}\text{Se}_2$ ($A = \text{K, Rb}$) where a high temperature OSM phase was identified [28].

Such spectral weight redistributions with lowering of temperature were earlier ascribed to the spin density wave transition (SDW) in FeTe by *Zhang et al.* [35] who concluded that the suppression of the SDW is the cause of the reduction in the near E_F spectral weight at low temperatures. But, our observation of a stronger spectral weight shift in case of $\text{FeSe}_{0.5}\text{Te}_{0.5}$ compared to that of FeTe shows that the spectral weight shift in this case is not related to the SDW transition. A recent ARPES study [59] has reported the evolution of the spectral feature (a hump which corresponds to feature A in our data) as a function of x . The intensity of the hump was found to reduce with decreasing Se content. This study points at the role of electronic correlations driving the system close to the Mott metal insulator transition. Another ARPES study, temperature dependent, by *Liu et al.* [60] have reported a peak-dip-hump line shape in case of $\text{Fe}_{1.02}\text{Te}$ across its antiferromagnetic transition at 70 K. This study has shown the hump to become broader as the temperature is lowered below 50 K and explained the results in terms of the strength of polarons. It should be noted that the spectral weight shifts observed by us are all above the Neel temperature. Nevertheless, these results together highlight the intricate electron correlation in the near E_F states over a broad range of temperature.

Fig 3.8 shows the IPES spectra of $\text{FeSe}_{1-x}\text{Te}_x$ taken at 300 K (black) and 77 K (red). Quite similar to the spectral changes observed as a function of doping, the intensity of the feature A1 increases for higher temperature. Further, such a change in A1 could be seen for all the three compositions. This shows that the increase in the doping value and increase in the temperature have similar bearings on the spectral weight shifts which lead to the pseudogap. Moreover, such

a temperature dependent change also shows that these spectral weight shifts are inherent to the samples and are not artefacts arising from spectral normalisation or sample surface cleaning.

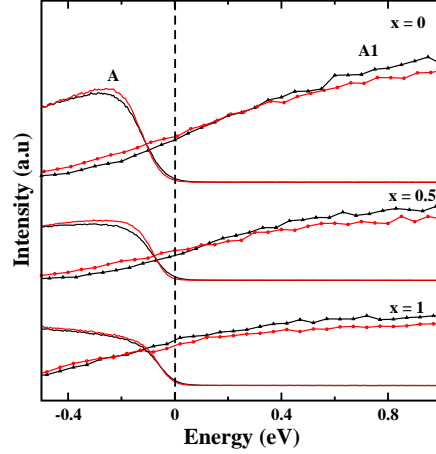


Figure 3.9: PES spectrum (solid lines) measured using He I (21.2 eV) below the Fermi level (dashed vertical line) and IPES spectra (dots+lines) at 9.2 eV photon energy above Fermi level for $\text{FeSe}_{1-x}\text{Te}_x$ ($x = 1, 0.5, 0$). The black and red spectra correspond to data taken at 300 K and 77 K respectively.

In order to understand the origin of the observed temperature dependent pseudogap in IPES which depict the unoccupied states, we have compared our results with the photoemission spectra (PES) representing the occupied states. A comparison between the temperature dependent photoemission spectra and the IPES spectra is shown in fig 3.9. The figure shows an enhancement of states for the feature A in the occupied region ($-0.5 \text{ eV} - E_F$ energy range) and a complimentary depletion of states for feature A1 in the unoccupied region ($E_F - 1 \text{ eV}$ range) at low temperature. This temperature dependent enhancement in PES was attributed to the change in the chalcogen height (Z) from the Fe plane at low temperature. Reduction in Z at low temperature causes change in the hybridisation between Fe 3d and chalcogen p orbitals. This result in the enhancement of spectral weight for feature A due to the increased occupancy of the $3z^2-r^2$ orbitals at low temperature. The spectral weight in IPES has a direct correspondence to the same in PES. Thus, the enhancement in spectral weight of $3z^2-r^2$ orbitals in the occupied side manifests as depletion of states in the unoccupied side. This explains the observed changes in features A1' and A1'' with temperature. Our result is consistent with the temperature dependent Fe K edge XAS measurements [61], showing an enhancement of pre peak A, at low temperature in $\text{FeSe}_{1-x}\text{Te}_x$, which has been correlated to the enhanced hybridisation of Fe-3d and chalcogen-p orbitals due to the decreased chalcogen height (h) at low temperature.

In Figure 3.10 we have compared the spectra collected using the HeI and HeII photons for

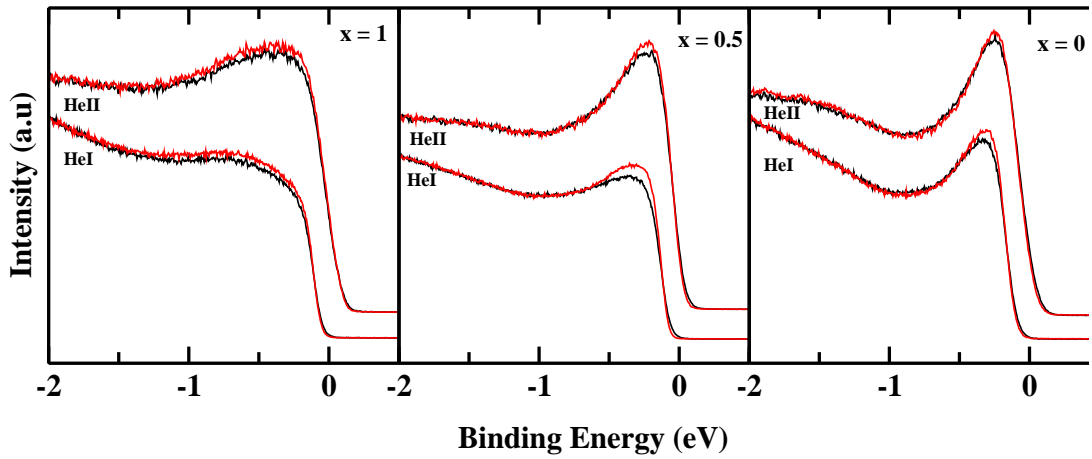


Figure 3.10: Comparison of HeI and HeII spectra for FeSe_{1-x}Te_x ($x = 1, 0.5, 0$) measured at 300 K (black) and 77 K (red).

FeTe, FeTe_{0.5}Se_{0.5} and FeSe respectively. The black and red spectra correspond to data taken at 300 K and 77 K respectively. There is an enhancement of Fe 3d derived states in case of He II for all the compositions due to the higher cross section of Fe 3d at the He II energy. The spectral weight shifts and thereby arising pseudogap described above follow the same trend in case of He II also but with a lower magnitude compared to He I.

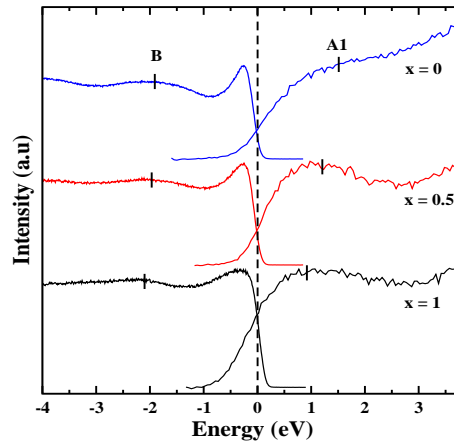


Figure 3.11: The PES and IPES spectra below and above the Fermi level respectively, for FeTe (black), FeSe_{0.5}Te_{0.5} (blue) and FeSe (red). The black ticks correspond to the positions of A1 and B.

By combining the spectra from PES and IPES we can estimate some of the energy scales involved in the electronic transport in this family of Fe superconductors, like the onsite Coulomb energy (U). The feature B in the valence band spectra and A1 in the IPES spectra are ascribed to the lower and upper Hubbard band respectively [34]. The energy separation between B and

A1 provides a rough estimate of the onsite Coulomb energy, U [62]. Fig. 3.11 shows the PES spectra taken using He II (40.8 eV) source and IPES spectra at 9.9 eV photon energy, of the $\text{FeSe}_{1-x}\text{Te}_x$ system plotted together by aligning the corresponding Fermi energies. From the plot the value of U was estimated to be $\sim 3.5, 3.4, 3.2$ eV for FeSe, $\text{FeSe}_{0.5}\text{Te}_{0.5}$ and FeTe respectively. The estimated U for FeSe is comparable to the result obtained experimentally by Yokoya et al. [51]. Chen et al. [63] reported a U value of 4.0 using X-ray Absorption Spectroscopy (XAS) and X-ray Emission Spectroscopy (XES). Further, it should be noted that U increases in $\text{FeSe}_{1-x}\text{Te}_x$ with decreasing x . Such a trend was earlier predicted by using theoretical calculations [6]. The gap in the density of unoccupied states with doping of Se leads to a shifting of the Upper Hubbard band A1 towards higher energy which signifies the enhancement of electron correlation with doping.

3.4 Conclusion

A systematic study of the electronic structure of $\text{FeSe}_{1-x}\text{Te}_x$, using PES and IPES has been done and the results have been interpreted using our theoretical band structure calculations. A doping and temperature dependent pseudogap formation reflecting the role of chalcogen height in this system is observed. The strong orbital dependent spectral weight transfer at low temperature observed in the valence band, suggests that these compounds are in close proximity with Mottness. Using theoretical band structure calculations we have shown that the spectral weight transfer is due to the shifting of the electron occupancy from the xz/yz and x^2-y^2 orbitals to the $3z^2-r^2$ indicating a temperature induced crossover from a metallic state to an Orbital Selective Mott (OSM) Phase. The temperature dependency of the pseudogap in the unoccupied region is complementary to the observed pseudogap in the occupied region. We have also estimated the Coulomb correlation energy for different doping concentrations which demonstrate that the electron correlations in Fe(Se,Te) superconductors do have a bearing on the change in their geometric structure.

Bibliography

- [1] T. Hanaguri, S. Niitaka, K. Kuroki, and H. Takagi, *Science* **328**, 474 (2010).
- [2] Y. Kamihara, H. Hiramatsu, M. Hirano, R. Kawamura, H. Yanagi, T. Kamiya, and H. Hosono, *J. Am. Chem. Soc.* **128**, 10012 (2006).
- [3] K.-W. Yeh, T.-W. Huang, Y.L. Huang, T.-K. Chen, F.-C. Hsu, P.M. Wu, Y.-Y. Lee, Y.-Y. Chu, C.-L. Chen, J.-Y. Luo, D.-C. Yan, and M.-K. Wu, *Europhys. Lett.* **84**, 37002 (2008).
- [4] A. Subedi, L. Zhang, D.J. Singh, and M.H. Du, *Phys. Rev. B* **78**, 134514 (2008).
- [5] A. Tamai, A. Y. Ganin, E. Rozbicki, J. Bacsá, W. Meevasana, P. D. C. King, M. Caffio, R. Schaub, S. Margadonna, K. Prassides, M. J. Rosseinsky, and F. Baumberger *Phys. Rev. Lett.* **104**, 097002 (2010).
- [6] T. Miyake, K. Nakamura, R. Arita, and M. Imada, *J. Phys. Soc. Jpn.* **79**, 044705 (2010).
- [7] K. Nakayama, T. Sato, P. Richard, T. Kawahara, Y. Sekiba, T. Qian, G. F. Chen, J. L. Luo, N. L. Wang, H. Ding, and T. Takahashi, *Phys. Rev. Lett.* **105**, 197001 (2010).
- [8] H. Miao, P. Richard, Y. Tanaka, K. Nakayama, T. Qian, K. Umezawa, T. Sato, Y.-M. Xu, Y. B. Shi, N. Xu, X.-P. Wang, P. Zhang, H.-B. Yang, Z.-J. Xu, J. S. Wen, G.-D. Gu, X. Dai, J.-P. Hu, T. Takahashi, and H. Ding, *Phys. Rev. B* **85** 094506 (2012).
- [9] K. Okazaki, Y. Ito, Y. Ota, Y. Kotani, T. Shimojima, T. Kiss, S. Watanabe, C.-T. Chen, S. Niitaka, T. Hanaguri, H. Takagi, A. Chainani, and S. Shin, *Phys. Rev. Lett.* **109**, 237011 (2012).
- [10] K. Okazaki, Y. Ito, Y. Ota, Y. Kotani, T. Shimojima, T. Kiss, S. Watanabe, C.-T. Chen, S. Niitaka, T. Hanaguri, H. Takagi, A. Chainani, and S. Shin, *Sci. Rep.* **4**, 4109 (2014).

- [11] Y. Lubashevsky, E. Lahoud, K. Chashka, D. Podolsky, and A. Kanigel, *Nature Physics* **8**, 309 (2012)
- [12] H. Lohani, P. Mishra, and B. R. Sekhar, *Physica C* **512**, 54 (2015).
- [13] N. Lanatá, U. R. H. Strand, G. Giovannetti, B. Hellsing, Medici Luca dè, and M. Capone, *Phys. Rev. B.* **87**, 045122 (2013).
- [14] Medici Luca dè, G. Giovannetti, and M. Capone, *Phys. Rev. Lett.* **112**, 177001 (2014).
- [15] Julián Rinçon, Adriana Moreo, Gonzalo Alvarez, and Elbio Dagotto, *Phys. Rev. B* **90**, 241105 (2014).
- [16] J.K. Glasbrenner, I.I. Mazin, H.O. Jeschke, P.J. Hirschfeld, and R. Valenti, arXiv:1501.04946 (2015).
- [17] L. Craco, and M.S. Laad, arXiv:1001.3273 (2010).
- [18] T. Timusk, and B. Statt, *Rep. Prog. Phys.* **62**, 61 (1999).
- [19] M.R. Norman, D. Pines, and C. Kallin, *Adv. Phys.* **54**, 715 (2005).
- [20] V.A. Sidorov, M. Nicklas, P.G. Pagliuso, J.L. Sarrao, Y. Bang, A.V. Balatsky, and J.D. Thompson, *Phys. Rev. Lett.* **89**, 157004 (2002).
- [21] Y.S. Kwon, J.B. Hong, Y.R. Jang, H.J. Oh, Y.Y. Song, B.H. Min, T. Lizuka, S.-I. Kimura, A.V. Balatsky, and Y. Bang, *New J. Phys.* **14**, 063009 (2012).
- [22] T. Sato, S. Souma, K. Nakayama, K. Terashima, K. Sugawara, T. Takahashi, Y. Kamihara, M. Hirano, and H. Hosono, *J. Phys. Soc. Jpn.* **77**, 063708 (2008).
- [23] D. C. Johnston, *Advances in Physics* **59**, 803 (2010).
- [24] K.K. Gomes, A.N. Pasupathy, A. Pushp, S. Ono, Y. Ando, A. Yazdani, *Nature* **447**, 569 (2007).
- [25] J. Lee, K. Fujita, A.R. Schmidt, C.K. Kim, H. Eisaki, S. Udhida, and J.C. Davis, *Science* **325**, 1099 (2009).

- [26] M.J. Lawler, K. Fujita, J. Lee, A.R. Schmidt, Y. Kohsaka, C.K. Kim, H. Eisaki, S. Uchida, J.C. Davis, J.P. Sethna, and E.-A. Kim, *Nature* **466**, 347 (2010).
- [27] T.D. Stanescu, and P. Phillips, *Phys. Rev. Lett.* **91**, 017002 (2003).
- [28] M. Yi, D.H. Lu, R. Yu, S.C. Riggs, J.-H. Chu, B. Lv, Z.K. Liu, M. Lu, Y.-T. Cui, M. Hashimoto, S.-K. Mo, Z. Hussain, C.W. Chu, I.R. Fisher, Q. Si, and Z.-X. Shen, *Phys. Rev. Lett.* **110**, 067003 (2013).
- [29] P. Pal, M.K. Dalai, R. Kundu, and B. R. Sekhar, *Phys. Rev B* **77**, 184405 (2008).
- [30] L. deMedici, S.R. Hassan, M. Capone, and X. Dai, *Phys. Rev. Lett.* **102**, 126401 (2009).
- [31] M. Neupane, P. Richard, Z.-H. Pan, Y.-M. Xu, R. Jin, D. Mandrus, X. Dai, Z. Fang, Z. Wang, and H. Ding, *Phys. Rev. Lett.* **103**, 097001 (2009).
- [32] V.I. Anisimov, I.A. Nekrasov, D.E. Kondakov, T.M. Rice, and M. Sigrist, *Eur. Phys. J. B* **25**, 191 (2002).
- [33] L. Craco, M.S. Laad, and S. Leoni, *Europhys. Lett.* **91** 27001 (2009).
- [34] M. Aichhorn, S. Biermann, T. Miyake, A. Georges, and M. Imada, *Phys. Rev. B.* **82**, 064504 (2010).
- [35] Y. Zhang, F. Chen, C. He, L.X. Yang, B.P. Xie, Y.L. Xie, X.H. Chen, M. Fang, M. Arita, K. Shimada, H. Namatame, M. Taniguchi, J.P. Hu, and D.L. Feng, *Phys. Rev. B* **82**, 165113 (2010).
- [36] P.-H. Lin, Y. Texier, A. Taleb-Ibrahimi, P. LeFèvre, F. Bertran, E. Giannini, M. Grioni, and V. Brouet, *Phys. Rev. Lett.* **111**, 217002 (2013).
- [37] V.P.S. Awana, A. Pal, A. Vajpayee, M. Mudgel, H. Kishan, M. Husain, R. Zeng, S. Yu, Y.F. Guo, Y.G. Shi, K. Yamaura, and E.T. -Muromachi, *J. Appl. Phys.* **107**, 09E128 (2010).
- [38] R.A. Zargar, A. Pal, A.K. Hafiz, and V.P.S. Awana, *J. Supercond. Nov. Magn.* **27**, 897 (2014).
- [39] M. Maniraj, and S.R. Barman, *Rev. Sci. Instrum.* **85**, 033301 (2014).

- [40] S. Banik, A.K. Shukla, and S.R. Barman, *Rev. Sci. Instrum.* **76**, 06612 (2005).
- [41] M. Maniraj, B.N. Raja Sekhar, and S.R. Barman, *Rev. Sci. Instrum.* **83**, 046107 (2012).
- [42] O.K. Andersen, *Phys. Rev. B* **12** 3060 (1975).
- [43] S. Li, C. Delacruz, Q. Huang, Y. Chen, J.W. Lynn, J. Hu, Y.-L. Huang, F.-C. Hsu, K.-W. Yeh, M.-K. Wu, and P. Dai, *Phys. Rev. B* **79**, 054503 (2009)
- [44] F.-C. Hsu, J.-Y. Luo, K.-W. Yeh, T.-K. Chen, T.-W. Huang, P.M. Wu, Y.-C. Lee, Y.-L. Huang, Y.-Y. Chu, D.-C. Yan, and M.-K. Wu, *Proc. Natl. Acad. Sci. USA* **105**, 14262 (2008).
- [45] S. Medvedev, T. M. McQueen, I. A. Troyan, T. Palasyuk, M. I. Erements, R. J. Cava, S. Naghavi, F. Casper, V. Ksenofontov, G. Wortmann, and C. Felser, *Nature Mater.* **8**, 630 (2009).
- [46] J. -F. Ge, Z. -L. Liu, C. Liu, C. -Lei Gao, D. Qian, Q. -K. Xue, Y. Liu, and J. -F. Jia, *Nature Mater.* **14**, 285 (2015).
- [47] M. Chand, G. Saraswat, A. Kamlapure, M. Mondal, S. Kumar, J. Jesudasan, V. Bagwe, L. Benfatto, V. Tripathi, P. Raychaudhuri, *Phys. Rev.* **85**, 014508 (2012)
- [48] B. Joseph, A. Iadecola, A. Puri, L. Simonelli, Y. Mizuguchi, Y. Takano, and N.L. Saini, *Phys. Rev. B* **82**, 020502(R) (2010).
- [49] Z. Wang, P. Zhang, G. Xu, L.K. Zeng, H. Miao, X. Xu, T. Qian, H. Weng, P. Richard, A. V. Fedorov, H. Ding, X. Dai, and Z. Fang, *arxiv* : 1506.0676 (2015).
- [50] Keith W. Goodman, and Victor E. Henrich *Phys. Rev. B* **49**, 4827 (1994).
- [51] T. Yokoya, R. Yoshida, Y. Utsumi, K. Tsubota, H. Okazaki, T. Wakita, Y. Mizuguchi, Y. Takano, T. Muro, Y. Kato, H. Kumigashira, M. Oshima, H. Harima, Y. Aiura, H. Sato, A. Ino, H. Namatame, M. Taniguchi, M. Hirai, and Y. Muraoka, *Sci. Technol. Adv. Mater.* **13**, 053303 (2012).
- [52] A. Yamasaki, Y. Matsui, S. Imada, K. Takase, H. Azuma, T. Muro, Y. Kato, A. Higashiya, A. Sekiyama, S. Suga, M. Yabashi, K. Tamasaku, T. Ishikawa, K. Terashima,

- H. Kobori, A. Sugimura, N. Umeyama, H. Sato, Y. Hara, N. Miyagawa, and S.I. Ikeda, *Phys. Rev. B* **82**, 184511 (2010).
- [53] N.L. Saini, Y. Wakisaka, B. Joseph, A. Iadecola, S. Dalela, P. Srivastava, E. Magnano, M. Malvestuto, Y. Mizuguchi, Y. Takano, T. Mizokawa, and K. B. Garg, *Phys. Rev. B* **83**, 052502 (2011).
- [54] Z.P. Yin, K. Haule, and G. Kotliar, *Nature Materials*. **10**, 932 (2011).
- [55] B. Joseph, A. Iadecola, L. Simonelli, Y. Mizuguchi, Y. Takano, T. Mizokawa, and N.L. Saini, *J. Phys. : Condens. Matter* **22**, 485702 (2010).
- [56] D. Louca, K. Horigane, A. Llobet, R. Arita, S. Ji, N. Katayama, S. Konbu, K. Nakamura, T.-Y. Koo, P. Tong, and K. Yamada, *Phys. Rev. B* **81**, 134524 (2010).
- [57] K. Horigane, H. Hiraka, and K. Ohoyama, *J. Phys. Soc. Jpn.* **78**, 074718 (2009).
- [58] P. Phillips, T.-P. Choy, and R.G. Leigh, *Rep. Prog. Phys.* **72**, 036501 (2009).
- [59] E. Ieki, K. Nakayama, Y. Miyata, T. Sato, H. Miao, N. Xu, X.-P. Wang, P. Zhang, T. Qian, P. Richard, Z.-J. Xu, J.S. Wen, G.D. Gu, H.Q. Luo, H.-H. Wen, H. Ding, and T. Takahashi, *Phys. Rev. B* **89** 140506 (2014).
- [60] Z.K. Liu, R.-H. He, D.H. Lu, M. Yi, Y.L. Chen, M. Hashimoto, R.G. Moore, S.-K. Mo, E.A. Nowadnick, J. Hu, T.J. Liu, Z.Q. Mao, T.P. Devereaux, Z. Hussain, and Z.-X. Shen, *Phys. Rev. Lett.* **110**, 037003 (2013).
- [61] L.Simonelli, N.L. Saini, Y. Mizuguchi, Y. Takano, T. Mizokawa, G. Baldi, and G. Monaco, *J. Phys. : Condens. Matter* **24**, 415501 (2012).
- [62] K. Shimada, T. Mizokawa, K. Mamiya, T. Saitoh, A. Fujimori, K. Ono, A. Kakizaki, T. Ishii, M. Shirai, and T. Kamimura, *Phys. Rev. B* **57**, 8845 (1998).
- [63] C.L. Chen, C.L. Dong, J.L. Chen, J.-H. Guo, W.L. Yang, C.C. Hsu, K.W. Yeh, T.W. Huang, B.H. Mok, T.S. chan, J.F. Lee, C.L. Chang, S.M. Rao, and M.K. Wu, *Phys. Chem. Chem. Phys* **13**, 15666 (2011).

Chapter 4

Electronic structure study of Nd[O_{1-x}F_x]FeAs superconductor

In the previous chapter, we discussed about the electronic structure of FeSe_{1-x}Te_x superconductor, a member of (11) family using Photoemission and Inverse Photoemission Spectroscopy. This chapter covers the electronic structure study of Nd[O_{1-x}F_x]FeAs, a member of (1111) family. The similarity in the electronic structure of (1111) and (11) family, despite the structural difference due to the absence of spacer layer in case of (11) family has been explored.

4.1 Introduction

The discovery of superconductivity with T_c of ~ 26 K, in fluorine doped LaFeAsO [1], created a new arena of research in the field of superconductors and paved way for the discovery of various Fe superconductors. Amongst the various classes of layered Fe superconductors, the (1111) family comprising of the layered oxy-pnictides exhibit the highest T_c . Till date various rare earth (RE) doped quaternary oxypnictides superconductors [2] with the general formula REFeAsO have attracted the attention of researchers. Electron doping via partial replacement of O²⁻ with F⁻ or oxygen deficiency in these systems enhances the T_c [3–8] to a maximum of 55 K [9]. The Fe oxypnictides possess striking resemblances to the cuprates in terms of structure and high T_c . This has led to an avalanche of research in this field.

The Rare Earth oxypnictides (REFeAsO) exist in layered structure, with the superconducting (FeAs) ^{δ^-} layers separated by the charge reservoir (REO) ^{δ^+} layers. The superconductivity in these systems are dependent on the charge transfer and the lattice misfit between the two sub layers [10, 11]. One of the interesting aspects of these materials is the competing spin density wave (SDW) and the superconductivity [12, 13]. The undoped compound REFeAsO is

non superconducting and exhibits a structural phase transition from tetragonal to orthorhombic which is accompanied by a spin density wave (SDW) transition [12–17]. Doping or oxygen deficiency lead to disappearance of structural and SDW transition with a simultaneous emergence of superconductivity. The maximum T_c of the doped system increases with reducing the rare-earth ion size [18], while the structural transition temperature decreases for the undoped system [12, 14]. Although doping suppresses both the lattice distortion and Fe magnetic order, magnetism is believed to play a major role in the superconducting pairing mechanism in pnictide superconductors. This suggests a strong interplay between structure, magnetism and superconductivity with the chemical pressure in the Fe pnictides.

Extensive research have been focussed on unveiling the electronic structure of Fe pnictides. The first principles band structure calculations indicated that the Fermi surface of REFeAsO consists of two hole pockets around Γ point and two electron pockets around M point [19]. The theoretical calculations and quantum oscillation measurements [20] suggest similar sizes of the hole and electron pockets at the Fermi surface. On the contrary, ARPES shows an extra large circular hole pocket around the zone centre, Γ , which covers almost 40 % of the Brillouin zone intersection size. This extra hole pocket is associated with the surface-driven electronic structure, i.e an atomic reorganisation and/or lattice relaxation at the sample surface [21–23]. This large hole pocket shows no gap in the undoped sample, while exhibits a s-wavelike gap in the F doped superconducting sample [24]. Various scenarios have been proposed to explain the mechanism of superconductivity in these systems predicting different symmetry of the order parameter ranging from s wave to d wave and p wave [25–30].

The layered oxypnictides with unpaired 4f electrons show some interesting interactions of the rare earth magnetic moment with the FeAs layer [31]. The competing effects of the rare earth magnetic moments and the chemical pressure (due to doping) on the electronic, magnetic and superconducting properties of REFeASO family are still not well understood. The Nd based oxypnictide (NdFeAsO), shows a high T_c of ~ 50 K with F doping. The parent compound, NdFeAsO is an antiferromagnetic, nonsuperconductor displaying a structural transition from tetragonal to orthorhombic at 150 K which is accompanied by the onset of stripe like AFM ordering of Fe below $T_N \sim 140$ K [32]. Below temperature 15 K, the Fe moments experience a strongly hysteretic magnetic transition from AFM to FM along the c direction but unchanged AFM stripe like ordering in the ab plane. Accompanied with this, the Nd moments order antiferromagnetically at ~ 6 K. The Nd moments are coupled to the Fe moment by a com-

mon magnetic unit cell, indicating a complex interplay between Nd and Fe magnetism [33]. F doping at O site, causes an emergence of superconductivity with maximum T_c reaching 50 K, by suppressing the spin density wave order [34]. The pnictogen/chalcogen height dependent multiorbital correlations of Fe-3d orbitals give rise to exotic electronic properties Fe superconductors [35].

Previously reported Angle Resolved Photoemission studies on Nd[O_{1-x}F_x]FeAs single crystals have looked into the superconducting gap and the nature of Fermi surface [24, 36]. ARPES study on NdFeAsO_{0.9}F_{0.1} [36] revealed the Fermi surface composed of large hole pockets at Brillouin zone (BZ) centre and smaller electron pockets at each corner of the BZ. Further a superconducting gap of 20 meV, with an emergence of a coherent peak below T_c was also reported. The study of Kondo et al. [24] indicated a nodeless superconducting gap in the hole pocket at BZ centre of NdFeAsO_{0.9}F_{0.1}. The isotropic superconducting gap of ~ 15 meV is consistent with an isotropic s wave pairing symmetry. In the present study, angle integrated photoemission spectroscopy has been used to investigate the electronic structure of Nd[O_{1-x}F_x]FeAs ($x = 0.0$ and 0.2). We have focussed on the emergence and origin of normal state pseudogap in these Nd pnictides, which is a characteristic feature of the pnictide superconductors [37–41]. The observed temperature dependent pseudogap has been correlated with the change in pnictogen height.

4.2 Experimental

Polycrystalline samples of Nd[O_{1-x}F_x]FeAs ($x = 0, 0.8$) used in this study were synthesized via solid state reaction route [42] and characterized for their electrical, magnetic and structural properties. Angle integrated ultraviolet photoemission spectroscopy (UPS) measurements were performed using a high intensity vacuum-ultraviolet source and a hemispherical electron energy analyser (SCIENIA R3000). At the He I ($h\nu = 21.2$ eV) line, the photon flux was of the order of 10^{16} photons/s/steradian with a beam spot of 2 mm in diameter. Fermi energies for all measurements were calibrated by using a freshly evaporated Ag film on to the sample holder. The total energy resolution, estimated from the width of the Fermi edge, was about 27 meV for the He I excitation. All the measurements were performed at a base pressure of $\sim 5.0 \times 10^{-11}$ mbar. The samples were repeatedly scraped using a diamond file inside the preparation chamber with a base vacuum of 5.0×10^{-10} mbar and the spectra were taken within an hour,

so as to avoid any surface degradation. All the measurements were repeated many times to ensure the reproducibility of the spectra. The low temperature measurements at 77 K were performed immediately after cleaning the sample surfaces followed by the room temperature measurements. Band structure calculations using TBLMTO-ASA [43] were performed using the experimental lattice parameters reported earlier [42]. The correlation effects of the Fe-3d and Nd-4f orbitals were taken into account by using the LDA + U formalism with J as 0.8 eV and U as 3 eV for Fe-3d and 5.0 eV for Nd-4f [44].

4.3 Results and Discussions

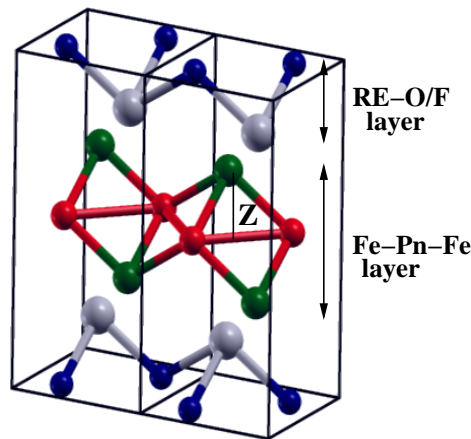


Figure 4.1: Crystal structure of REFePnO depicting two unit cells. Grey, blue, red and green spheres correspond to RE, O/F, Fe and Pn atoms, respectively.

The prototypical crystal structure of Fe(1111) superconductor is depicted in fig 4.1. It consists of alternate stacks of Fe-Pn-Fe (Pn = Pnictogen) and RE-O/F (RE = Rare Earth) layers with eight atoms in a tetragonal unit cell of space group $P4/nmm$. The intralayer and interlayer chemical bonding is of covalent and ionic nature respectively [45]. The perpendicular distance between Fe plane and the Pn atom is termed as the pnictogen height 'z'. The structure of Fe (1111) family differs from the previously discussed (11) family in terms of the presence of the spacer layer, RE-O/F. The RE-O layers are negatively charged and acts as charge reservoir while the Fe-As layer is negatively charged conducting layer responsible for superconductivity. The structure of REFeAsO comprises of sheets of Fe^{2+} ions in between the ionic blocks of $REOAs^{2-}$. The RE atoms are coordinated by four As atoms and four O atoms forming distorted square antiprisms. The Fe atoms form square nets perpendicular to the c- axis. F substitution

introduces extra positive charges in the RE-O layers and hence compensating electrons are introduced into the Fe-As layers to maintain charge neutrality. The increased interlayer ionic bonding due to F doping manifests itself in the shortening of the lattice vector along the c axis. In case of NdFeAsO, the RE and Pn correspond to Nd and As atoms, respectively.

The lattice parameters for the parent, NdFeAsO is $a = 3.969 \text{ \AA}$, $c = 8.596 \text{ \AA}$. For NdFeAsO_{0.8}F_{0.2}, the a and c lattice parameters are reduced to $a = 3.956 \text{ \AA}$, $c = 8.539 \text{ \AA}$ [42]. The pnictogen height 'z' depends on the internal coordinate of the pnictogen atom (d) and the c-axis lattice constant according to the relation; $z = (d-0.5) \times c$. The internal coordinates of the pnictogen atom for NdFeAsO and NdFeAsO_{0.8}F_{0.2} are 0.6577 and 0.6514 \AA , respectively [42]. The pnictogen heights estimated using the above relation are 1.36 and 1.29 \AA for the parent and doped compound respectively. Fluorine doping also changes the As-Fe-As bond angle (α) in REFeAsO compounds. The bond angle decreases approaching the value of ideal tetrahedron angle of 109.5° [12]. Fluorine doping thus, causes a reduction in pnictogen height and bond angle, both of which are determinant to superconductivity in pnictides.

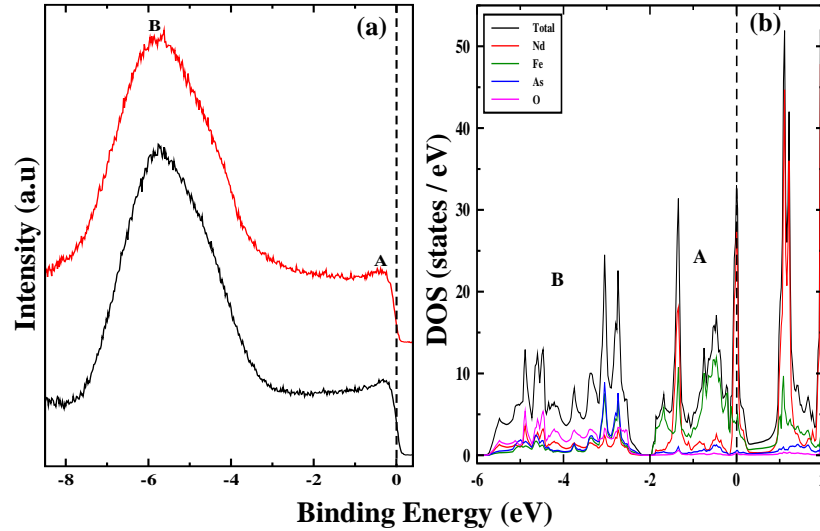


Figure 4.2: (a) He II Valence band photoemission spectra for NdFeAsO (black) and NdFeAsO_{0.8}F_{0.2} (red) showing two major features A and B. (b) The density of states calculation for NdFeAsO with the marked positions A and B corresponding to the experimental features.

Panel (a) of fig 4.2 shows the He II valence band photoemission spectra for the NdFeAsO_{1-x}F_x ($x = 0, 0.2$) samples taken at room temperature. Panel (b) shows our theoretical band structure calculations for NdFeAsO using TB-LMTO ASA depicting the valence band density of states (DOS) in the energy range -6 - +2 eV . The experimental spectra shows two prominent fea-

tures A and B at -0.2 and -5.7 eV energy. It can be inferred from the DOS calculations that A is predominantly Fe derived states with an admixture of localised Nd states while B consists of As - O hybridized states. For the doped compound (calculation not shown) F states also contribute to feature B. The localised Nd 4f states are split into two bands at ~ -1.5 eV and at E_F . The conduction band, from E_F till 2 eV, comprises of Nd-Fe hybridised states. The DOS plot shows a dip at 0.3 eV above E_F extending till 0.9 eV which is a generic case for the members of (1111) family [35]. This dip like structure above E_F , absent in case of (11) family, is attributed to the higher chalcogen height by Miyake et al. [35]. The relatively lower pnictogen height ($z = 1.35$ Å) in NdFeAs(O,F) [46], in comparison to the Fe(Se,Te) system ($z = 1.78$ Å for FeTe and 1.46 Å for FeSe) [35], promotes the Fe-3d - pnictogen-p hybridisation and Fe-3d inter orbital hoppings via As-p orbitals. This causes an enhanced hybridisation of $x^2-y^2 - 3z^2-r^2$ and $yz/zx - xy$ orbitals, and thereby a larger splitting between lower and upper Fe 3d bands. Hence, a dip emerges in (1111) family in sharp contrast to the (11) family. Our calculations are in accordance with the earlier reported band structure calculations [35] of Fe(1111) family of superconductors.

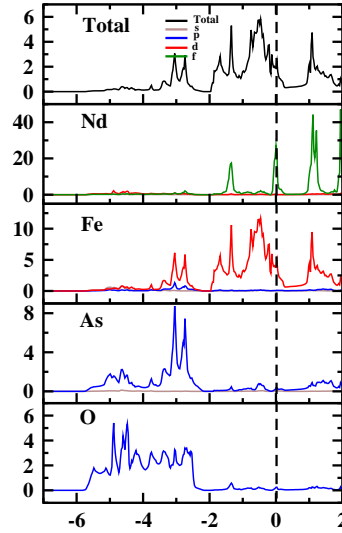


Figure 4.3: Calculated partial density of states of NdFeAsO.

The partial density of states (PDOS) calculation for NdFeAsO, shown in fig 4.3 shows two prominent features A and B. The feature A extending from E_F till -2.0 eV, comprises of primarily Fe-3d states with an admixture of highly localised Nd-4f states. The feature B spanning from -2.5 to -6 eV originates from the As-4p - O-2p hybridised states with a minor contribution from Fe-3d states towards the lower binding energy side. The conduction band

extending from E_F to 2 eV comprises of Fe- 3d and Nd-4f states.

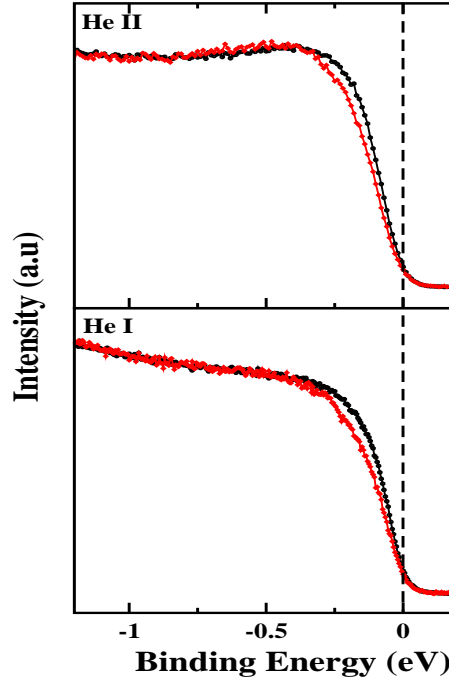


Figure 4.4: The high resolution photoemission spectra for NdFeAsO (black) and NdFeAsO_{0.8}F_{0.2} (red) using He I (bottom panel) and He II (top panel) energy.

Figure 4.4 shows the near E_F photoemission spectra of the NdFeAsO_{1-x}F_x ($x = 0.0, 0.2$) samples taken using He I (21.2 eV) and He II (40.8 eV) sources. The parent compound exhibits a feature at -0.2 eV for both He I and He II sources. However, the higher intensity of this feature in case of He II signifies the higher Fe 3d cross section at He II energy. For the doped compound, this feature shifts to higher binding energy and occurs at -0.30 eV. Electron doping due to fluorine substitution at the oxygen site causes a shift in the Fermi level which in turn results in the backward shift of bands from the Fermi level [47]. The pnictogen height, plays a crucial role in the observed electronic properties of the Fe superconductors [35, 48]. Doping or application of pressure causes modification in the pnictogen height [46]. Electron doping, due to F substitution in NdFeAsO leads to reduced c-axis lattice constant [42] and thereby a reduced pnictogen height (z) (as was estimated from the relation between c-axis lattice parameter and pnictogen atom positions in the previous paragraph), similar to that observed in other Fe pnictides [49]. The change in the structural geometry of Fe-As tetrahedra due to the reduced z promotes the hybridisation of Fe-3d - As-4p orbitals and Fe 3d inter orbital hoppings. The enhanced hybridisation between Fe-3d $x^2-y^2 - 3z^2-r^2$ and $yz/zx - xy$ orbitals at lower z enhances the splitting between the lower and upper Fe-3d bands situated in valence and conduction bands

respectively [35]. This is reflected as the backward shift of Fe-3d states at the Fermi level in comparison to the undoped sample.

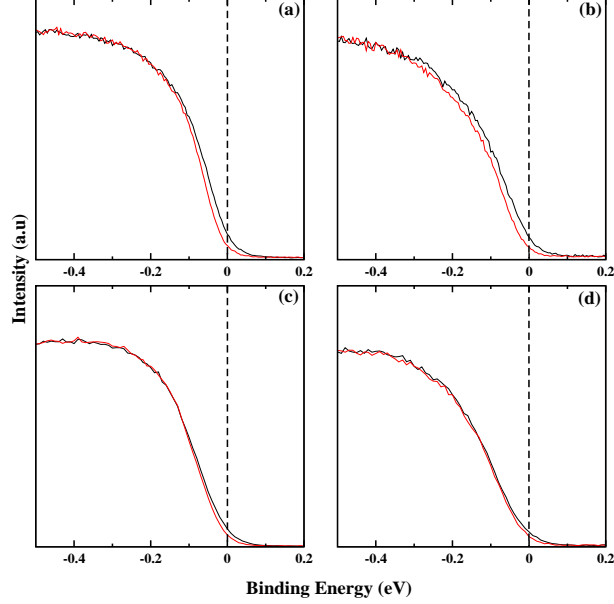


Figure 4.5: The high resolution photoemission spectra at 300 K (black) and 77 K (red) using He I (21.2 eV) source for (a) NdFeAsO (b) NdFeAsO_{0.8}F_{0.2}. The He II (40.8 eV) photoemission spectra at 300 K (black) and 77 K (red) for (c) NdFeAsO and (d) NdFeAsO_{0.8}F_{0.2}.

Figure 4.5(a,b) shows the He I near E_F valence band spectra for NdFeAsO and NdFeAsO_{0.8}F_{0.2} at 300 K (black) and 77 K (red) respectively. One can clearly see a depletion of states from the neighborhood of E_F as we go down in temperature. Such reduced spectral weight near the E_F shows the formation of a pseudogap. The He II spectra (fig 4.5(c,d)) also show a similar pseudogap opening although the magnitude of the gap is lesser. The temperature dependent photoemission studies on Fe(Se,Te) systems also displayed a pseudogap of lower magnitude at He II energy. Photoemission measurements on various REFeASO systems [37, 38, 40], have demonstrated the existence of normal state pseudogap, though its origin is not clear. The temperature dependent pseudogap formation in Fe(Se,Te) was ascribed to the reduction in chalcogen height at low temperature which resulted in enhancement of Fe-3d interorbital hoppings. However, reports by Ingle et al. [49] demonstrated that the lowering of temperature leads to an increase in the pnictogen height, for SmFeAsO. Hence, the temperature dependent pseudogap observed here in the case of NdFeAsO cannot be correlated with the pnictogen height. Theoretical studies on REFeAsO system by León et al. [50] and Dong et al. [17] have indicated a Fe 3d spectral weight depletion near E_F in the low temperature orthorhombic phase. This was linked to the existence of stripe spin ordering in the orthorhombic phase. The presence of spin

density wave (SDW) in NdFeAsO has been confirmed by Awana et al. [42] from resistivity measurements. Thus, the origin of pseudogap formation observed in case of NdFeAsO can be attributed to the SDW existing in the low temperature orthorhombic phase.

The F doped compound, however does not show any structural or magnetic transition. On the contrary, F doped REFeAsO compound exhibits a reduction in pnictogen height at low temperature as reported by Ingle et al. [49]. Thus, the pseudogap at low temperature in NdFeAsO_{0.8}F_{0.2} can be correlated with the reduced pnictogen height, similar to that observed in Fe(Se,Te) systems. The reduced pnictogen height promotes the Fe-3d - As-4p hybridisation and Fe-3d interorbital hoppings mediated via pnictogen orbitals. This results in an enhanced hybridisation of $x^2-y^2 - 3z^2-r^2$ and $yz/zx - xy$ orbitals, and hence, a reduced spectral weight for Fe-3d x^2-y^2 and yz/zx orbitals near Fermi level [35]. Thus, the pnictogen height mediated enhanced Fe-3d interorbital hybridisation is the cause of emergence of pseudogap in doped pnictides. Further, this temperature induced change in the structure of the F doped compound can also lead to an Orbital Selective Mott insulating Phase (OSMP) (at low temperature) whereby, the Fe-3d (x^2-y^2 and yz/zx) orbitals which were metallic are rendered insulating, as was discussed in Fe(Se,Te) system.

Thus, the formation of pseudogap in parent and doped compound have a different origin. In the case of parent compound it is linked to the SDW whereas for the doped compound its origin lies in the pnictogen height dependent moderate multi orbital electron correlations. This suggest a strong interplay of magnetism and electron correlations linked to the normal state pseudogap, in the family of REFeAsO system. Despite the lower electron correlation value of Fe-3d orbitals in the (1111) family ($U \sim 3$ eV) in comparison to the (11) family ($U \sim 4$ eV), due to the lower z and presence of shallower Nd-4f and O-2p states, the temperature dependent pseudogap follow the same trend in both the families of Fe superconductors. This hints at the common origin of superconductivity and correlations in both the families.

4.4 Conclusion

In conclusion, we have studied the doping and temperature dependent valence band electronic structure of Nd[O_{1-x}F_x]FeAs systems. The electronic structure of Fe superconductors belonging to (11) and (1111) family exhibit a remarkable similiarity, despite the difference in the structure, in terms of the absence of spacer layer in (11) system. The observed tempera-

ture dependent pseudogap in the parent compound is attributed to the spin density wave. On the other hand, the pseudogap formation in the doped compound has been correlated with the enhanced Fe-3d interorbital hybridisation induced by the reduced pnictogen height at low temperature. This observed spectral weight depletion and consequent pseudogap, for doped compounds show a similar nature to that found in the (11) family of superconductor, demonstrating the role of multiorbital correlations in the family of Fe superconductors. Further, since the pseudogap is linked to the temperature dependent structural changes, it could be intimately related to the Orbital Selective Mottness of x^2-y^2 and yz/zx orbitals similar to the case of (11) system. The different origin of pseudogap formation in the parent (linked to SDW) and doped compound (linked to pnictogen height), signifies the intricate interplay of magnetism and multiorbital correlations in the (1111) family of Fe superconductors.

Bibliography

- [1] Y. Kamihara, T. Watanabe, M. Hirano, and H. Hosono, *J. Am. Chem. Soc.* **130**, 3296 (2008).
- [2] P. Quebe, L. J. Terbüchte, and W. Jeitschko, *J. Alloys Compd.* **302**, 70 (2000).
- [3] H. Takahashi, K. Igawa, K. Arii, Y. Kamihara, M. Hirano, and H. Hosono, *Nature (London)* **453**, 376 (2008).
- [4] Z. -A. Ren, G. -C. Che, X. -L. Dong, J. Yang, W. Lu, W. Yi, X. -L. Shen, Z. -C. Li, L. -L. Sun, F. Zhou, and Z. -X. Zhao *Europhys. Lett.* **83**, 17002 (2008).
- [5] G. F. Chen, Z. Li, D. Wu, G. Li, W. Z. Hu, J. Dong, P. Zheng, J. J. Luo, and N. L. Wang, *Phys. Rev. Lett.* **100**, 247002 (2008).
- [6] Z. -A. Ren, J. Yang, W. Lu, W. Yi, G. -C. Che, X. -L. Dong, L. -L. Sun, and Z. -X. Zhao, *Mater. Res. Innovations* **12**, 105 (2008).
- [7] Z. -A. Ren, J. Yang, W. Lu, W. Yi, X. -L. Shen, Z. -C. Li, G. -C. Che, X. -L. Dong, L. -L. Sun, F. Zhou, and Z. X. Zhao, *Europhys. Lett.* **82**, 57002 (2008).
- [8] P. Cheng, L. Fang, H. Yang, X. Zhu, G. Mu, H. Luo, Z. Wang, and H. Wen, *Sci. China Ser. G* **51** 719 (2008).
- [9] R. Z. -An, L. Wei, Y. Jie, Y. Wei, S. X. -Li, Z. -C., C. G. -Can, D. X. -Li, S. L. -Ling, Z. Fang, and Z. Z. -Xian, *Chin. Phys. Lett.* **25**, 2215 (2008).
- [10] M. Fratini, R. Caivano, A. Puri, A. Ricci, Z. Ren, X. Dong, J. Yang, W. Lu, Z. -X. Zhao, L. Barba, G. Arrighetti, M. Polentarutti, and A. Bianconi, *Supercond. Sci. Technol.* **21**, 092002 (2008).

- [11] A. Ricci, N. Poccia, G. Ciasca, M. Fratini, A. Bianconi, J. Supercond. Nov. Magn. **22**, 589 (2009).
- [12] J. Zhao, Q. Huang, C. de la Cruz, S. Li, J. W. Lynn, Y. Chen, M. A. Green, G. F. Chen, G. Li, Z. Li, J. L. Luo, N. L. Wang, and P. Dai, Nature Materials **7**, 953 (2008).
- [13] Q. Huang, J. Zhao, J. W. Lynn, G. F. Chen, J. L. Luo, N. L. Wang, and P. Dai, Phys. Rev. B **78**, 054529 (2008).
- [14] C. de la Cruz, Q. Huang, J. W. Lynn, Jiying Li, W. Ratcliff II, J. L. Zarestky, H. A. Mook, G. F. Chen, J. L. Luo, N. L. Wang, and P. Dai, Nature **453**, 899 (2008).
- [15] C. -H. Lee, A. Iyo, H. Eisaki, H. Kito, M. Teresa Fernandez-Diaz, T. Ito¹, K. Kihou, H. Matsuhata, M. Braden, and K. Yamada, J. Phys. Soc. Jpn. **77**, 083704 (2008).
- [16] F. Ma, Z. -Yi Lu, Phys. Rev. B **78** 033111 (2008).
- [17] J. Dong, H. J. Zhang, G. Xu, Z. Li, G. Li, W. Z. Hu, D. Wu, G. F. Chen, X. Dai, J. L. Luo, Z. Fang, and N. L. Wang, Europhys. Lett. **83**, 27006 (2008).
- [18] P. M. Aswathy, J. B. Anooja, P. M. Sarun and U. Syamaprasad, Supercond. Sci. Technol. **23**, 073001 (2010).
- [19] S. Raghu, X. -L. Qi, C. -X. Liu, D. J. Scalapino, and S. -C. Zhang, Phys. Rev. B **77**, 220503 (2008).
- [20] A. I. Coldea, J. D. Fletcher, A. Carrington, J. G. Analytis, A. F. Bangura, J. -H. Chu, A. S. Erickson, I. R. Fisher, N. E. Hussey, and R. D. McDonald, Phys. Rev. Lett. **101**, 216402 (2008).
- [21] D. H. Lu, M. Yi, S.-K. Mo, J. G. Analytis, J.-H. Chu, A. S. Erickson, D. J. Singh, Z. Hussain, T. H. Geballe, I. R. Fisher, and Z.-X. Shen, Physica C **469**, 452 (2009).
- [22] I. I. Mazin and J. Schmalian, Physica C **469**, 614 (2009).
- [23] H. Eschrig, A. Lankau, and K. Koepf, Phys. Rev. B **81**, 155447 (2010).
- [24] T. Kondo, A. F. S. -Syrro, O. Copie, C. Liu, M. E. Tillman, E. D. Mun, J. Schmalian, S. L. Bud'ko, M. A. Tanatar, P. C. Canfield, and A. Kaminski, Phys. Rev. Lett **101**, 147003 (2008).

- [25] I. I. Mazin, D. J. Singh, M. D. Johannes, and M. H. Du, Phys. Rev. Lett. **101**, 057003 (2008)
- [26] K. Kuroki, S. Onari, R. Arita, H. Usui, Y. Tanaka, H. Kontani, and H. Aoki, Phys. Rev. Lett. **101**, 087004 (2008).
- [27] X. Dai, Z. Fang, Y. Zhou, and F. -C. Zhang, Phys. Rev. Lett. **101**, 057008 (2008).
- [28] P. A. Lee, and X. -G. Wen, Phys. Rev. B **78**, 144517 (2008).
- [29] Z. -J. Yao, J. -X. Li, and Z. D. Wang, New J. Phys. **11**, 025009 (2009).
- [30] F. Wang, H. Zhai, Y. Ran, A. Vishwanath, and D. -H. Lee, Phys. Rev. Lett. **102**, 047005 (2009).
- [31] P. Jeglič, J. -W. G. Bos, A. Zorko, M. Brunelli, K. Koch, H. Rosner, S. Margadonna, and D. Arčon, Phys. Rev. B **79**, 094515 (2009).
- [32] Y. Chen, J. W. Lynn, J. Li, G. Li, G. F. Chen, J. L. Luo, N. L. Wang, P. Dai, C. dela Cruz, and H. A. Mook, Phys. Rev. B **78**, 064515 (2008).
- [33] W. Tian, W. Ratcliff II, M. G. Kim, J. -Q. Yan, P. A. Kienzle, Q. Huang, B. Jensen, K. W. Dennis, R. W. McCallum, T. A. Lograsso, R. J. McQueeney, A. I. Goldman, J. W. Lynn, and A. Kreyssig, Phys. Rev. B **82**, 060514 (2010).
- [34] Y. Qiu, W. Bao, Q. Huang, T. Yildirim, J. M. Simmons, M. A. Green, J. W. Lynn, Y. C. Gasparovic, J. Li, T. Wu, and X. H. Chen, Phys. Rev. Lett. **101**, 257002 (2008).
- [35] T. Miyake, K. Nakamura, R. Arita, and M. Imada, J. Phys. Soc. Jpn. **79**, 044705 (2010).
- [36] C. Liu, T. Kondo, M. E. Tillman, R. Gordon, G. D. Samolyuk, Y. Lee, C. Martin, J. L. McChesney, S. Bud'ko, M. A. Tanatar, E. Rotenberg, P. C. Canfield, R. Prozorov, B. N. Harmon, and A. Kaminski, arXiv:0806.2147 (2008).
- [37] X. Jia, H. Liu, W. Zhang, L. Zhao, J. Meng, G. Liu, X. Dong, G. F. Chen, J. L. Luo, N. L. Wang, Z. A. Ren, W. Yi, J. Yang, W. Lu, G. C. Che, G. Wu, R. H. Liu, X. H. Chen, G. Wang, Y. Zhou, Y. Zhu, X. Wang, Z. Zhao, Z. Xu, C. Chen, and X. J. Zhou, arXiv: 0806.0291 (2008).

- [38] H. W. Ou, Y. Zhang, J. F. Zhao, J. Wei, D. W. Shen, B. Zhou, L. X. Yang, F. Chen, M. Xu, C. He, R. H. Liu, M. Arita, K. Shimada, H. Namatame, M. Taniguchi, Y. Chen, X. H. Chen, and D. L. Feng, arXiv:0806.0078 (2008).
- [39] T. Shimojima, T. Sonobe, W. Malaeb, K. Shinada, A. Chainani, S. Shin, T. Yoshida, S. Ideta, A. Fujimori, H. Kumigashira, K. Ono, Y. Nakashima, H. Anzai, M. Arita, A. Ino, H. Namatame, M. Taniguchi, S. Uchida, Y. Tomioka, T. Ito, K. Kihou, C. H. Lee, A. Iyo, H. Eisaki, K. Ohgushi, S. Kasahara, T. Terashima, H. Ikeda, T. Shibauchi, Y. Matsuda, and K. Ishizaka, *Phys. Rev. B* **89**, 045101 (2014).
- [40] Y. Ishida, T. Shimojima, K. Ishizaka, T. Kiss, M. Okawa, T. Togashi, S. Watanabe, X. Wang, C. Chen, Y. Kamihara, M. Hirano, H. Hosono, and S. Shin, *J. Phys. Jpn.* **77**, 61 (2008).
- [41] T. Sato, S. Souma, K. Nakayama, K. Terashima, K. Sugawara, T. Takahashi, Y. Kamihara, M. Hirano, and H. Hosono, arXiv: 0805.3001 (2008).
- [42] V. P. S. Awana, R. S. Meena, A. Pal, A. Pal, A. Vajpayee, K. V. R. Rao and H. Kishan, *Eur. Phys. J. B* **79**, 139 (2011).
- [43] O. K. Anderson, *Phys. Rev. B* **12**, 3060 (1975).
- [44] E. Ertürk, T. Gürel, A. V. Lukoyanov, G. Akcay, R. Eryigit, and V. I. Anisimov, *J. Phys.: Condens. Matter* **26**, 045501 (2014).
- [45] S. Lebégue, *Phys. Rev B* **75**, 035110 (2007).
- [46] K. Kuroki, H. Usui, S. Onari, R. Arita, and H. Aoki, *Phys. Rev. B* **79**, 224511 (2009).
- [47] S. L. Skornyakov, I. R. Shein, A. L. Ivanovskii, and V. I. Anisimov, *JETP Letters* **98**, 373 (2013).
- [48] V. Vildosola, L. Pourovskii, R. Arita, S. Biermann, and A. Georges, *Phys. Rev. B* **78**, 064518 (2008).
- [49] K. Ingle, K. R. Priolkar, A. Pal, V. P. S Awana, and S. Emura, *Supercond. Sci. Technol.* **27**, 075010 (2014).

[50] J. M. León, J. L. -Pacheco, A. Bianconi, and N. L. Saini, *Journal of Phys. Chem. Solids* **71**, 1118 (2010).

Chapter 5

Electronic structure of rare-earth doped SrFBiS₂ superconductors

Chapter 3 and 4 discussed about the electronic structure of Fe superconductors. In the present chapter, the photoemission spectroscopy in conjunction with LDA band structure calculations have been used to investigate the electronic structure of recently discovered BiS based superconductors. The change in band structure and electronic properties of the SrFBiS₂ superconductor with Rare Earth (Ce,La) has been presented in this chapter. A comparison of the BiS superconductor with cuprates and Fe superconductors has also been highlighted.

5.1 Introduction

Discovery of superconductivity in Bi₄O₄S₃ [1] has brought the family of BiS₂ based compounds to the focus owing to their similarities with the cuprates and Fe based superconductors in terms of quasi two dimensional layered structure. Recently, numerous superconductors have been added to this family which includes, REO_{1-x}F_xBiS₂ (RE = La, Nd, Ce, Pr, Yb) [2–7], Sr_{1-x}RE_xFBiS₂ (RE = La,Ce, Nd, Pr, Sm) [8–11], La_{1-x}M_xOBiS₂ (M = Ti, Zr, Hf and Th) [12], Eu based BiS₂ compounds [13, 14]. Till date the highest T_c reported in this family is 10.6 K exhibited by LaO_{0.5}F_{0.5}BiS₂ [2]. The BiS₂ compounds exhibit a layered structure composed of stacks of spacer layers and BiS₂ layers [1]. The BiS₂ layers have a strong bearing on many of the superconducting properties, similar to the case of the CuO layers in cuprates and Fe-P/Ch (P-pnictogen, Ch-chalcogen) layers in Fe superconductors. Parent compounds of the BiS₂ family are weak insulators or semiconductors with band gap of ~ 0.8 eV and superconductivity is induced by electron doping in the BiS₂ layers. T_c reaches a maximum at an optimum doping level of $x \sim 0.5$ for many compounds [15].

The mechanism of superconductivity in these class of materials is still under intense debate as recent experimental and theoretical findings have led to diverse views. A group of researchers [16–19] predicted the existence of a strong electron phonon interaction as a result of Fermi surface (FS) nesting, and thus proposed a s-wave superconductivity. The experimental results from magnetic penetration depth, muon spin rotation spectroscopy and ARPES also support a conventional s wave BCS superconductor mediated by electron phonon coupling [20–22]. On the other hand, it was pointed out by a few others [23, 24] that spin and orbital fluctuations emerging from the FS nesting in combination with electron correlation, may lead to unconventional pairing symmetry [23, 24]. Further, the absence of any phonon anomaly in the data from neutron scattering experiment [25], conform to a weaker electron phonon coupling against the theoretical predictions. The ratio of $\frac{2\Delta}{k_B T_c}$ estimated from scanning tunneling spectroscopy measurements [26, 27] is larger than the value expected for a conventional superconductor, thus suggesting unconventional superconductivity. ARPES measurements [15] substantiated small Fermi pockets and an anomalous temperature dependence of the low energy spectral function indicative of a strong correlation-induced unconventional superconductivity. The pairing symmetry is also highly debatable. Spin/charge fluctuation mediated pairing interactions have been studied theoretically and an extended s or d wave pairing by Martin et al. [23] and d or p wave pairing by Tao et al. [28] have been proposed. At low electron doping, the existence of g wave symmetry and at higher doping a competing s and d wave is theoretically predicted [24]. Further, Dai et al. [29] showed that the low electron doping phase is a mixture of singlets and triplets, with dominating triplet pairing symmetry. The possibility of triplet pairing and weak topological superconductivity has also been suggested [30].

Electron spectroscopic methods are considered to be quite suited to probe the electronic structure of materials. There exist very few reports probing the valence band electronic structure of BiS superconductors. ARPES study on Nd(O,F)BiS₂ [15] revealed two small electron pockets around X point instead of the large hole like Fermi surfaces at Γ and M points as per theoretical predictions. The near E_F spectrum is composed of a weakly dispersing broad hump, which is suppressed with increasing temperature, and a dispersive branch which remains unaffected with temperature. The soft X-ray photoemission spectroscopy reported by Nagira et al. [31] demonstrated the core levels as well as valence band of LaO_{1-x}F_xBiS₂. The valence band spectra indicated a shift towards higher binding energy with a simultaneous appearance of new states with dominant Bi 6p character near E_F , with F doping. The detailed

electronic structure of Rare Earth (RE) doped SrFBiS₂ superconductors is also lacking, hence, we have investigated the electronic structure of the RE doped BiS superconductors. In this chapter, we present our valence band photoemission studies on SrFBiS₂, Sr_{0.5}La_{0.5}FBiS₂ and Sr_{0.5}Ce_{0.5}FBiS₂. LDA based band structure calculations are employed to understand the experimental results. The effect of Rare Earth (La,Ce) doping on the near Fermi level electronic structure of SrFBiS₂ has been investigated.

5.2 Experimental

Polycrystalline samples of SrFBiS₂, Sr_{0.5}La_{0.5}FBiS₂, Sr_{0.5}Ce_{0.5}FBiS₂ were synthesized via solid state reaction route, characterized using various techniques and reported elsewhere [8, 32, 33]. Angle integrated ultraviolet photoemission (UPS) measurements were performed by using an ultra high vacuum system equipped with a high intensity vacuum-ultraviolet source and a hemispherical electron energy analyser (SCIENZA R3000). At the He I ($h\nu = 21.2$ eV) line, the photon flux was of the order of 10^{16} photons/s/steradian with a beam spot of 2 mm diameter. Fermi energies for all measurements were calibrated by using a freshly evaporated Ag film on a sample holder. The total energy resolution, estimated from the width of the Fermi edge, was about 27 meV for the He I excitation. All the photoemission measurements were performed at a base pressure of $\sim 5.0 \times 10^{-11}$ mbar. The samples were repeatedly scraped using a diamond file inside the preparation chamber with a base vacuum of 5.0×10^{-10} mbar and the spectra were taken within an hour, so as to avoid any surface degradation. All the measurements were repeated many times to ensure the reproducibility of the spectra. The low temperature photoemission measurements at 77 K were performed immediately after cleaning the sample surfaces followed by the room temperature measurements. TBLMTO-ASA [34] based band structure calculations were performed using the experimental lattice parameters reported earlier [8, 32]. For the RE doped SrFBiS₂, the Coulomb correlation energy, U for the La-f and Ce-f orbitals were incorporated by taking the value of U as 5.0 eV. The Hund's coupling parameter J was taken as 0.7 eV [35, 36].

5.3 Results and Discussions

Fig. 5.1 shows the tetragonal ($P4/nmm$) crystal structure of BiS₂ based superconductors [37]. The structure consists of stacks of rock salt type BiS₂ (superconducting layers) layers and

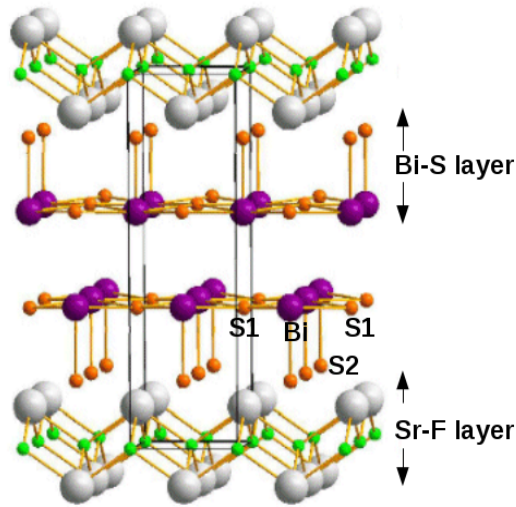


Figure 5.1: Crystal structure of SrFBiS_2 depicting two unit cells. Grey, green, purple and orange spheres correspond to Sr/RE, F, Bi and S atoms, respectively.

Flourite type SrF (spacer) layers. The BiS_2 layer is responsible for superconductivity while the spacer layer acts as charge reservoir. In case of Rare Earth (RE) doped compounds, the SrF layer also contains RE (La, Ce) atoms. The doping of Rare Earth (RE) atoms at Sr site leads to electron doping in the system. The structure of BiS_2 based compounds possess a striking similarity with the cuprates and Fe superconductors in terms of the superconducting layers separated by spacer layers. Each Bi atom (shown in fig 5.1) is bonded to two inplane S atoms S1 and a out of plane S atom S2. The angle S1-Bi-S1 is sensitive to electron doping, which shall be discussed later.

Unlike the Fe superconductors where the parent compounds are bad metals and cuprates with insulating parent compound, the BiS are semiconductors. The parent compound, SrFBiS_2 is semiconducting with band gap of 0.82 eV. The a and c lattice parameters are 4.08 Å and 13.78 Å respectively. A reduction in c lattice parameters occurs due to RE doping. 50 % Ce doping at Sr site leads to appearance of superconductivity with $T_c \sim 2.8$ K, with a simultaneous emergence of ferromagnetism below 7.5 K. The a and c lattice parameters are 4.0563 Å and 13.38 Å respectively. Ce doping provides carriers to the superconducting layers and meanwhile form ferromagnetic ordering in the (Sr,Ce)F layers. The Ce doped compound thus creates a platform to study the interplay between the coexisting superconductivity and magnetism in this system. $\text{Sr}_{0.5}\text{La}_{0.5}\text{BiS}_2$, is a superconductor with $T_c \sim 2.5$ K. The a and c lattice parameters are 4.077 Å and 13.388 Å respectively. The Ce and La doped compounds also show semiconducting behaviour (enhanced resistivity with decreasing temperature), although

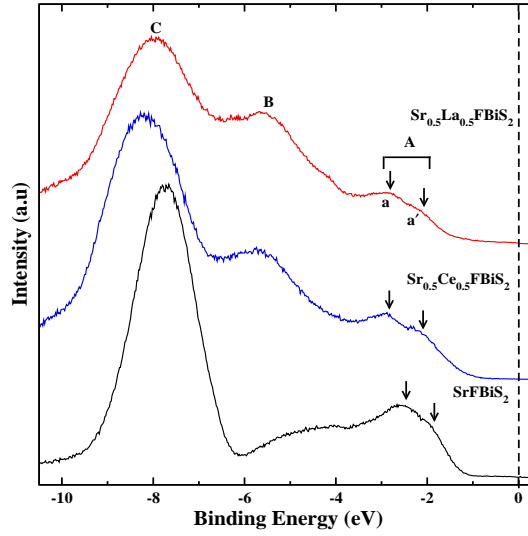


Figure 5.2: He II photoemission spectra for SrFBiS₂ (black), Sr_{0.5}Ce_{0.5}BiS₂ (blue) and Sr_{0.5}La_{0.5}BiS₂, with marked experimental features A, B and C. The sub features of A, a and a' are also marked.

the magnitude of resistivity is reduced with doping.

Fig 5.2 shows the photoemission spectra of SrFBiS₂, Sr_{0.5}Ce_{0.5}BiS₂ and Sr_{0.5}La_{0.5}BiS₂ taken by using HeII (40.8 eV) line. The spectra for all the compositions are dominated by three features A, B and C. They appear at -2.5, -4.5 and -7.7 eV, respectively, for the parent compound (SrFBiS₂). Feature A is composed of a sub feature 'a' positioned at -1.9 eV and a shoulder 'a'' at -2.5 eV for SrFBiS₂ (shown by arrows in fig 2(a)). The RE (Rare Earth = Ce and La) doped compounds show a shift of features A and B to higher binding energy, positioning them at -2.9, -5.5 eV respectively. The features 'a' and 'a'' shift to -2.1 and -2.8 eV respectively for RE doped compounds. The separation between feature A and B is increased with doping. The feature C shifts to higher binding energy with RE doping and occurs at 8.2 and 8.0 eV for Sr_{0.5}Ce_{0.5}BiS₂ and Sr_{0.5}La_{0.5}BiS₂ respectively.

In order to get more insights into the orbital character of the features, we calculated the density of states (DOS) and partial density of states (PDOS) using the LDA formalism. Results of the calculations are shown in fig 5.3 and 5.4. Effects of correlations of Ce/La-f orbitals on the DOS is clear from fig. 5.3(a) and 5.3(b) where we have compared the DOS for (U=5.0 J=0.7) and (U=J=0.0) respectively. Although, the correlation energy has no prominent influence on the valence band DOS, it causes noticeable changes in the conduction band states. The valence band extends from -12 eV to E_F while the conduction band spans from E_F to 4 eV binding energy. The valence band comprises of three major features A, B and C. Feature A spans

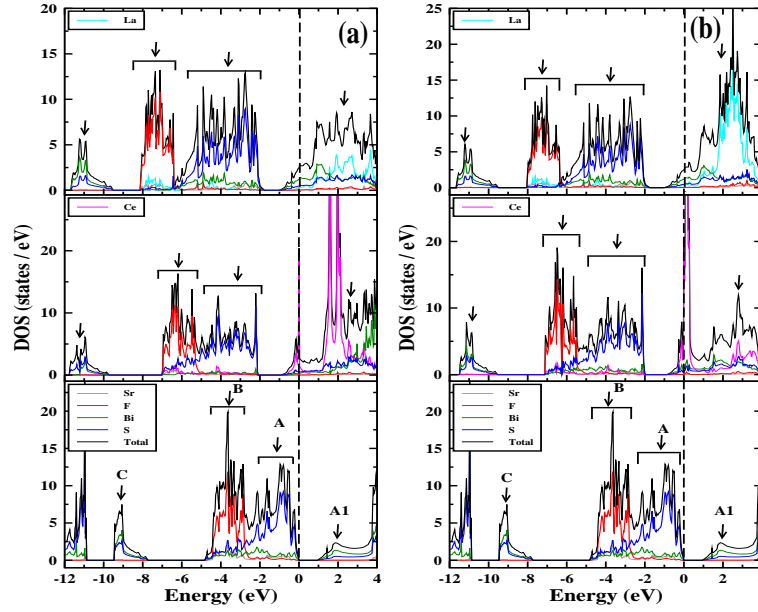


Figure 5.3: The calculated DOS for $\text{Sr}_{0.5}\text{RE}_{0.5}\text{BiS}_2$ with $U = 5.0$ eV, $J = 0.7$ eV (a), $U = J = 0$ (b) with the marked theoretical features.

from Fermi level to -2.5 eV for SrFBiS_2 . The PDOS calculations indicate that it is comprised predominantly of Bi-6p and S-3p hybridised states with a minor contribution from Sr-3d states. Feature A shifts to higher binding energy with RE doping and extends from -2.0 to -5.1 eV and -1.8 to -6.3 eV for the Ce and La doped compositions, respectively. The shift of feature A towards higher binding energy, consistent with electron doping for RE doped compositions, is also reflected in the photoemission spectra (fig 5.2) discussed previously.

Feature B, extending from -2.5 to -7.0 eV, for SrFBiS_2 , comprises predominantly of S-3p and F-2p hybridised states. This feature spans from -5.1 to -7.0 eV and -6.3 to -8.0 eV for the Ce and La doped compounds respectively. The shifting of this feature with RE doping is also seen in the experimental spectra (fig 5.2). The features A and B are closely spaced for the undoped system, while it becomes fully distinct for the La doped system (fig 5.3(a)). The feature C, appearing at -9 eV in case of the parent compound, consists of Bi-6s and S-3s states. This feature is also shifted to higher binding energy with RE substitution due to electron doping and occurs at -11.0 eV. The conduction band consists of feature A1 comprising of Bi-6p and S-3p hybridised unoccupied states, occurring at 2.0 eV energy for the parent compound. For the doped compounds, in addition to the Bi/S-p states, the contribution of the rare earth states (La/Ce-d and La/Ce-f) is also considerable. The Ce states are highly localised at E_F for $U=J=0$ case (fig 5.3(b)). Application of U results in the formation of a low DOS feature at E_F and a

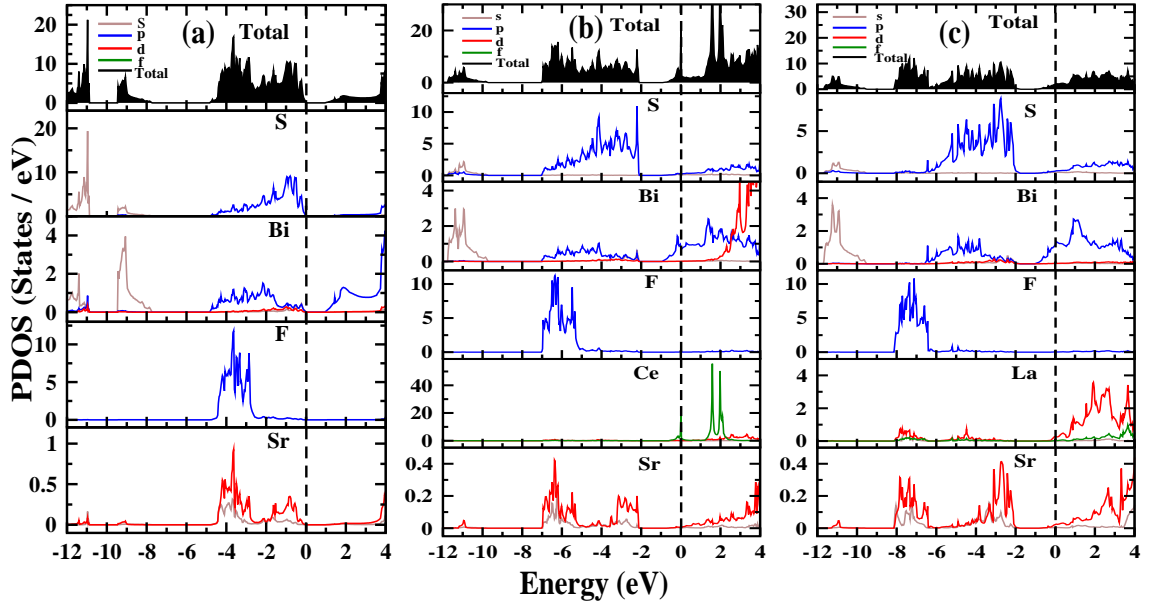


Figure 5.4: Calculated partial DOS for (a) SrFBiS₂, (b) Sr_{0.5}Ce_{0.5}BiS₂, (c) Sr_{0.5}La_{0.5}BiS₂. Vertical dashed line corresponds to Fermi level.

high density peak at 2 eV in the unoccupied side. The shifting of Ce states to higher energy, due to the application of U, in the unoccupied region has been reported in earlier studies [38]. Likewise, for the La doped compound, application of U results in broadening of La states, which are otherwise localised at ~ 2.5 eV in the unoccupied region. Thus doping of rare earth elements affect the features near the conduction band minimum and the Fermi level is shifted to the conduction band. The calculated DOS is in accordance with the previously reported band structure calculations on various BiS based superconductors [37, 39].

Fig 5.5 shows the band structure calculations for the parent (fig 5.5(a)), Ce doped (fig

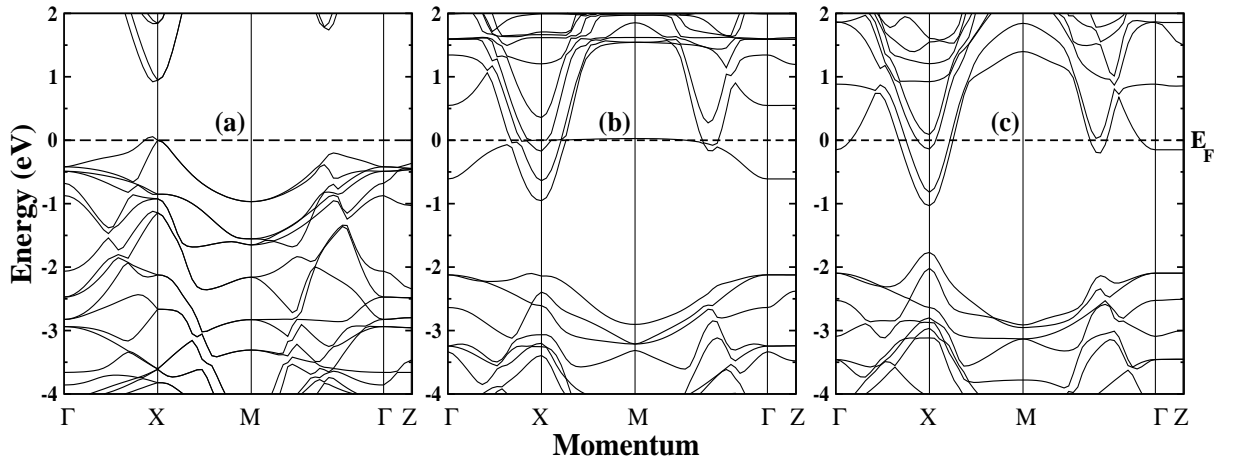


Figure 5.5: Calculated band structure for (a) SrFBiS₂, (b) Sr_{0.5}Ce_{0.5}BiS₂, (c) Sr_{0.5}La_{0.5}BiS₂

5.5(b)) and La doped (fig 5.5(c)) compositions. The near E_F band structures of the three compounds exhibit many similarities owing to their resemblance in terms of crystal structure. The absence of dispersion along the Γ - Z line suggests the quasi two dimensional character of these compounds. In case of SrFBiS₂, the valence band maximum (VBM) consists of a pair of degenerate band along the X-M direction which splits along the Γ -X direction. Likewise, the conduction band minimum (CBM) constitutes two pairs of degenerate bands along X-M direction which splits along the Γ -X direction. The splitting of these bands along Γ -X direction occurs due to the interlayer coupling [15]. Along M- Γ direction a pair of band occurs at 1/2 M- Γ , in the conduction band. The direct band gap of 0.9 eV between the VBM and CBM at X point signifies the semiconducting nature of SrFBiS₂. Previously reported band structure calculations predicted a gap of 0.8 eV at the X point [37]. The discrepancy of 0.1 eV could be due to the limitations of LDA in the prediction of exact band gap of semiconductors [40]. RE doping introduces electron carriers into the Bi-S conducting layer [41] which is reflected as a shift of Fermi level towards the conduction band. This is in accordance with the enhanced metallicity for the RE doped samples [10, 11] in comparison to the undoped compound [37]. The two degenerate pair of bands above the Fermi level along X-M direction, in case of the parent compound, show a lifting of degeneracy with RE doping and occurs below the Fermi level. Similarly, the pair of band along the M- Γ direction also occurs below the Fermi level for the doped compounds.

Fig 5.6(a) shows the 300 K high resolution He I photoemission spectra for SrFBiS₂ (black), Sr_{0.5}Ce_{0.5}FBiS₂ (blue) and Sr_{0.5}La_{0.5}FBiS₂ (red). The feature near E_F (composed of both A and A') is assigned to the Bi 6p states [15]. There occurs an enhancement of spectral weight from E_F to -0.2 eV (A') with a simultaneous depletion of states from -0.2 to -0.6 eV (A) for the doped compounds. Doping of RE atoms introduces electrons into the Bi-S plane thereby enhancing the metallicity [9,42]. Further, it causes an increase of the inplane S1-Bi-S1 bond angle (shown in fig 1), which approaches almost 180° at the optimum RE doping of 0.5 [43]. The flat S1-Bi-S1 plane enhances the hybridisation of Bi 6p_{x/y} and S 3p_{x/y} orbitals. Further, theoretical calculations by Usui et al. and Xing et al. have shown that the change in Fermi surface topology for electron doping of x = 0.5, causes an enhanced density of states at E_F [4, 16]. This could be a plausible cause for the spectral weight shift from A to A' for the doped superconductors. Thus the combined effect of reduced distortion of S1-B-S1 plane and change in Fermi surface topology may lead to the spectral weight shift from A to A'.

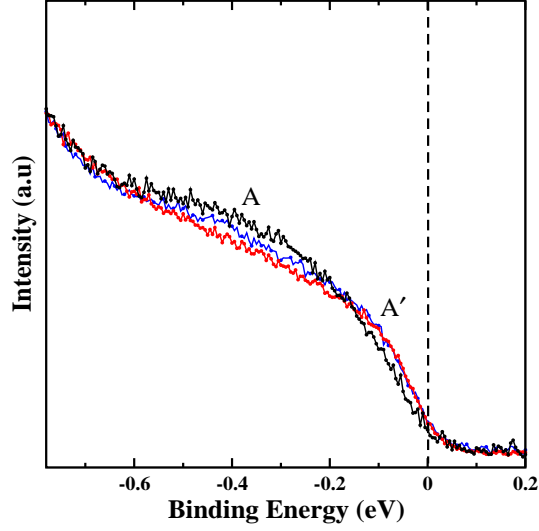


Figure 5.6: (a) High resolution He I photoemission spectra for SrFBiS₂ (black), Sr_{0.5}Ce_{0.5}BiS₂ (blue), (c) Sr_{0.5}La_{0.5}BiS₂ (red) (b) High resolution He I photoemission spectra at 300 K (black) and 77 K (red) for SrFBiS₂ (a), Sr_{0.5}Ce_{0.5}BiS₂ (b), Sr_{0.5}La_{0.5}BiS₂ (c). Dashed vertical line corresponds to E_F

Such spectral weight shifts, observed in the case of manganites [46], was ascribed to the phase separation. Both the cuprates [47] and the BiS superconductors, exhibit a high density of states at E_F in comparison to the undoped, non superconducting parent compound. In contrast, the Fe superconductors show a reduced spectral weight near E_F in comparison to the parent non superconducting compound [45]. This can also be inferred from the previous chapters, where we see a depleted density of states near Fermi level for the superconducting compound (FeSe, NdFeAsO_{0.8}F_{0.2}) in comparison to the parent FeTe and NdFeAsO compound. The BiS₂ superconductors resemble the cuprates in terms of the structure and higher spectral weight for the doped compounds.

5.4 Conclusion

In conclusion, our valence band photoemission and LDA based band structure calculations, reveal the valence band electronic structure of Rare Earth (La,Ce) doped BiS₂ superconductors. RE doping introduces electron carriers causing an enhanced metallicity. The Fermi level is shifted towards conduction band which results in the shifting of valence band features towards higher binding energy, for the doped compounds. Further, the degeneracy of the bands at VBM and CBM, along XM direction is lifted with RE doping. The reduced distortion of BiS plane and change in Fermi surface topology, is reflected as increased spectral weight near fermi level

and a corresponding decrease in density of states at higher binding energy, for the RE doped compounds.

Bibliography

- [1] Y Mizuguchi, H. Fujihisa, Y. Gotoh, K. Suzuki, H. Usui, K. Kuroki, S. Demura, Y. Takano, H. Izawa, and O. Miura, Phys. Rev. B **86** 220510, 2012.
- [2] Y. Mizuguchi, S. Demura, K. Deguchi, Y. Takano, H. Fujihisa, Y. Gotoh, H. Izawa, and O. Miura, J. Phys. Soc. Jpn. **81**, 114725 (2012).
- [3] S. Demura, Y. Mizuguchi, K. Deguchi, H. Okazaki, H. Hara, T. Watanabe, S. J Delhome, M. Fujioka, T. Ozaki, H. Fujihisa, Y. Gotoh, O. Miura, T. Yamaguchi, H. Takeya, and Y. Takano, J. Phys. Soc. Jpn. **82**, 033708 (2012).
- [4] J. xing, S. Li, X. Ding, H. Yang, and H. -H. Wen, Phys. Rev. B **86**, 214518 (2012).
- [5] D. Yazici, K. Huang, B. D. White, A. H. Chang, A. J. Friedman, and M. B. Maple, arXiv:1301.3932 (2013).
- [6] R. Jha, H. Kishan, and V. P. S. Awana, arXiv:1406.4231 (2014).
- [7] M. Nagao, A. Miura, S. Demura, K. Deguchi, S. Watauchi, T. Takei, Y. Takano, N Kumada, and I. Tanaka, Solid State Comm. **178**, 33 (2014).
- [8] R. Jha, B. Tiwari, and V. P. S Awana, J. Appl. Phys. **117**, 013901 (2015).
- [9] X. Lin, X. Ni, B. Chen, X. Xu, X. Yang, J. Dai, Y. Li, X. Yang, Y. Luo, Q. Tao, G. Cao, and Z. Xu, Phys. Rev. B **87**, 020504 (2013).
- [10] Y. Li, X. Lin, L. Li, N. Zhou, X. Xu, C. Cao, J. Dai, L. Zhang, Y. Luo, W. Jiao, Q. Tao, G. Cao, and Z. Xu, Supercond. Sci. Technol. **27**, 035009 (2014).
- [11] L. Li, Y. Li, Y. Jin, H. Huang, B. Chen, X. Xu, J. Dai, L. Zhang, X. Yang, H. Zhai, G. Cao, and Z. Xu, Phys. Rev. B **91**, 014508 (2015).

- [12] D. Yazici, K. Huang, B. D. White, I. Jeon, V. W. Burnett, A. J. Friedman, I. K. Lum, M. Nallaiyan, S. Spagna, and M. B. Maple, *Phys. Rev. B* **87**, 174512 (2013).
- [13] H. F. Zhai, Z. T. Tang, H. Jiang, K. Xu, K. Zhang, P. Zhang, J. K. Bao, Y. L. Sun, W. H. Jiao, I. Nowik, I. Felner, Y. K. Li, X. F. Xu, Q. Tao, C. M. Feng, Z. A. Xu, and G. H. Cao, *Phys. Rev. B* **90**, 064518 (2014).
- [14] H. F. Zhai, P. Zhang, S. Q. Wu, C. Y. He, Z. T. Tang, H. Jiang, Y. L. Sun, J. K. Bao, I. Nowik, I. Felner, Y. W. Zeng, Y. K. Li, X. F. Xu, Q. Tao, Z. A. Xu, and G. H. Cao, *J. Am. Chem. Soc.* **136**, 15386 (2014).
- [15] L. K. Zeng, X. B. Wang, J. Ma, P. Richard, S. M. Nie, H. M. Weng, N. L. Wang, Z. Wang, T. Qian, and H. Dang, *Phys. Rev. B* **90**, 054512 (2014).
- [16] H Usui, K Suzuki, and K Kuroki, *Phys. Rev. B* **86**, 220501 (2012).
- [17] X. Wan, H. -C. Ding, S. Y. Savrasov, and C. -G. Duan, *Phys. Rev. B* **87**, 115124 (2013).
- [18] T. Yildirim, *Phys. Rev. B* **87**, 020506 (2013).
- [19] B. Li, Z. W. Xing, G. Q. Huang, *Europhys. Lett.* **101**, 47002 (2013).
- [20] G. Lamura, T. Shiroka, P. Bonfá, S. Sanna, R. De Renzi, C. Baines, H. Luetkens, J. Kajitani, Y. Mizuguchi, O. Miura, K. Deguchi, S. Demura, Y. Takano, and M. Putti, *Phys. Rev. B* **88**, 180509 (2013).
- [21] Shruti, P. Srivastava, and S. Patnaik, *J. Phys.:Condens. Matter* **25**, 312202 (2013).
- [22] Z. R. Ye, H. F. Yang, D. W. Shen, J. Jiang, X. H. Niu, D. L. Feng, Y. P. Du, X. G. Wan, J. Z. Liu, X. Y. Zhu, H. H. Wen, and M. H. Jiang, *Phys. Rev. B* **90**, 045116 (2014).
- [23] G. B. Martins, A. Moreo, and E. Dagotto, *Phy. Rev. B* **87**, 081102 (2013).
- [24] Y. Liang, X. Wu, and W. -F. Tsai, *J. Hu, Front. Phys* **9**, 194 (2014).
- [25] J. Lee, M. B. Stone, A. Huq, T. Yildirim, G. Ehlers, Y. Mizuguchi, O. Miura, Y. Takano, K. Deguchi, S. Demura, and S.-H. Lee, *Phys. Rev. B* **87**, 205134 (2013).
- [26] S. Li, H. Yang, D. Fang, Z. Wang, J. Tao, X. Ding, H. H. Wen, *Sci. China-Phys. Mech. Astron.* **56**, 2019 (2013).

- [27] J. Liu, D. Fang, Z. Wang, J. Xing, Z. Du, S. Li, X. Zhu, H. Yang, and H. -H. Wen, *Europhys. Lett.* **106**, 67002 (2014).
- [28] T. Zhou, and Z. D. Wang, *J. Supercond. Nov. Magn.* **26**, 2735 (2013).
- [29] C. -L. Dai, Y. Yang, W. -S. Wang, and Q. -H. Wang, *Phys. Rev. B* **91**, 024512 (2015).
- [30] Y. Yang, W. -S. Wang, Y. -Y. Xiang, Z. -Z. Li, and Q. -H. Wang, *Phys. Rev. B* **88**, 094519 (2013).
- [31] S. Nagira, J. Sonoyama, T. Wakita, M. Sunagawa, Y. Izumi, T. Muro, H. Kumigashira, M. Oshima, K. Deguchi, H. Okazaki, Y. Takano, O. Miura, Y. Mizuguchi, K. Suzuki, H. Usui, K. Kuroki, K. Okada, Y. Muraoka, and T. Yokoya, *J. Phys. Soc. Jpn.* **83**, 033703 (2014).
- [32] R. Jha, B. Tiwari, and V. P. S. Awana, *J. Phys. Soc. Jpn.* **83**, 105001 (2014).
- [33] R. Jha, B. Tiwari, and V. P. S. Awana, *J. Phys. Soc. Jpn.* **83**, 063707 (2014).
- [34] O. K. Anderson, *Phys. Rev. B* **12**, 3060 (1975).
- [35] M. Gamża, A. Ślebarski, and H. Rosner, *Eur. Phys. J. B* **63**, 1 (2008).
- [36] J. Chung, J. Park, J. -G. Park, B. -H. Choi, S. -J. Oh, E. -J. Cho, H. -D. Kim, and Y. S. Kwon, *J. Korean Phys. Soc.* **38**, 744 (2001).
- [37] H. Lei, K. Wang, M. Abeykoon, E. S. Bozin, and C. Petrovic, *Inorg. Chem.* **52**, 10685 (2013).
- [38] S. Banik, A. Arya, A. Bendounan, M. Maniraj, A. Thamizhavel, I. Vobornik, S. K. Dhar, and S. K. Deb, arXiv: 1404.5167 (2014).
- [39] N. Benayad, M. Djermouni, and A. Zaoui, *Computational Condensed Matter* **1**, 19 (2014).
- [40] C. Persson, and S. Mirbt, *Braz. J. Phys.* **36**, 286 (2006).
- [41] H. Sakai, D. Kotajima, K. Saito, H. Wadati, Y. Wakisaka, M. Mizumaki, K. Nitta, Y. Tokura, and S. Ishiwata, *J. Phys. Soc. Jpn.* **83**, 014709 (2014).
- [42] B. Li, Z. W. Xing, and G. Q. Huang, *Europhys. Lett.* **101**, 47002 (2013).

- [43] D. Yazici, I. Jeon, B. D. White, and M. B. Maple, *Physica C* **514**, 218 (2015).
- [44] A. Ino, T. Mizokawa, K. Kobayashi, and A. Fujimori, *Phys. Rev. Lett.* **81**, 2124 (1998).
- [45] T. sato, K. Nakayama, Y. Sekiba, T. Arakane, K. Terashima, S. Souma, T. Takahashi, Y. Kamihara, M. Hirano, and H. Hosono, *J. Phys. Soc. Jpn.* **77**, 65 (2008).
- [46] P. Pal, M. K. Dalai, R. Kundu, B. R. Sekhar, *Phys. Rev. B* **77**, 184405 (2008).
- [47] A. Ino, T. Mizokawa, K. Kobayashi, A. Fujimori, *Phys. Rev. Lett.* **81**, 2124 (1998).

Chapter 6

Electronic structure study of GeSe semiconductor

The previous three chapters (chapter 3,4,5) dealt with the electronic structure investigation of layered superconductors. This chapter describes the detailed electronic structure study of a layered semiconductor Germanium Selenide (GeSe). Angle resolved Photoemission Spectroscopy (ARPES) and X-ray Photoemission Spectroscopy (XPS) in conjunction with the LDA based band structure calculation describes the valence band electronic structure of GeSe single crystal.

6.1 Introduction

The inadequacy of graphene in technological applications owing to its zero band gap, has led to many re-investigations of alternative two dimensional layered compounds [1]. The narrow and finite band gaps of these layered materials enhance their functionality in device applications. Recently, 2D chalcogenides with layer dependent band gaps have attracted much attention due to their richness in fundamental physics [2–4] as well as diverse applications in thermoelectrics, optical filters, optical recording materials, infrared detectors, photovoltaics energy storage, photocatalysis, sensors etc. [5, 6]. There has been an upsurge of research on the IV-VI semiconductors, particularly, the Germanium Selenide systems due to its use in random access memory applications and radiation sensors [7, 8]. Owing to the small band gap, 1.07 eV [9], GeSe systems are promising candidates in solar cell industry [10] and photovoltaics [11]. Moreover, the Ge based semiconductors (i.e., GeSe, GeS) are potential alternatives to their counterparts such as narrow-band-gap systems containing Pb, Cd, and Hg due to the advantages of their relatively higher stability and environmental sustainability [10].

Germanium Selenide belongs to the family of IV-VI layered chalcogenide semiconductors with orthorhombic structure (Pnma) [12]. The layers of atoms are separated by van der Waals forces, making the material cleavable along the b-c [100] planes. Various experimental studies on GeSe including High resolution energy loss spectroscopy (HREELS) [13], transmittance [9], reflectance [14], thermorefectance [15], refraction index measurements [16], photoconductivity [17], photoelectron partial-yield and constant-initial-state (CIS) spectroscopies [18], X-ray powder diffraction and Raman spectroscopy [19], have explored the optical and structural properties of this system. Though photemission [20–22] studies on GeSe have been reported earlier, there are no reports till date focussing on the extensive electronic structure using Angle Resolved Photoemission (ARPES) technique. The former technique has been quite successful in elucidating the momentum-resolved valence band electronic structure of the layered semiconductors [23–25]. The band structure analysis of GeSe may motivate the synthesis of new doped Germanium based chalcogenides with enhanced optoelectronic applications.

In this paper, a detailed electronic structure study of the valence band as well as core levels using ARPES and X-ray photoelectron spectroscopy (XPS) respectively is reported on GeSe single crystals. The experimental band structures obtained from ARPES are also compared with our LDA based band structure calculations.

6.2 Experimental

The synthesis of GeSe single crystals, via chemical vapor technique, and its characterisation have been reported elsewhere [26]. The samples were cleaved in-situ by the standard post technique. The surface quality and the crystallographic symmetry directions were confirmed by in-situ low energy electron diffraction (LEED). The surface cleanliness of the cleaved surfaces were checked by using X-Ray Photoelectron Spectroscopy (XPS) employing monochromatic Mg K α (1253.4 eV) source. ARPES experiments were performed using SCIENTA-R4000WAL electron energy analyser with a 2D-CCD detector at a base pressure of 4×10^{-11} mbar. HeI α (21.2 eV) resonance line, using a high flux GAMMADATA VUV He lamp (VUV5000) attached to a VUV monochromator (VUV5040), was used to excite the photoelectrons from the sample surface. The polar angle θ was varied to cover the different symmetry directions of the Brillouin zone. All the experiments were performed at room temperature with an angular resolution better than 0.7° in the wide-angle mode (15°) of the analyser while the analyser energy

resolution was ~ 2 meV. Fermi energies for all measurements were calibrated using a freshly evaporated Ag film on a sample holder. Band structure calculations have been performed by TBLMTO-ASA [27] utilising the lattice parameters and atomic coordinates of GeSe reported by Okazaki et al. [28].

6.3 Results and Discussions

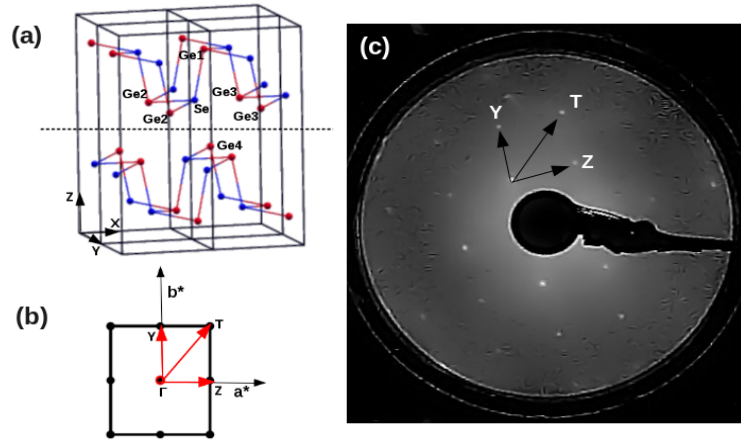


Figure 6.1: (a) Crystal structure of GeSe with two unit cells. Red and blue dots correspond to Germanium and Selenium atoms respectively. Ge1, Ge2, Ge3 and Ge4 correspond to first, second, third and fourth nearest neighbours respectively. The dashed line shows the cleavage plane along x-y plane. (b) The surface Brillouin zone, showing the high symmetry directions (red lines) of the GeSe single crystal. (c) LEED pattern taken at 120 eV, with bright spots arranged in rectangular fashion indicating the rectangular symmetry of the Brillouin zone. The marked directions (black lines) in the LEED image correspond to the symmetry directions shown in fig b (marked by red lines).

Fig 6.1(a) shows the orthorhombic crystal structure of GeSe single crystal. A single unit cell contains eight atoms situated in two adjacent double layers along the z axis. The atoms in each double layer is bonded to their three nearest neighbours in a zig-zag fashion. The neighbouring Ge atoms surrounding the Se atoms are marked in fig 6.1(a). The van der Waals force between the adjacent layers makes the crystal cleavable along its xy plane giving a quasi-two-dimensional crystal structure suitable for ARPES measurements. The surface Brillouin zone of GeSe showing the high symmetry directions of GeSe crystal is presented in fig 6.1(b). The orientation of the crystal structure as obtained from LEED is shown in fig 6.1(c). The spots arranged in rectangular pattern conform to the rectangular Brillouin zone of GeSe surface.

The bonding in GeSe system can be inferred from fig 6.2 which shows the Se-4p orbital

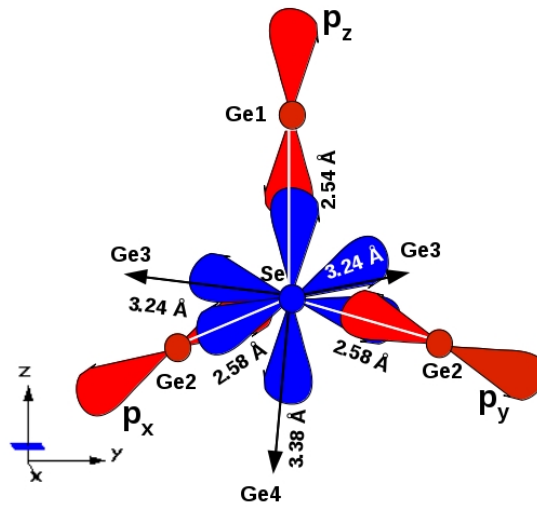


Figure 6.2: GeSe local bonding picture representing the p orbitals of Se atom (blue) along with the p orbitals of the neighbouring Ge atom (red). These atoms correspond to the same ones shown in fig 1(a).

overlap with its neighbouring Ge-4p orbitals. Each Se atom is bonded to its first nearest neighbour Ge1 atom at distance 2.54 Å and second nearest neighbour Ge2 atoms at distance of 2.58 Å. The third and fourth nearest neighbours are Ge3 and Ge4 atoms located at distances 3.24 and 3.38 Å respectively from the Se atom. The Se- $p_{x/y}$ orbitals are bonded to $p_{x/y}$ orbitals of Ge2 and Ge3 atoms. The Se- p_z orbital is bonded to p_z orbitals of Ge1 and Ge4 atoms. The bonding between Se- p_z and Ge4- p_z is relatively weaker in comparison to other bonds since Ge4 atom is bonded to Se atom by van der Waals force (shown in fig 6.1(a)). Hence, the hybridisation between Se $p_{x/y}$ and Ge $p_{x/y}$ orbitals is expected to be relatively stronger in comparison to Se p_z and Ge p_z orbitals.

The LDA based density of states (DOS) calculations ranging from -16 eV to 10 eV is represented in fig 6.3. The spectral features from E_F till -16 eV binding energy constitutes the valence band region. The region from E_F to 10 eV comprises the conduction band region. Peak A and B are predominantly hybridised Ge-4p and Se-4p bonding states with a little admixture of Ge 4s states near the valence band maximum. Despite the larger spatial extent of Ge 4s lone pairs, the wide spanning Ge 4p - Se 4p hybridised states lead to the diffusion of Ge 4s lone pair, hence, Ge 4s state is concentrated within a small region near the top of valence band [29]. The next set of bands, marked as C, extending from -6 eV to -10 eV binding energy, is the Ge 4s dominating region. The lowest region (-12 eV to -14 eV) in the valence band, D, represents the Se 4s states. The feature A' in the conduction band region corresponds to the Ge-4p -

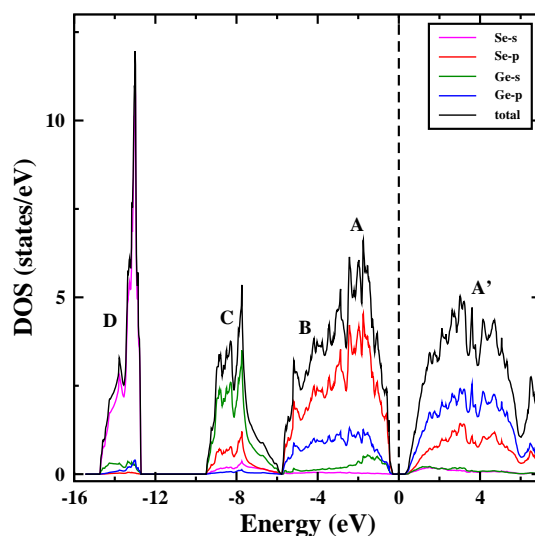


Figure 6.3: LDA density of states representing the s and p orbital contributions of Ge and Se atoms to the total density of states.

Se-4p antibonding states. The positions of these bands are similar to the earlier reported band structure calculations [12] and photoemission results [20, 21].

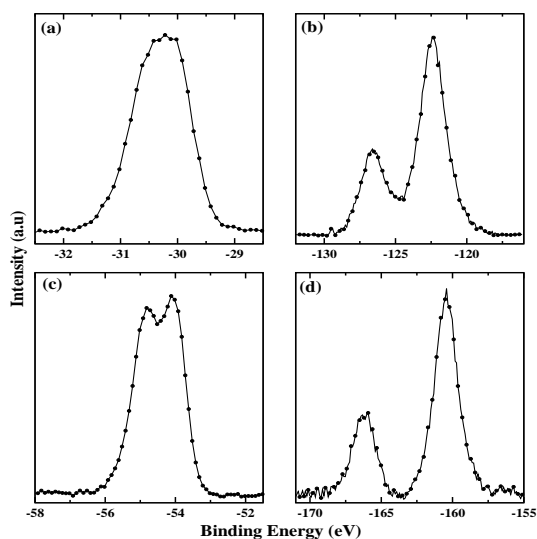


Figure 6.4: The core level spectra corresponding to Ge 3d, Se 3d, Ge 3p and Se 3p levels shown in fig (a), (b), (c) and (d) respectively.

The chemical constituents of the GeSe crystal surface, confirmed from the core level XPS spectra shown in fig 6.4(a-d), matches with the earlier reports [30]. The Ge 3d region (fig 6.4(a)) shows a feature at 30.2 eV corresponding to the Ge 3d states. The experimental resolution limit leads to unresolvable Ge $3d_{3/2}$ and Ge $3d_{5/2}$ features which are spin orbit splitted by 0.6 eV [31]. Fig 6.4(b) shows Se $3d_{5/2}$ and Se $3d_{3/2}$ lines at 54.9 eV and 54.1 eV respectively. The

Ge 3p region (fig 6.4(c)) shows the prominent Ge 3p_{3/2} and Ge 3p_{1/2} lines at 122.4 eV and 126.5 eV respectively while the Se 3p region (fig 6.4(d)) shows features corresponding to Se 3p_{3/2} and Se 3p_{1/2} at 160.4 eV and 166.2 eV respectively.

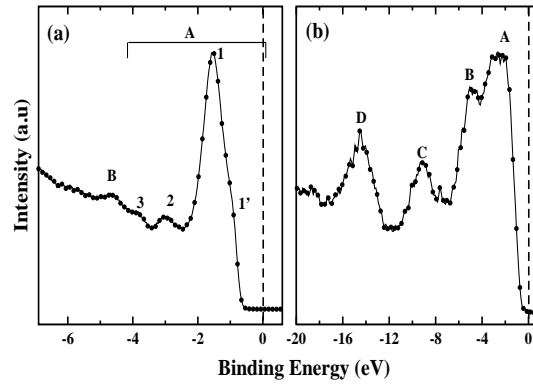


Figure 6.5: Valence band region marked with prominent features probed using (a) Mg K α source (b) He I. The dashed lines correspond to the Fermi Level.

The valence band region of GeSe probed by XPS (Mg K α) and He I and is displayed in fig 6.5. The He I valence band (fig 6.5(b)) shows two features A and B. A is composed of sub features 1', 1, 2, 3 occurring at -0.9, -1.55, -3.0 and -3.9 eV binding energy, respectively. Feature B is positioned at -4.7 eV binding energy. The XPS valence band region shown in fig 6.5(b) represents four prominent features A, B, C and D positioned at -2.4, -4.6, -8.9 and -14.2 eV binding energy respectively. The sub features of A prominent in the case of He I spectra merge into a single feature A in the XPS spectra [21]. Feature D is well separated from rest of the features in the valence band signifying the core like nature of the Se 4s level. The experimentally observed features conform to our LDA based density of states calculations discussed in the preceding paragraph.

Angle Resolved Photoemission Spectra (ARPES) of GeSe single crystal was measured along different symmetry directions of the Brillouin zone using He I excitation source and varying polar angles (θ). Fig 6.6(a) shows the energy distribution curves (EDC) along the Γ -Z direction. The spectrum for the Γ point shows four features at -1.50, -3.0, -3.8 and -4.7 eV and a weak shoulder at -1.0 eV. With increasing polar angle beyond the Γ point, the shoulder at -1.0 eV becomes more prominent. This feature disperses towards E_F for few polar angles reaching -0.5 eV at $\sim 1/2$ Γ -Z, and then disperses back towards higher binding energy with further increase in polar angle. The feature at -1.5 eV initially disperses towards higher binding energy near the Γ point and then moves towards E_F till the Z point. This band disperses towards higher

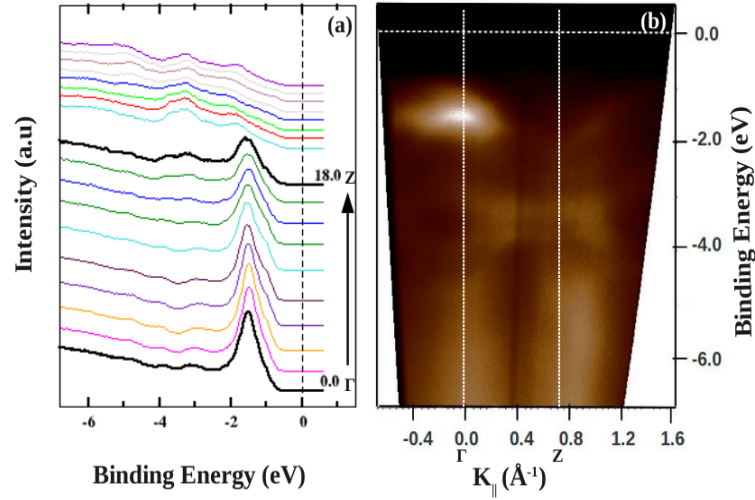


Figure 6.6: (a)EDC from ARPES on GeSe along Γ -Z direction of its Brillouin zone. The polar angle theta for Γ point and Z point (curves represented by thick black bold lines) is marked in the figure.Dotted line represents the Fermi level (b) Intensity plot of binding energy as a function of parallel component of momentum ($K_{||}$) representing the band dispersion. Vertical dotted lines correspond to Γ point and Z point while the horizontal dotted line represents the Fermi level.

binding energy in the next Brillouin zone. The feature at -3.0 eV disperses towards E_F near the Γ point and then disperses towards higher binding energy till the Z point, beyond which it again moves towards E_F . The feature at -3.8 eV which initially disperses towards higher binding energy, moves towards E_F and merges with the peak at -3.0 eV near Z point. The faint feature at -4.7 eV disperses towards lower binding energy till the Z point and disperses away from E_F , beyond the Z point. The feature at -5.8 eV remains dispersionless over the entire Brillouin zone. The band dispersion is visible in the intensity plot shown in Fig 6.6(b).

Fig 6.7(a) shows the ARPES EDC plots along the Γ -Y direction of the Brillouin zone of GeSe single crystal. The intensity plot for the same is represented in Fig 6.7(b). The weak feature at -1.0 eV disperses away from E_F along this direction. The -1.5 eV feature moves towards higher binding energy and reaches -2.05 eV at Y point, beyond which it disperses towards E_F . These bands are more dispersing along Γ -Y direction in comparison to Γ -Z direction. The features at -3.0 eV and -3.6 eV approach towards each other and merge completely into a single peak at Y point. The dispersion of these bands are weaker along Γ -Y direction in comparison to Γ -Z direction. The -4.7 eV feature disperses towards higher binding energy. Non dispersive feature occurs at -5.8 eV, similar to Γ -Z direction. The bands near the valence band maximum are more dispersive than the higher binding energy bands along Γ -Y direction unlike the case

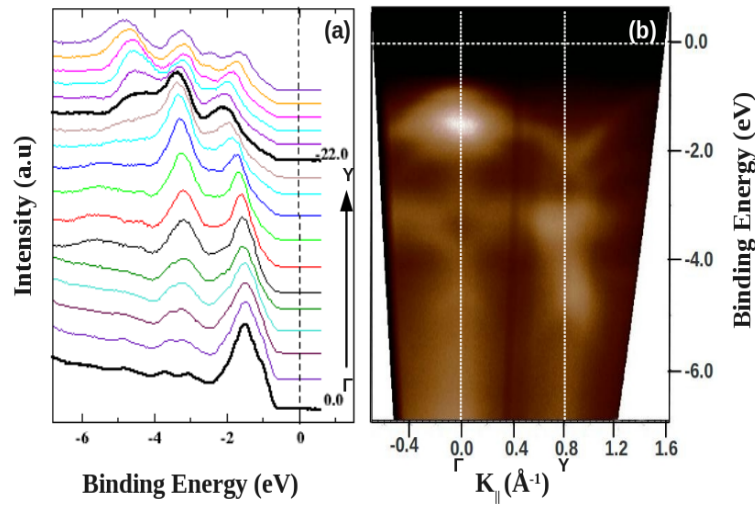


Figure 6.7: ARPES spectra along Γ -Y direction represented in form of (a) EDC (b) intensity plot. Vertical lines in (b) represent the Γ point and Y point.

of Γ -Z direction.

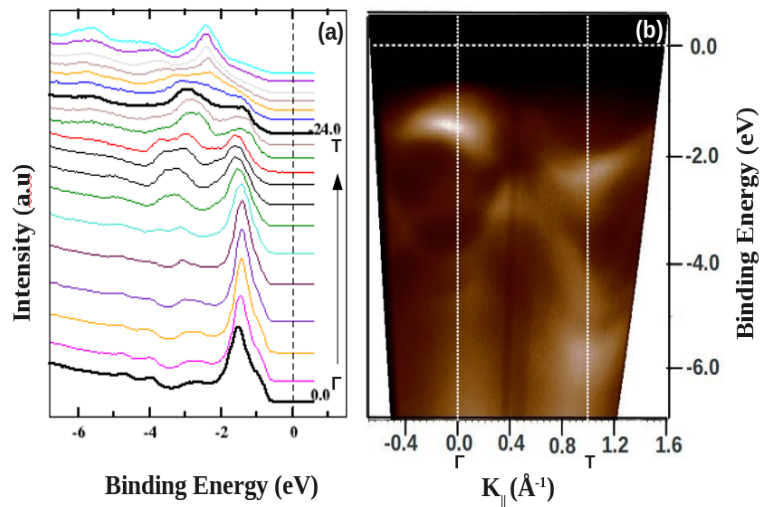


Figure 6.8: ARPES spectra along Γ -T direction represented in form of (a) EDC (b) intensity plot. Vertical lines in (b) represent the Γ point and T point.

Fig 6.8(a) shows the EDC plot along Γ -T direction and its corresponding intensity plot is shown in fig 6.8(b). The weak feature at -1.0 eV shifts towards higher binding energy along this direction. The -1.5 eV feature initially disperses away from E_F , but moves towards lower binding energy on approaching the T point. The -3.0 and -3.6 eV features move towards each other and merge into a single feature. Further increase in polar angle leads to splitting of the single merged feature into two features. The lower binding energy feature disperses towards E_F while the higher binding energy feature disperses away from E_F till the T point. Beyond

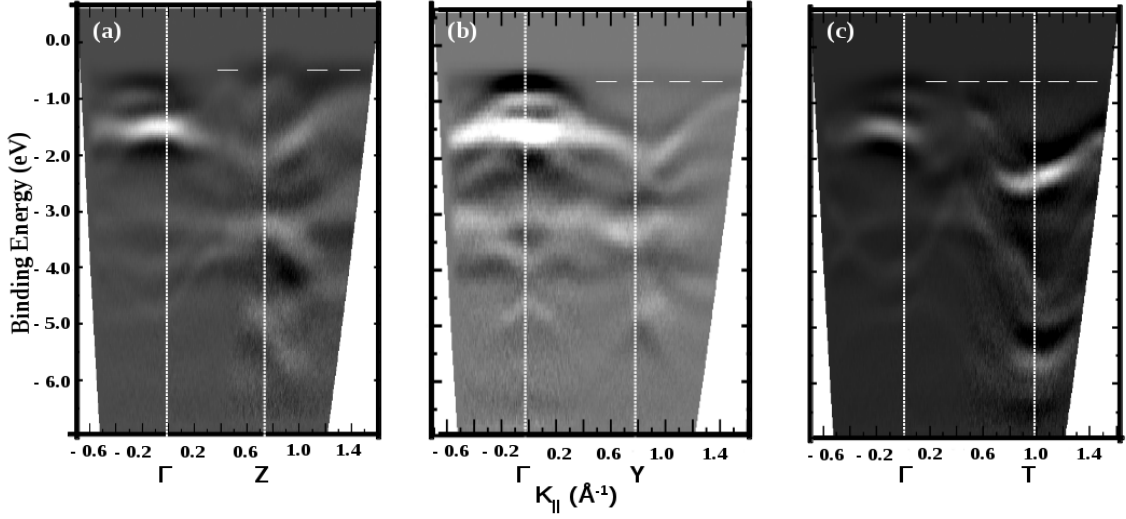


Figure 6.9: The second derivative of intensity plot, $\partial^2 I / \partial E^2$ versus momentum component parallel to the sample surface, along (a) Γ -Z, (b) Γ -Y and (c) Γ -T directions of the Brillouin zone. Vertical dashed lines correspond to the high symmetry points.

the T point, the lower binding energy feature disperses away from E_F while the higher binding energy feature vanishes. The feature at -4.9 eV disperses towards higher binding energy. The -5.8 eV feature remains non dispersive along the entire symmetry direction. All the bands along Γ -T direction exhibit greater dispersion in comparison to the same ones along the other two symmetry directions.

To enhance the visibility of the bands, the second derivative of the ARPES intensity plot along Γ -Z, Γ -Y and Γ -T directions, have been shown in fig 6.9(a-c). The horizontal white dotted line in fig 6.9 represents the nondispersive bands present near valence band maximum (VBM) at a binding energy ~ 0.7 eV. Similar non dispersive features around valence band maximum were reported in previous photoemission experiments [32, 33] which could be attributed to the final state effect and surface states. Another non dispersing band occurs at ~ -6.0 eV, along all the symmetry directions, visible in the EDC spectra. Similar features reported earlier [32] have been interpreted as the phonon assisted non k conserving (indirect) transitions from the occupied to the unoccupied states. These non dispersive features are inherent to various II-VI, III-V, elemental semiconductors [33–35] as well as graphite systems [25].

Fig 6.10(a-c) represents the the experimental data points extracted from the second derivative image and its superposition on the calculated LDA band structure plot along the various symmetry directions. The experimental data points match reasonably well with the calculated bands. The bands at VBM is very less dispersing along Γ -Z direction while it is remarkably

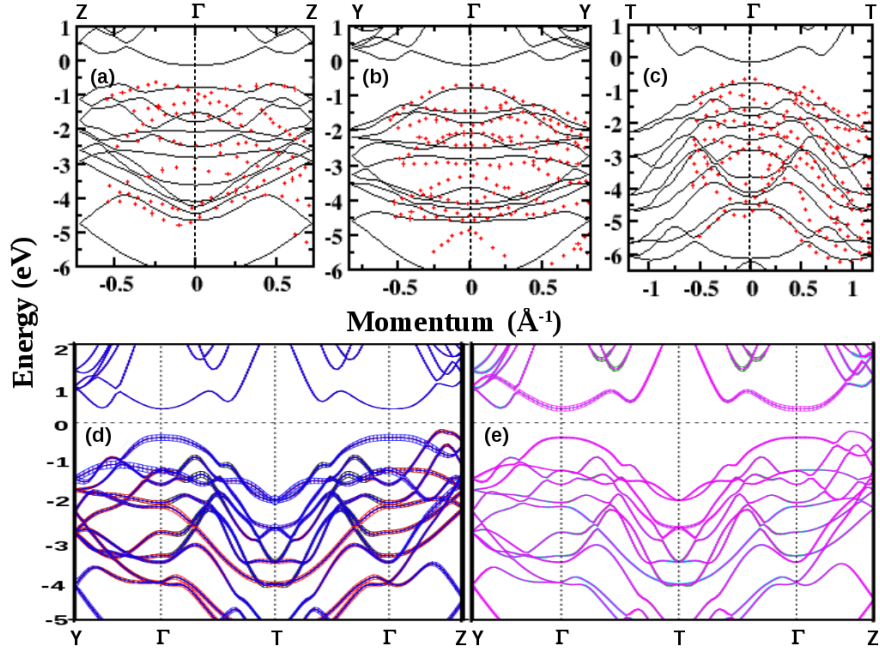


Figure 6.10: Energy versus momentum component parallel to the sample surface ($E(k)$ vs $K_{||}$) representing the experimental data points (red circles) superposed on calculated band structure plot (black curves) along (a) Z- Γ -Z, (b) Y- Γ -Y and (c) T- Γ -T directions of the Brillouin zone. The fatness of band for GeSe calculated for (d) Se-4p orbitals and (e) Ge-4p orbitals. Black, red and blue denotes Se- p_x , p_y and p_z orbitals respectively while green, cyan and magenta denotes Ge- p_x , p_y and p_z orbitals respectively.

dispersing along Γ -T direction. The bands near the Fermi level matches with the theoretical results in all the symmetry directions. The valence band maximum occurs at $\sim 1/2$ Γ -Z, at binding energy -0.5 eV, indicating the indirect band gap in GeSe. The bands in the range of -3 eV to -5 eV also matches well with the theoretical bands .

The difference in dispersion of bands in the ARPES spectra is expected due to the variation in contribution of Se and Ge 4p orbitals. To get a better insight of the orbital contribution along various symmetry directions, the LDA FAT band calculations for Ge and Se 4p orbitals are shown in fig 6.10(d,e). The fatband graph indicates that the Se-4p orbitals are more dominating (as seen by the fatness of Se-4p orbitals) in comparison to Ge-4p along all the symmetry directions. The top of the valence band comprises of predominantly Se- p_z (blue) orbitals while the bands in the range -2 eV to -4 eV consists of contributions from all the Se 4p orbitals (Se- p_x (black) , Se- p_y (red) and Se- p_z (blue)). The presence of Se- p_z orbitals near the VBM signifies the relatively low hybridisation of Se-Ge 4p $_z$ orbitals, in comparison to Se-Ge $p_{x/y}$ orbitals which are positioned at higher binding energy. The nature of dispersion along different

directions is dependent on the difference in hybridisation of Se 4p-Ge 4p orbitals. There is a distinct difference in the dispersion of bands along Γ -T direction in comparison to Γ -Y and Γ -Z directions. The predominance of p_z orbitals along Γ -T direction may be the cause for the highly dispersing bands along Γ -T direction unlike the other symmetry directions.

6.4 Conclusion

The electronic structure of GeSe was investigated using XPS and ARPES. The core level XPS confirms the chemical constituents while ARPES probes the valence band dispersion. The observed ARPES band dispersion along the Γ -Z, Γ -Y and Γ -T symmetry directions match qualitatively with the LDA based theoretical band structure calculations. The bands in the VBM and -3 eV to -5 eV binding energy region, matches well with the theoretical bands. Non dispersive bands related to the surface states and indirect transitions were reported. The valence band maximum occurs along Γ -Z direction, at binding energy 0.5 eV, corroborating the indirect band gap of GeSe. The predominant contribution of Se 4 p_z orbitals along Γ -T direction could be the reason for the highly dispersive bands occurring along this symmetry direction.

Bibliography

- [1] S. Z. Butler, S. M. Hollen, L. Cao, Y. Cui, J. A. Gupta, H. R. Gutiérrez, T. F. Heinz, S. S. Hong, J. Huang, A. F. Ismach, E. J. Halperin, M. Kuno, V. V. Plashnitsa, R. D. Robinson, R. S. Ruoff, S. Salahuddin, J. Shan, L. Shi, M. G. Spencer, M. Terrones, W. Windl, and J. E. Goldberger, *ACS Nano* **7**, 2898 (2013).
- [2] J. Kim, J. Kim, and S. -H. Jhi, *Phys. Rev. B* **82**, 201312 (2010).
- [3] B. Singh, H. Lin, R. Prasad, and A. Bansil *Phys. Rev. B* **88**, 195147 (2013).
- [4] T. V. Menshchikova, S. V. Ereameev, Y. M. Koroteev, V. M. Kuznetsov, and E. V. Chulkov, *JETP Letters* **93**, 15 (2011).
- [5] A. Qurashi, *Metal Chalcogenide Nanostructures for Renewable Energy Applications* Wiley ISBN: **978-1-118-23791-5** (2015).
- [6] H. Wei, S. Chen, X. Ren, B. Qian, Y. Su, Z. Yang, and Y. Zhang, *Cryst Eng Comm.* **14**, 7408 (2012).
- [7] D. Reso, M. Silinskas, M. Lisker, A. Schubert, and E.P. Burte, *Appl. Phys. Lett.* **98**, 151901 (2011).
- [8] P. Dandamudi, M. N. Kozicki, H. J. Barnaby, Y. Gonzalez-Velo, M. Mitkova, K. E. Holbert, and M. Ailavajhala, W. Yu, *Nuclear Sci IEEE Trans.* **60**, 4257 (2013).
- [9] R. Eymard, and A. Otto, *Phys. Rev. B* **16**, 1616 (1977).
- [10] P. D. Antunez, J. J. Buckley, and R. L. Brutchey, *Nanoscale* **3**, 2399 (2011).
- [11] N. L. Nagard, C. Levy-Clement, A. Katty, R. M. A. Lieth, *Materials Research Bulletin* **25**, 495 (1990).

- [12] L. Makinistian, and E. A. Albanesi, *J. Phys.: Condens. Matter* **19**, 186211 (2007).
- [13] L. -M. Yu, A. Degiovanni, P. A. Thiry, J. Ghijsen, and R. Caudano, *Phys. Rev. B* **47**, 16222 (1993).
- [14] A. M. Elkorashy, *Phys. Status Solidi b* **135**, 707 (1986).
- [15] G. Valiukonis, F. M. Gashimzade, D. A. Guseinova, G. Krivaite, A. M. Kulibekov, G. S. Orudzhev, and A. Sileika, *Phys. Status Solidi b* **117**, 81 (1983).
- [16] A. M. Elkorashy, *Phys. Status Solidi b* **149**, 747 (1988).
- [17] A. M. Elkorashy, *Phys. Status Solidi b* **152**, 249 (1989).
- [18] M. Taniguchi, R. L. Johnson, J. Ghijsen, and M. Cardona, *Phys. Rev. B* **42**, 3634 (1990).
- [19] H. C. Hsueh, and J. Crain, *Phys. Status Solidi b* **211**, 365 (1999).
- [20] R. B. Shalvoy, G. B. Fisher, and P. J. Stiles, *Phys. Rev. B* **15**, 2021 (1977).
- [21] P. C. Kemeny, J. Azoulay, M. Cardona, and L. Ley, *Il Nuovo Cimento* **39**, 709 (1977).
- [22] A. Kosakov, H. Neumann, and G. Leonhardt, *J. Electron Spec. and Related Phenomena* **181**, 12 (1977).
- [23] T. Grandke, L. Ley, *Phys. Rev. B* **16**, 832 (1977).
- [24] S. K. Mahatha, K. D. Patel, and Krishnakumar S. R. Menon, *J. Phys.:Condens. Matter* **24**, 475504 (2012).
- [25] R. Kundu, P. Mishra, B. R. Sekhar, M. Maniraj, and S. R. Barman, *Physica B: Condensed Matter* **407**, 827 (2012).
- [26] G. K. Solanki, M. P. Deshpande, and M. K. Agarwal, *Indian Journal of Engineering and Materials Sciences* **14**, 373 (2007).
- [27] O. K. Anderson, *Phys. Rev. B* **12**, 3060 (1975).
- [28] A. Okazaki, *Journal of the Physical society of Japan* **13**, 10 (1958).
- [29] U. V. Waghmare, N. A. Spaldin, H. C. Kandpal, and R. Seshadri, *Phys. Rev. B* **67**, 125111 (2003).

- [30] R. B. Shalvoy, G. B. Fisher, and P. J. Stiles, Phys. Rev. B. **15**, 1680 (1977).
- [31] R. D. Bringans, M. A. Olmstead, R. I. G. Uhrberg, and R. Z. Bachrach, Phys. Rev. B **36**, 9569 (1987).
- [32] M. Nagelstraßer, H. Dröge, H.-P. Steinrück, F. Fischer, T. Litz, A. Waag, and G. Landwehr, Phys. Rev. B **58**, 10394 (1998).
- [33] V. Hinkel, H. Haak, C. Mariani, L. Sorba, K. Horn, and N. E. Christensen, Phys. Rev. B **40**, 5549 (1989).
- [34] J. Olde, G. Mante, H. -P. Barnscheidt, L. Kipp, J. -C. Kuhr, R. Manzke, and M. Skibowski, Phys. Rev. B **41**, 9958 (1990).
- [35] K. O. Magnusson, and S. A. Flodström, Phys. Rev. B **56**, 228 (1997).

Chapter 7

Summary

In this thesis, we have investigated the electronic structure of several layered superconductors and semiconductors using photoemission spectroscopy in conjunction with LDA based band structure calculations.

Chapter-1 presents a brief introduction of the layered materials with special focus on the layered superconductors and semiconductors. The general physical and electronic properties of iron and BiS superconductors and GeSe semiconductor has been discussed in brief.

Chapter-2 deals with the discussion on experimental methodologies used for the thesis work. The working principle and instrumentation of ARPES, UPS, XPS and IPES have been explored. The basic concepts and theoretical background of TBLTMTO based band structure calculations have been presented.

Chapter-3 discusses the electronic structure of Fe(Se,Te) systems, a member of (11) family of Fe superconductor. Using UPS and IPES we have studied the occupied and unoccupied states respectively of $\text{FeSe}_{1-x}\text{Te}_x$ ($x = 1, 0.5, 0$). A pseudogap opening with Se substitution observed in both valence band and unoccupied states has been correlated to the chalcogen height dependent structural changes in the $\text{Fe}(\text{Se,Te})_4$ tetrahedra. In an analogy with the doping dependent case, a pseudogap opening at low temperature is caused due to the shift in the electron occupancy from the xz/yz and $x^2 - y^2$ orbitals to the $3z^2 - r^2$ orbitals. The spectral weight depletion near Fermi level in PES indicates a temperature induced crossover from a metallic state to an Orbital Selective Mott (OSM) Phase. The depletion in spectral weight near E_F at low temperature in IPES occurs due to the enhancement of the electron occupancy of $3z^2 - r^2$ orbitals in PES. The coulomb correlation energy U , estimated from the combined PES and IPES spectra signifies the enhancement in electron correlations in $\text{FeSe}_{1-x}\text{Te}_x$. The pseudogap formation confirms the importance of correlations in the 11 family of Fe superconductors.

Chapter-4 presents the electronic structure of NdFeAsO(F) system, a member of (1111) family of Fe superconductor. The valence band photoemission on NdFeAsO_{1-x}F_x (x = 0, 0.2) in support with the LDA band structure calculations reveal a doping and temperature dependent pseudogap. The reduction in pnictogen height, induced by the changes in Fe-As tetrahedra results in the depletion of spectral weight near Fermi level. The observed temperature dependent pseudogap in the parent compound, NdFeAsO is attributed to the spin density wave. On the other hand, the pseudogap formation in the doped compound has been correlated with the enhanced Fe-3d interorbital hybridisation induced by the reduced pnictogen height at low temperature. Further, the temperature induced pseudogap in the F doped NdFeAsO generates an Orbital Selective Mott Transition, where the metallic Fe-3d x^2-y^2 and yz/zx orbitals turn insulating at low temperature, similar to that observed in Fe(Se,Te) systems. The different origin of pseudogap formation in the parent (linked to SDW) and doped compound (linked to pnictogen height), signifies the intricate interplay of magnetism and multiorbital correlations in the (1111) family of Fe superconductors.

Chapter-5 covers the electronic structure of a recently discovered BiS based superconductor. The valence band photoemission on RE (La, Ce) doped SrFBiS₂ superconductors have been investigated using photoemission spectroscopy. The changes in the electronic structure of SrFBiS₂ with doping of rare earth elements have been explained in terms of the band structure calculations. The doped systems exhibit a shifting of the Fermi level towards the conduction band which results in the shifting of the photoemission spectral features towards higher binding energies in comparison to the parent compound. An enhanced spectral weight near E_F with a simultaneous depletion of states at higher binding energy, with doping was observed in the photoemission spectra. This has been correlated to the reduced distortion of S1-B-S1 plane and change of Fermi surface topology for the case of doped compounds.

Chapter-6 deals with the electronic structure of a layered semiconducting chalcogenide GeSe, investigated using XPS and ARPES which is further supported by our band structure calculations. XPS probes the core level electronic structure confirming the chemical constituent of GeSe. The dispersive bands along the three symmetry directions Γ -Z, Γ -Y and Γ -T match qualitatively with the theoretical bands. The valence band maximum was reported around -0.5 eV binding energy which occurs midway along the Γ -Z direction. This supports the indirect band gap of GeSe. The variation of dispersion along different symmetry directions occurs due to the difference in hybridisation of Se and Ge 4p orbitals. The highly dispersive band along Γ -

T direction has been correlated to the predominance of Se $4p_z$ orbitals. The detailed electronic structure analysis confirms the significance of the hybridised cation-anion 4p orbitals in the band structure of IV-VI semiconductors.